TOWARDS FULLY AUTOMATED, MOTION-ROBUST DIFFUSION-WEIGHTED MRI OF THE ABDOMEN

By

Ruiqi Geng

A dissertation submitted in partial fulfillment of

the requirements for the degree of

Doctor of Philosophy

(Electrical and Computer Engineering)

at the

UNIVERSITY OF WISCONSIN-MADISON

2023

Date of final oral examination: June 21, 2023

The dissertation is approved by the following members of the Final Oral Committee:

Diego Hernando, Associate Professor, Radiology, Medical Physics, Electrical & Computer Engineering, Biomedical Engineering

Scott B. Reeder, Professor, Radiology, Medical Physics, Biomedical Engineering, Medicine, and Emergency Medicine

Ali Pirasteh, Assistant Professor, Radiology and Medical Physics

Oliver Wieben, Professor, Medical Physics and Radiology

Kevin M. Johnson, Assistant Professor, Medical Physics and Radiology

Abstract

Diffusion-weighted (DW) MRI of the abdomen is utilized clinically in the detection, diagnosis, and treatment monitoring of cancer and non-cancer disease. Despite its enormous potential, poor reproducibility and inefficient clinical workflow of DW imaging remain bottlenecks for rapid, high-value DW-MRI of the abdomen. A central challenge is physiological motion, including cardiac and respiratory motions. As the heart and vessels pulsate, they exert compressive tissue motion in the liver and the pancreas. The compressive tissue motion results in phase variations, leading to signal loss in diffusion-weighted images and bias in quantitative measurements. Furthermore, the slower respiratory motion results in mis-registration among repetitions taken in different phases of the respiratory cycle during free-breathing acquisitions.

Inefficient clinical workflow for DW-MRI acquisition remains another technical challenge. Currently, all abdominal DW-MRI scans are prescribed manually by technologists and routinely acquired with respiratory gating. That workflow requires training of technologists and takes a significant portion of the scan time. The resulting prescription can show high inter-operator variation and occasionally insufficient coverage. A fully automated MRI prescription that would cover the whole liver is needed. Besides, although respiratory-triggering DW-MRI acquisition methods can reduce respiration-induced artifacts, these methods lead to poor SNR and unpredictable scan times due to their highly variable effective repetition time, reducing the efficiency of clinical imaging workflows. In contrast, free-breathing methods without triggering enable abdominal DW-MRI with high SNR efficiency and predictable scan times, albeit at the risk of respiration-induced mis-registration. Thus, there is an unmet need for a free-breathing DW-MRI acquisition combined with motion-corrected averaging, to enable high-SNR DW-MRI with predictable scan times and free from motion artifacts.

This thesis describes technical innovations to address the aforementioned needs in order to enable fully automated, motion-robust diffusion-weighted MRI of the abdomen. An automated AI-based method for image prescription of liver MRI was developed and evaluated to standardize liver MRI prescription and improve the clinical workflow. Additionally, the cardiovascular motion artifacts was characterized and corrected in a motion phantom and healthy volunteers for pancreas DW-MRI. Finally, motion-robust, free-breathing DW-MRI in the liver was developed using optimized motion-compensated diffusion gradient waveforms and a motion-corrected averaging algorithm.

Acknowledgements

I would like to begin by thanking my advisor Dr. Diego Hernando. I still remember when I was giving my first oral presentation at ISMRM, he went through the materials with me more than five times and my phrasing word by word. He would go through meetings with the techs with me for add-on studies. His mentorship and encouragement allowed me to grow both technically and professionally as a researcher. My co-advisor Dr. Scott Reeder has always been considerate and provides invaluable insights into the clinical significance of our work. His leadership in the field inspires me. It has been a privilege to be a part of Drs. Diego Hernando and Scott Reeder's research teams. I have learned both from their direct mentorship and from their excellent examples. I would also like to thank the remaining members of my PhD committee, Dr. Oliver Wieben, Dr. Ali Pirasteh, and Dr. Kevin Johnson. Not only have they supported me in their roles as committee members, but each has been an inspiring teacher during my graduate coursework.

I have been surrounded by an excellent group of researchers in the Quantitative Imaging Methods Lab (QIML) and Liver Imaging Research Program (LIRP). I would like to give my never ending thanks to Dr. Yuxin (Annie) Zhang; very few of my ideas in diffusion-weighted imaging made it to the page without discussing with her first. I would like to give a heartfelt thank you to Dr. Jitka Starekova for the times I ended up going to her with clinical questions during my time in the program. Sincere thank you to Drs. Daiki Tamada, Nikolaos Panagiotopoulos, Thekla Oechtering, Edward Lawrence, Greg Simchick, Raphael Tadeu Do Vale Souza, Marcin Ignaciuk, and Matthias Mühler. Special thanks to my fellow lab-mates, Collin Buelo, James Rice, Tim Allen, Yavuz Muslu, Sheena Chu, Srijyotsna (Lucky) Volety, Aidan Tollefson, Jiayi Tang, Garrett Fullerton, Dr. Ruiyang Zhao, Huiwen Luo, Ruvini

Navaratna, Zihan Wang, Dr. Xiaoke Wang, Dr. Ante Zhu, Dr. Timothy J. Colgan, Louis Hinshaw Jr., Zachary N. Schwartz, and big thanks to Dr. David Harris and Ashley Hinrichs. I could not have asked for a better group of people to spend my PhD career with.

I am grateful to my fellow researcher Mahalakshmi Sundaresan who graduated from the ECE department in 2020 for working together on computer vision techniques for medical imaging. It has been a pleasure to work with the brilliant scientists and excellent staff in the UW Radiology and Medical Physics departments. I would like to express my gratitude to Carol Aspinwall, Sara John, Kelli Hellenbrand, Juliette M. Schefelker, Daryn Belden, Colin Keunyong Kim, Drs. John Garrett, Alejandro Roldán-Alzate, David Rutkowski, Ty Cashen, Jim Holmes, Karl Vigen, Frank Korosec, and Tomy Varghese. I would like to thank our GE collaborators Drs. Patricia Lan, Arnaud Guidon, Dan Rettman, and Lloyd Estkowski for the great conversations at weekly meetings. And I would like to express my gratitude towards my internship managers Drs. Laura Bell and Cheng Chen for their mentorship at Genentech and Google.

Finally, I would like to thank my family and friends. The hard work of my grandmother, Zhifeng Li, as a nurse and mid-wife in rural China and her abrupt passing from lung cancer inspired me to pursue a career to improve human health. My amazing parents, Xiumei Wang and Xijun Geng, have led by example as the dedicated engineers and always supported my decisions and encouraged me to pursue wildest dreams. I am forever grateful for their unwavering love and care. My close friends, Kai Huang, Xuening Wang, Tawa Alabi, Jianxiong Yu, Yanshan Guo and among others, have shared my life events. I also want to thank my boyfriend, Josh Yeend. Our dating started after multiple hour-long walks in the freezing Wisconsin winter in the midst of the pandemic. He has ever since been a constant source of strength and encouragement while I was away from my family in China and juggling PhD research and two internships.

Table of Contents

List of Figures

List of Tables

Chapter 1 Introduction

1.1 Overview and Specific Aims

1.1.1 Purpose

The overarching purpose of this work is to develop fully automated and motion-robust diffusion-weighted (DW)-MRI methods of the abdomen, to enable high throughput, high image quality, and improved quantification of diffusion properties in the abdomen.

1.1.2 Motivation

DW-MRI has a unique capacity to probe tissue microstructure without the need for ionizing radiation or intravenous contrast agents(1). DW-MRI of the abdomen is utilized in the detection(2–9), diagnosis(10), and treatment monitoring(11–14) of cancer and non-cancer disease in various organs(1). Despite its enormous potential, the poor reproducibility and inefficient clinical workflow of diffusion weighted MRI remain a bottleneck for rapid, high-value DW-MRI of the abdomen(4, 10, 15, 16).

A central challenge for diffusion-weighted imaging (DWI) of the abdomen is physiological motion, including cardiac and respiratory motions. As the heart and vessels pulsate, they exert compressive tissue motion in the liver and the pancreas. The compressive tissues motion results in phase variations, which leads to signal loss in the diffusion weighted images and bias in quantitative measurements(17–21). Furthermore, the slower respiratory motion results in mis-registration among repetitions taken in different phases of the respiratory cycle during free-breathing (FB) acquisitions(22).

The inefficient clinical workflow for DW-MRI acquisition remains another technical challenge. Currently, all abdominal DW-MRI scans are prescribed manually by technologists(23) and routinely acquired with respiratory gating(24). That workflow requires training of

technologists and takes a significant portion of the scan time(23). The resulting prescription can show high inter-operator variation and occasionally insufficient coverage(23). A fully automated MRI prescription that would cover the whole liver is needed. Besides, although respiratory-triggering (RT) DW-MRI acquisition methods can reduce respiration-induced artifacts, RT methods lead to poor SNR(25) and unpredictable scan times(24) due to their highly variable effective repetition time (TR), reducing the efficiency of clinical imaging workflows. In contrast, FB methods without triggering enable abdominal DW-MRI with high SNR efficiency and predictable scan times(24), albeit at the risk of respiration-induced mis-registration. Thus, there is an unmet need for a FB DW-MRI acquisition combined with motion-corrected averaging, in order to enable high-SNR DW-MRI with predictable scan times and free from motion artifacts.

Our research group have recently achieved several advances to address these major challenges. Optimized motion-compensated diffusion gradient waveforms with minimized TEs have been recently proposed(26–28) to address signal dropouts in the presence of cardiovascular-related motion. Although motion-robust DWI methods have been demonstrated in various applications of DWI, including in liver(27, 28) and cardiac(26) imaging, their performance in the pancreas remains unknown. A motion-corrected averaging approach based on non-local means (NLM) has been demonstrated potential in chemical shift encoded MRI in the abdomen(29). Development and optimization of the NLM approach to be applied in abdominal DWI is needed. Combination of these techniques further with motion-corrected averaging is promising to enable motion-robust, free-breathing DW-MRI acquisitions.

1.1.3 Specific Aims

I addressed these challenges and opportunities by pursuing the following aims:

Aim 1: Automated image prescription for liver MRI using deep learning;

Aim 2: Characterization and correction of cardiovascular motion artifacts in pancreas DWI;

Aim 3: Development of optimized methods for motion-robust, free-breathing DWI in the liver using optimized motion-compensated diffusion gradient waveforms and a motion-corrected averaging algorithm.

1.2 Abdominal DW-MRI

1.2.1 Clinical value

Diffusion MRI is routinely acquired in abdominal MRI exams for evaluation of neoplastic or infectious/inflammatory disease processes(1). Diffusion MRI is predominantly utilized for detection, diagnosis, and treatment monitoring of abnormalities, including liver and pancreatic lesions(2, 3, 5–9).

Detection of the presence and the number of liver lesions often changes the disease stage and hence how the patient is treated. Therefore, successful detection of small liver lesions can make a difference in patient management. Although Gadoxetate-(Gd-)enhanced liver MRI is highly sensitive to liver metastases from colorectal cancer and neuroendocrine tumors(5, 6), lesions that are sub-centimeter and/or adjacent to vessels remain difficult to detect. Such lesions appear conspicuous in DW images as signals from background liver parenchyma and major vessels are suppressed. An example of DWI improving the detection of small liver lesions compared to Gd-enhanced liver MRI is shown in **Figure 1**. Therefore, DWI serves as an invaluable tool for the detection of metastatic liver lesions. DWI has also been shown to have a similar accuracy as contrast-enhanced MRI for the diagnosis of pancreatic cancer and pancreatic neuroendocrine tumors(9).

Diagnosis: Malignant lesions generally have a lower ADC than benign lesions, and several thresholds have been proposed(10). Further, ADC measurements may enable differentiation of malignant pancreatic lesions from healthy tissue(30), mass-forming pancreatitis(15, 31), and other benign lesions(32, 33) and potentially determine the tumor grade(34, 35). However, there is substantial overlap in ADC values between benign and malignant pancreatic and solid liver lesions(4, 10, 15, 16). This overlap, which likely arises from technical challenges including motion-induced artifacts as well as biological variability within tumors, currently limits the practical utility of ADC for lesion characterization. The pancreas, due to its location within the retroperitoneum, is substantially affected by physiological motion including respiratory(8, 15), peristaltic(36, 37), and cardiovascular-related motion(38). In particular, cardiovascular-related motion, due to both direct cardiac motion and pulsation of large blood vessels, is not as manageable(8, 15, 36, 37) as the other two forms of motion and its effect is not understood in the context of DWI of the pancreas.

Treatment monitoring: Quantitative diffusion measurements reflect multiple tissue properties such as cellularity, cell size, necrosis, and perfusion. These tissue properties often change before macroscopic changes such as alterations in lesion size. Therefore, quantitative diffusion MRI has also sparked interest for the early assessment of treatment response in various cancer imaging applications(11). DWI improves the characterization of liver metastases in the context of treatment monitoring(5, 39). In the pancreas, measured ADC values in the pancreas has been shown to correlate well with histopathological markers, such as the proportion of collagenous fibers(40). DWI has also shown potential to enable early prediction of treatment response(12–14) as change of tumor ADC values in unresectable pancreatic cancer during chemotherapy facilitates survival prediction and treatment plan adjustments.

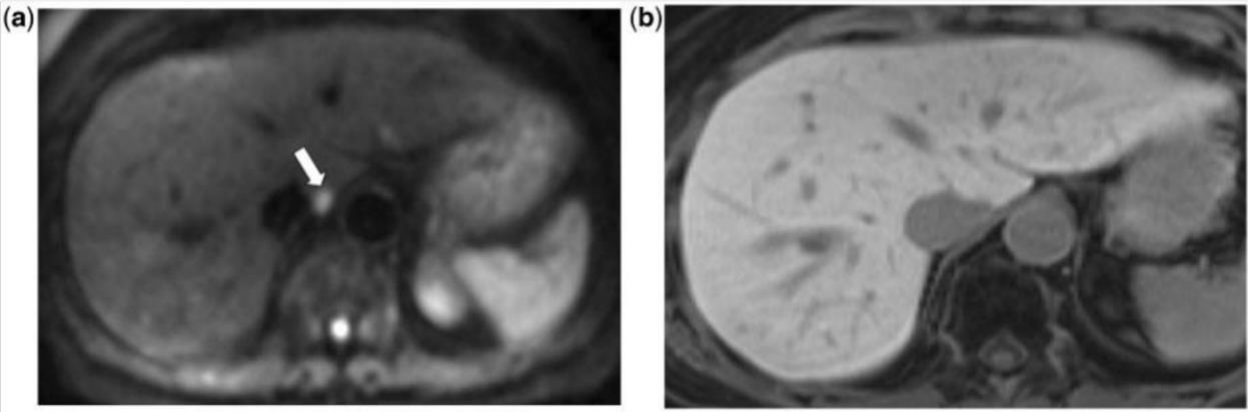

Figure 1. DW-MRI improves the detection of small metastases that may mimic small blood vessels on the hepatocellular phase of Gd-EOB-DTPA-enhanced imaging*(41). Liver metastasis mimicking intrahepatic vasculature on Gd-EOB-DTPA-enhanced imaging. A 48 year-old man with colorectal cancer. (a) b = 750 s mm^{-2} image shows high-signal metastasis in the caudate lobe of the liver adjacent to the inferior vena cava (arrow). (b) The lesion is poorly seen and cannot be distinguished from the intrahepatic vasculature, which also appears hypointense relative to the liver in the hepatocellular phase of contrast enhancement. Figure from (41).*

1.2.2 Technical challenges and recent developments

DW-MRI in the abdomen faces multiple technical challenges that hinder its widespread usage in clinical research and the clinics. In particular, physiological motion, including cardiovascular pulsation and respiratory motion, results in distinct artifacts in DW-MRI. This thesis focuses on addressing motion-related challenges, as motion is the central challenge in DW-MRI in the abdomen and success in this front may help ameliorate other challenges.

1.2.2.1 Signal dropouts due to cardiovascular-related motion

Compressive motion arises both from direct contact with the pounding heart (as in the left lobe of the liver), as well as from pulsation effects near large blood vessels (as in the pancreas head and body). Importantly, this motion leads to unpredictable signal loss in DW-MRI in the liver(17–20). Signal loss confounds image interpretation, obscures underlying pathology(42), and results in biased (overestimated) and imprecise quantitative diffusion measures, such as ADC(17, 21). Our

research group recently proposed motion-compensated waveforms that were designed using the Optimized Diffusion-weighting Gradient waveform Design (ODGD) method(27) to correct for cardiovascular motion artifacts in the liver. Furthermore, motion-robust M1-optimized diffusion gradient waveforms (MODI) can address cardiac-induced artifacts while reducing blood signal(28). Importantly, the effect of cardiovascular-related motion, due to pulsation of large blood vessels, is not understood in the context of DWI of the pancreas. As part of this thesis, I set out to characterize and correct cardiovascular motion artifacts in pancreas DWI (Aim 2).

1.2.2.2 Mis-registration among repetitions due to respiration

Respiratory motion is routinely managed using breath-held (BH) or respiratory-triggered (RT) methods(4), both of which suffer from poor SNR(24, 25). RT methods, due to their highly variable effective repetition time (TR), lead to unpredictable scan times(24) reducing the efficiency of clinical imaging workflows. Free-breathing (FB) methods without triggering, on the other hand, enable abdominal DW-MRI with high SNR efficiency and predictable scan times(24). However, FB DW-MRI of the abdomen leads to substantial mis-registration across repetitions, diffusion directions, and b-values. If uncorrected, this mis-registration leads to blurring in DW images and bias in ADC maps(22). Thus, there is an unmet need for a FB DW-MRI acquisition combined with motion-corrected averaging(29, 43), in order to enable high-SNR DW-MRI with predictable scan times and free from motion artifacts. Our research group has demonstrated the potential of a motion-corrected averaging approach based on non-local means (NLM) in chemical shift encoded MRI in the abdomen(29). As part of this thesis, I further developed and optimized the NLM approach for FB abdominal DWI (Aim 3).

1.2.2.3 Image distortions

DW-MRI of the abdomen is routinely acquired using single-shot echo-planar imaging (ss-EPI)(4). As the entire image is acquired following a single excitation, ss-EPI suffers from limited spatial resolution and image distortions in complex magnetic susceptibility environments, such as the abdomen(4, 20, 44, 45). Thus, small focal lesions cannot be reliably visualized, which severely limits the clinical utility of DW-MRI(4, 46). Furthermore, abdominal lesions are often heterogeneous, comprised of a necrotic center with higher ADC and viable periphery with lower ADC(4, 47, 48). To reliably visualize and quantify these lesions, high-resolution, low-distortion DW-MRI needs to be developed and validated. Multi-shot EPI (ms-EPI) acquisitions enable low-distortion, high-resolution DW-MRI(49–51) of the brain and have demonstrated reproducible performance in static diffusion phantoms as well as in the prostate(52). However, ms-EPI methods are currently unreliable in the abdomen due to severe challenges with inter-shot phase inconsistency. Our research group recently showed that a synergistic combination is feasible between motion-robust DW gradient waveforms (which reduce the motion-induced phase variations in the acquired data) and low-distortion DW-MRI(53). I, along with Yuxin Zhang et al, have published this work, which is not included in this thesis.

1.2.2.4 Modeling limitations

The simplest diffusion signal model assumes a mono-exponential signal decay with increasing b-values, parametrized by the Apparent Diffusion Coefficient (ADC). ADC measurements provide an overall measure of diffusion signal decay rate, based on unrestricted Gaussian diffusion (e.g., in a water phantom). However, the ADC model does not account for various complexities in tissue microstructure and intra-voxel heterogeneity. Advanced signal

models that take non-mono-exponential signal decays into account, such as intravoxel incoherent motion (IVIM), have been proposed(54, 55). In many abdominal organs, a perfusion compartment gives rise to a rapidly decaying signal component at low b-values (e.g. in blood water molecules moving in random directions with velocity V_b). IVIM parameterizes the rapidly decaying signal as an additive exponential decay with a rapid decay rate (D^*) and signal fraction (F) in a bi-exponential signal model. The quantitative parameters derived from IVIM may help evaluate various liver diseases such as fibrosis, hepatitis, and hepatocellular carcinoma(56–58). However, the predictive performance (e.g., distinguishing benign vs malignant lesions) of the blood microcirculation or perfusion parameters suffers from high measurement variability and poor precision, with poor test-retest repeatability and reproducibility across field strengths when using conventional IVIM methods(59, 60).

1.2.2.5 Fat suppression artifacts

Fat suppression is essential for DW-MRI in the abdomen, due to the presence of substantial subcutaneous, visceral, and intra-organ fat depots(61–63). With a long T2 relaxation time and an extremely low diffusion coefficient, fat appears bright in diffusion MRI. Fat signals have a large chemical shift, leading to large spatial shifts along the phase encoding dimension in EPI acquisitions, resulting in the so-called chemical shift artifacts. Thus, unsuppressed fat signals from visceral or subcutaneous depots may appear artifactually shifted and overlap with the organs of interest. Suppression of fat signals in DW-MRI is typically performed based on the chemical shift effect, i.e., selective excitation of signals that resonate at the expected water frequency while avoiding excitation of signals that resonate at the expected fat frequency. However, in the presence of B0 inhomogeneities, particularly in complex susceptibility environments such as in the abdomen, chemical shift-based fat suppression may fail, leading to

bright fat signals that overlap with the organs of interest(64). The chemical shift-based fat suppression failures are common in clinical practice and often lead to non-diagnostic image quality. Alternative fat signal suppression methods, e.g., based on inversion recovery fat signal nulling, often improve the robustness of fat suppression but can result in lower SNR(65, 66).

1.2.2.6 Other challenges

Diffusion MRI typically has relatively low SNR. The sensitivity of diffusion MRI to tissue microstructure emerges at relatively high diffusion weighting, with substantial signal decay. The gradient waveforms and long EPI echo trains in the pulse sequence leads to long echo times, resulting in low SNR in tissues with short T2 (e.g., the liver). This challenge is particularly severe in patients with iron overload, which results in substantially shorter T2 and T2*. In addition, gradient nonlinearities can lead to non-uniform diffusion weighting throughout the image, particularly away from isocenter, and introduce spatially-dependent quantification bias(67). Since DW-MRI is often obtained with thick slices to preserve SNR and with limited in-plane spatial resolution to minimize image distortions in the context of long-readout EPI acquisitions, partial volume effects can introduce bias in quantitative diffusion measurements, particularly when assessing small anatomical structures or focal lesions. Besides the technical challenges, biological variability may confound the ability of quantitative diffusion measurements to evaluate disease(61). For example, different tumors may have different correlations between ADC and cellularity, possibly because various other microstructural features, such as extracellular matrix, nucleic areas, ratio of stroma to parenchyma, or microvessel density, can affect ADC(68).

1.2.3 Innovation

1.2.3.1 Technical development

Developing novel motion-corrected averaging algorithms based on a non-local means approach (NLM) (Aim 3) would allow high SNR, motion robust FB acquisitions. Additionally, FB acquisitions with a fixed TR enable the incorporation of advanced hybrid fat suppression methods that rely on both spectral selection and T1(52), leading to improved robustness in fat suppression, while the clinical standard respiratory-triggered acquisitions are not compatible with those methods due to the variable effective TR (43, 69).

1.2.3.2 Translational validation

Previous works in pancreas DW-MRI have not evaluated the effect of cardiovascular-related motion. *My work on the characterization and correction of cardiovascular motion artifacts in pancreas DWI (Aim 2)* includes validation in a 3D-printed anatomically accurate pancreas motion phantom(70), establishing the correlation between tissue compressive motion and DWI signal dropouts due to phase variations through controlled experiments(71).

1.3 Automated image prescription of liver MRI

1.3.1 Clinical need for fully automated prescription of liver MRI

In abdominal MRI, patient experience and cost correlate closely with exam time(72). Recent technical advances have the potential to enable MRI of the abdomen with enhanced efficiency. For example, abbreviated MRI protocols have demonstrated excellent performance for the detection of abdominal lesions as well as diffuse liver disease(72, 73). Further, motion-robust free-breathing quantitative MRI methods are being developed to enable quantification of

various imaging biomarkers without the need for breath-holds(74–76). These developments may enable fully automated, single button-push focused exams of the liver with multiple advantages in terms of patient throughput, imaging volume, staff training and time, accessibility, and clinical workflow. An example workflow of such single button-push exams proposed by our group is shown in **Figure 2**. However, single button-push exams require fully automated prescription of the liver. For these reasons, the current manual image prescription remains a bottleneck for rapid, high-value MRI of the abdomen. Automated prescription may reduce non-value-added preparatory time and improve the reproducibility of image prescription within and across sites(77, 78).

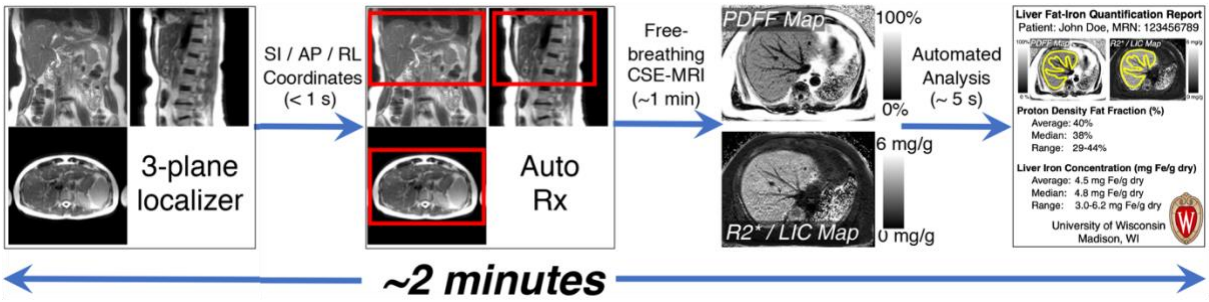

Figure 2. Automated liver image prescription will help enable rapid fat/iron quantification protocol proposed by our group. *This graphic shows an optimized workflow proposed by our research group, from free-breathing localizer acquisitions to automated liver prescription, to free-breathing fat and iron quantification sequences, and finally automated reporting of fat/iron content.*

1.3.2 Technical challenges and recent developments

Previous efforts towards automated scan prescription in the liver have relied on traditional image processing tools, such as active shape models, to detect the upper and lower edges of the liver(79, 80). In Goto et al, the upper edge of the liver was detected automatically using an active shape model, and the lower edge was detected using a probabilistic estimate based on automatically-derived statistics of the signal within the liver(79). Although promising,

this previous method requires a specialized volumetric, breath-held localizer scan, is limited to prescription of axial series, has been tested in limited numbers of healthy volunteers (n = 24) and simulated deformed livers (n = 7).

Artificial intelligence (AI) methods have enabled automated image prescription in the brain, spine, heart, and kidney, with the potential to improve workflow, efficiency, and prescription accuracy and consistency(77, 81, 82, 23, 83–86). AI has been used to address the persistent challenge of accurately localizing intervertebral discs (IVD) during MR examinations of the lumbar spine in a consistent and time-efficient manner(23). Furthermore, a cardiac MRI prescription method has recently been implemented, which substantially reduces examination time by automating real-time localization(82, 84). However, automated prescription of the liver remains an important unmet need.

1.3.3 Innovation

1.3.3.1 Technical development

Recent developments have demonstrated that artificial intelligence (AI) methods can enable automated image prescription in other applications, including spine, heart, and brain(12–14). However, AI-based image prescription for liver MRI remains an unmet need. My work to develop *a fully automated AI-based image prescription of liver MRI series (Aim 1) based on a localizer acquisition* has the potential to standardize liver MRI prescription and improve the clinical workflow.

1.3.3.2 Translational validation

In previous works, the development of automated MR prescription methods is often not validated systematically with a large patient cohort or a wide variety of pathologies(23, 82, 85,

86). The *fully automated liver MRI prescription method (Aim 1)* has been evaluated over a large population, different field strengths, localizer sequences, and a variety of pathologies(87).

1.4 Summary

This work developed and validated novel image prescription, acquisition, and post-processing methods for MRI of the abdomen. By enabling automated image prescription of the liver, improved automated workflow (Aim 1), and improved diffusion imaging of the pancreas and liver (Aims 2-3), these methods advance the reliability, value, and quantitative performance of abdominal MRI.

1.5 Thesis Outline

Following the aims of this work, the remainder of this dissertation is organized as follows:

- Chapter 2: To standardize liver MRI prescription and improve clinical workflow, I developed and evaluated an automated AI-based method for image prescription of liver MRI.
- Chapter 3: Cardiovascular motion artifacts were characterized and corrected in a motion phantom and healthy volunteers for pancreas DWI.
- Chapter 4: Motion-robust, free-breathing DWI in the liver was developed using optimized motion-compensated diffusion gradient waveforms and a motion-corrected averaging algorithm.
- Chapter 5: A final summary of this work is given and the potential for future work is discussed.

1.6 Journal publications and conference presentations

- *Summary of work for Aim 1*: **Geng R**, Buelo CJ, Sundaresan M, et al.: Automated MR Image Prescription of the Liver Using Deep Learning: Development, Evaluation, and Prospective Implementation. *Journal of Magnetic Resonance Imaging* 2022; ePrint. Nominated for ISMRM Young Investigator Award finalist
- *Summary of work for Aim 2*: **Geng R**, Zhang Y, Starekova J, et al.: Characterization and correction of cardiovascular motion artifacts in diffusion-weighted imaging of the pancreas. *Magn Reson Med* 2021; 86:1956–1969.
- *Technical development for Aim 3*: **Geng R**, Zhang Y, Luo H, Hernando D: Toward high-SNR, motion-robust diffusion MRI of the liver using optimized gradient waveforms, non-gated free-breathing acquisitions, and motion-corrected averaging. *International Society for Magnetic Resonance in Medicine Annual Meeting (ISMRM) 2019; Montreal, Canada*. #0772. ISMRM Magna cum Laude award.
- *Patient validation for Aim 3*: **Geng R**, Zhang Y, Muhler MR, Starekova J, Hernando D: Liver Diffusion MRI using Optimized Gradient Waveforms, Free-Breathing Acquisitions, and Motion-Corrected Averaging: Validation in Patients. In *ISMRM 2020*; #2470.
- *Feasibility study for Aim 1*: **Geng R**, Sundaresan M, Starekova J, et al.: Automated Image Prescription for Liver MRI using Deep Learning. *ISMRM 2021; SABI 2021* ; #0532.
- *Systematic validation & prospective implementation for Aim 1*: **Geng R**, Buelo CJ, Sundaresan M, et al.: AI-based Automated Liver Image Prescription:

Evaluation across Patients and Pathologies and Prospective Implementation and Validation. *ISMRM 2022* ; #0598. ISMRM Magna cum Laude award.

- *Ongoing & future works for Aim 1*: **Geng R**, Buelo CJ, Sundaresan M, et al.: Automated MR Image Prescription of the Liver using Deep Learning: Feasibility Study, Evaluation, and Prospective Implementation. *ISMRM 2023* ; #0003. ISMRM Young Investigator Award competition presentation.
- *Work in progress presentation for Aim 2*: **Geng R**, Zhang Y, Starekova J, et al.: Characterization and correction of cardiovascular motion artifacts in diffusion-weighted imaging of the pancreas. *ISMRM 2020* ; #0459.
- *Ongoing & future work (repeatability & reproducibility study) for Aim 2*: Starekova J, Geng R, Pirasteh A, Wang Z, Zhang Y, Hernando D: Improved Repeatability of Abdominal Diffusion MRI using Motion-Compensated Methods. In *106th Sci Assem Annu Meet Radiol Soc N Am*; :2020.
- **Geng R**, Zhang Y, Rice J, et al.: Motion-robust, blood-suppressed, reduced-distortion diffusion MRI of the liver. *Magnetic Resonance in Medicine* 2023; 89:908–921.
- **Geng R**, Rice J, Zhang Y, et al.: Validation of motion-robust, blood-suppressed, reduced distortion liver diffusion techniques in a pulsatile motion phantom. *ISMRM 2022* ; #5038. ISMRM Magna cum Laude award.
- Simchick G, Geng R, Zhang Y, Hernando D: b value and first-order motion moment optimized data acquisition for repeatable quantitative intravoxel incoherent motion DWI. *Magnetic Resonance in Medicine* 2022; 87:2724–2740.

- **Geng R**, Grimbaldeston M, Coimbra AF, Bell L: PRM and Topological Imaging Features From HRCT Can Identify Prism Patients Who Progress to COPD. *American Thoracic Society (ATS) 2023* .
- Zhang Y, Geng R, Muehler MR, Guidon A, Hernando D: Motion-Robust, Reduced-Distortion Diffusion MRI of the Liver with Optimized Motion Compensated Waveforms and Multi-shot EPI. *ISMRM 2020* ; #2608.
- Starekova J, Estkowski L, Geng R, Zhang Y, Hernando D, Reeder SB: Optimizing T2-weighted MRI and DWI of the Esophagus. *ISMRM 2021* ; #0255.
- Rice J, Geng R, Hernando D, Roldán-Alzate A: Fabrication of an Anthropomorphic, In-Vitro Liver Flow Phantom for Use in Motion-Robust MRI Sequence Validation Experiments. *ISMRM 2022* ; #2727.
- Simchick G, Geng R, Zhang Y, Hernando D: b-M1-Optimized Waveforms for Improved Stability of Quantitative Intravoxel Incoherent Motion DWI. *ISMRM 2021* ; #0402.
- Zhang Y, Guidon A, Zhao X, Wu G, Li H, Geng R, Hernando D: Motion-Robust, High-SNR Diffusion MRI of the Liver using Optimized Gradient Waveforms and Deep Learning Reconstruction. *ISMRM 2021* ; #2123.

Chapter 2 Automated MR Image Prescription of the Liver using Deep Learning: Development, Evaluation, and Prospective Implementation

2.1 Introduction

In abdominal MRI, patient experience and cost correlate closely with exam time(72). Recent technical advances have the potential to enable MRI of the abdomen with enhanced efficiency. For example, abbreviated MRI protocols have demonstrated excellent performance for the detection of abdominal lesions as well as diffuse liver disease(72, 73). Further, motion-robust free-breathing quantitative MRI methods are being developed to enable quantification of various imaging biomarkers without the need for breathholds(74–76). These developments may enable fully automated, single button-push focused exams of the liver with multiple advantages in terms of patient throughput, imaging volume, staff training and time, accessibility, and clinical workflow. However, single button-push exams require fully automated prescription of the liver. For these reasons, the current manual image prescription remains a bottleneck for rapid, high-value MRI of the abdomen. Automated prescription may reduce non-value-added preparatory time and improve the reproducibility of image prescription within and across sites(77, 78).

Previous efforts towards automated scan prescription in the liver have relied on traditional image processing tools, such as active shape models, to detect the upper and lower edges of the liver(79, 80). In Goto et al, the upper edge of the liver was detected automatically using an active shape model, and the lower edge was detected using a probabilistic estimate based on automatically-derived statistics of the signal within the liver(79). Although promising, this previous method requires a specialized volumetric, breath-held localizer scan, is limited to prescription of axial series, has been tested in limited numbers of healthy volunteers (n = 24) and simulated deformed livers (n = 7).

Artificial intelligence (AI) methods have enabled automated image prescription in the brain, spine, heart, and kidney, with the potential to improve workflow, efficiency, and prescription accuracy and consistency(77, 81, 82, 23, 83–86). AI has been used to address the persistent challenge of accurately localizing intervertebral discs (IVD) during MR examinations of the lumbar spine in a consistent and time-efficient manner(23). Furthermore, a cardiac MRI prescription method has recently been implemented, which substantially reduces examination time by automating real-time localization(82, 84). However, automated prescription of the liver remains an important unmet need.

Therefore, the purpose of this study was to develop and implement an AI-based fully automated prescription method for liver MRI.

2.2 Materials and Methods

The overall workflow of the development and validation of the proposed automated prescription method is shown in **Figure 3**. In an IRB-approved study, the retrospective study was conducted with a waiver of informed consent and the prospective study was performed with informed consent with IRB approval.

2.2.1 Data and image processing

In this IRB-approved study, consecutive clinical abdominal MRI exams acquired between 9/23/2008 and 12/17/2019 at the University of Wisconsin Hospitals and Clinics were retrieved retrospectively, with a waiver of informed consent. The clinical MRI examinations were performed to confirm, exclude, or follow-up a wide variety of abdominal disorders. Patients with their BMI recorded within 30 days of one of their scans were included. Only one exam was included for any one patient in this study; the first exam of the patient was included in case of multiple eligible exams. The included exams were chosen randomly for manual annotation and

model training and testing. The scanner models used for the exams were Discovery MR750, Discovery MR750w, SIGNA Architect, SIGNA PET/MR and SIGNA Premier at 3T, and Optima MR450w, SIGNA, SIGNA Artist, SIGNA HDx and SIGNA HDxt at 1.5T. The scanners used in this study were all manufactured by GE Healthcare (Waukesha, WI). At the institution of this study, all abdominal MRI examinations start with a three-plane localizer series based on spin-echo or gradient-echo acquisitions. From each exam, the (first) localizer series was retrieved for annotation, curation, and analysis. This series includes multiple abdominal images (21-30 total) in the axial, coronal, and sagittal orientations to allow for prescription of subsequent MR sequences. For manual labeling and automated inference, each individual localizer image slice was read in MATLAB (2021a, Mathworks, Natick, MA). These acquired localizer images typically have spatially heterogeneous intensity due to the receive coil sensitivity profiles, where the subcutaneous fat and other areas near the receive coils are much brighter than the liver. To increase contrast around the liver, the intensity values of each image were normalized to 0 to 1 and values between 0 and 0.2 were mapped to values between 0 and 1 (with values larger than 0.2 saturated to 1). Each resulting normalized image was written as a .png file as the input format to the labeling software and neural network(88). A 80-20 split was used for AI model training and testing in accordance with common practice and to provide sufficient data for training while reserving a meaningful subset for testing. Out of the training set, the ratio between data used for parameter training and for validation of training performance was 9:1. Thus, the data partitioning across training/validation/testing was 72%-8%-20% of the total dataset.

2.2.2 Manual image annotation and intra- and inter-reader reproducibility

The Radiological Society of North America (RSNA) Medical Imaging Resource Community (MIRC) Clinical Trials Processor (CTP) was used to perform image de-

identification. Performance of manual image annotation of all three-plane localizer datasets was distributed among six board-certified abdominal radiologists (J.S., N.P., T.H.O., E.M.L., M.I., and S.B.R.) on the *Python* platform *LabelImg*(89, 90). Seven classes of labels were annotated using bounding boxes that span the liver, torso, and arms in specific image orientations (axial: liver, torso, and arms; coronal: liver and torso; sagittal: liver and torso; **Figure 3**) to enable liver image prescription in any orthogonal orientation. The torso and the arms are needed for coronal prescription to avoid phase wrap in the R/L dimension, while the torso is needed for sagittal prescription in the A/P and S/I dimensions. Arms and torso were annotated at the level of the liver in the superior/inferior dimension. In addition, 50 exams were randomly selected for intra- and inter-reader reproducibility studies. One radiologist (J.S.) labeled the same dataset twice after a month-long delay to assess intra-reader reproducibility. Two radiologists (J.S. and N.P.) labeled the same datasets to assess inter-reader reproducibility.

2.2.3 Model training

A deep convolutional neural network (CNN) based on a You Only Look Once (YOLOv3) architecture was trained for detection, localization, and classification of the aforementioned bounding boxes(91, 92). The network input includes a single image from the three-plane localizer acquisition. The YOLOv3 feature extractor, called Darknet-53 includes 106 layers, and contains skip connections and 3 prediction heads, each processing the image at a different down-sampling rate of 32, 16 and 8, respectively. Detection can thus be achieved at three different scales. The network detects each of the 7 classes of labeled objects described above with a confidence level (0-100%), and outputs the coordinates of the corresponding bounding boxes. Training and validation involved 72% and 8% of all patient datasets respectively (randomly chosen). Different training dataset sizes (5%-100% of all training

datasets) were used to evaluate the effect of training size on network performance using 5-fold cross validation. Reflection (horizontally and/or vertically) was used to augment the training set by four-fold.

Additionally, a shallower network based on a lightweight variant of YOLOv3, YOLOv3-tiny, was trained to enable real-time scanner implementation(93). The tiny network includes only 15 layers, and is able to predict bounding boxes 3x faster when implemented on a scanner with CPUs and no GPUs. This shallower network was trained using data augmentation methods: reflections, translation, scaling, and contrast modifications.

Termination of training for both kinds of networks relied on mean average precision (mAP), a common metric to evaluate performance of object localization in multi-class datasets(94).

2.2.4 3D image prescription

The trained network predicts each bounding box from each test image with a confidence level (0-100%) on its classification label. For each image, the bounding box with the highest confidence level was extracted for each of the liver- and torso-labeled boxes while the top 2 arms-labeled boxes with the highest confidence level were extracted for the arms. Based on the extracted bounding boxes for each image (from either the manual or automated annotations), image prescription for whole-liver acquisition in each orientation was calculated as the minimum 3D bounding box needed to cover all the labeled 2D bounding boxes in the required volume. Different illustrative examples of 3D prescription along different orientations were considered in this work: 3D axial prescription covers the torso in the anterior/posterior (A/P) and right/left (R/L) dimensions and the liver in superior/inferior (S/I); 3D coronal prescription covers the torso and the arms in the R/L dimension and at the level of the liver in S/I and the liver in A/P; 3D

sagittal prescription covers the torso in the A/P and S/I dimensions and the liver in R/L. 3D prescriptions from manual annotation were calculated in a similar fashion.

2.2.5 Model evaluation

The performance of automated 2D object detection for each of the seven classes of labels was measured by mis-classification rate and intersection over union (IoU, the area of the intersection between the manual and automated bounding boxes divided by the area of their union), as intermediate evaluation metrics. To evaluate the performance of the subsequent automated 3D prescription, the mismatch with the manual prescription for each of the six edges of the 3D prescribed bounding box (right, left, anterior, posterior, superior, and inferior) was calculated on the remaining 20% of all patients (randomly chosen). The localizer images, where the S/I shift between manual labeling and AI predictions in 3D axial prescription was larger than 2 cm, were analyzed by a radiologist (J.S.) for subjective evaluation of the causes of errors. Furthermore, the percentage of the 3D volume from manual labeling that was covered by the AI-based prescription was reported as the overlap between AI and manual labeling. The performance of the proposed method was evaluated across patients, pathologies, field strengths and sequences with varying training sizes, full and tiny architectures, with and without data augmentation schemes, and against inter-reader reproducibility results**.** In this work, the ability to detect the liver's S/I edges was given particular focus because the S/I edges are expected to be essential to detect for automated prescription of subsequent axial series (which are common in liver imaging).

2.2.6 Online implementation and prospective study

The automated prescription was implemented for axial prescription on a clinical 3T MR system (MR750, GE Healthcare, Waukesha, WI), and evaluated prospectively on healthy

volunteers using different localizer pulse sequences (single-shot fast spin-echo, SSFSE; gradient-echo, GRE; balanced steady-state free-precession, bSSFP) and acquisition parameters. To run the neural networks for prediction during the scan, the trained network weights were converted into *TensorFlow*, and *Python* scripts for image pre-processing were integrated into a GE Healthcare investigational automated workflow testing platform(95). Using this platform, after selecting the localizer and the organ to prescribe to, with a single button push DICOM images were passed to the platform and processed (image intensity normalized from the highest intensity pixel and scaled to 0-255), the coordinates of the prescribed field of view were generated and returned, and the scan prescription was updated. In this implementation, the in-plane field-of-view size remained fixed as determined by the user, while the center of FOV and the prescribed volume and the number of axial slices were determined automatically. Once the automated prescriptions were determined, operators (R.G. and C.J.B.) at the console assessed whether the automated prescriptions needed modification in order to proceed to the subsequent scans. This assessment by the operators was recorded for each exam.

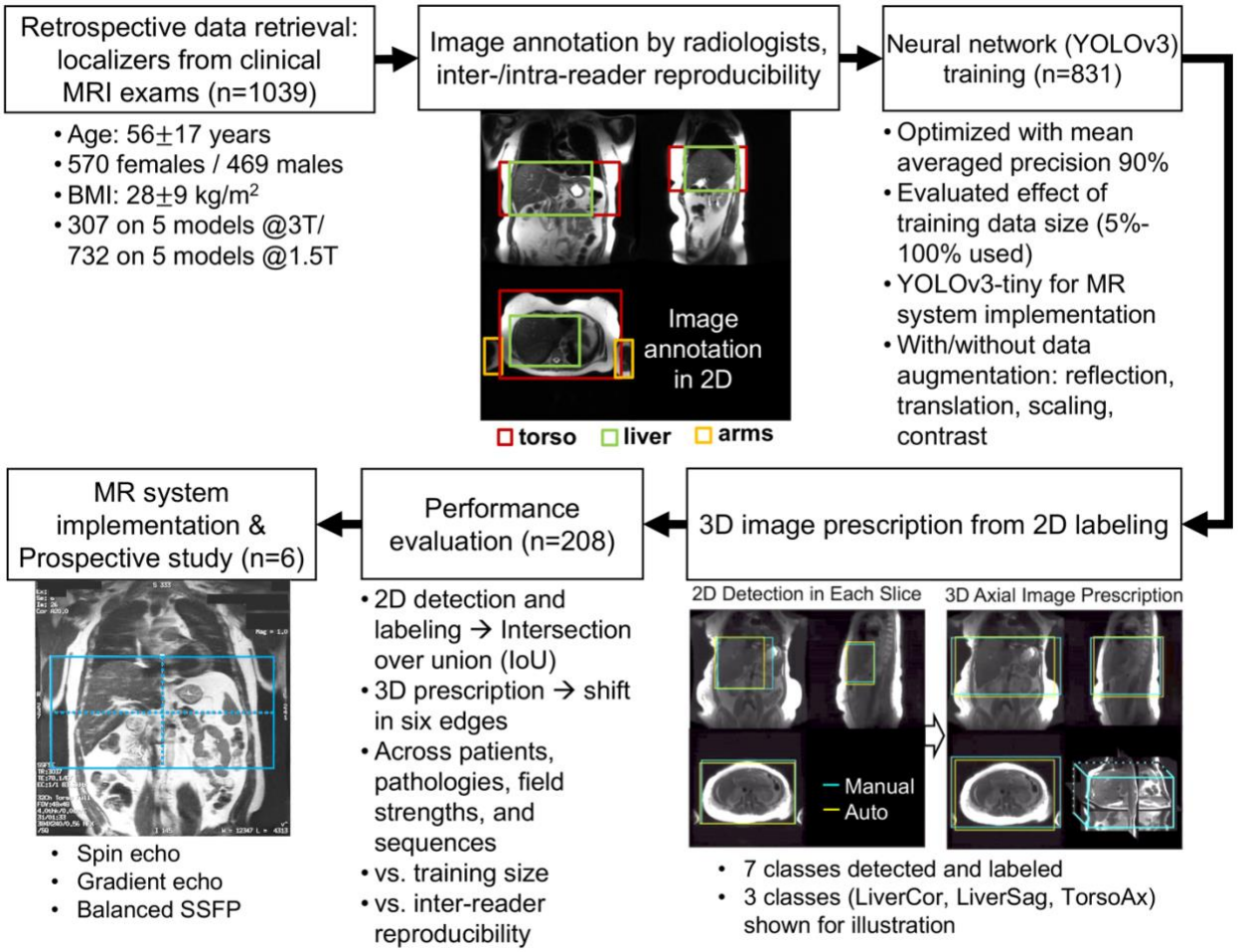

Figure 3. Flow-chat summary for data retrieval, annotation, training, prescription, evaluation, and scanner implementation. *Manual labeling consisted of 7 localization regions (LiverAx, TorsoAx, ArmsAx, LiverCor, TorsoCor, LiverSag, TorsoSag) that was evaluated by assessment of inter-reader reproducibility. A convolutional neural network (CNN) for object detection was trained with 80% of the datasets. The minimum 3D box needed to cover the appropriate labeled 2D boxes was used to obtain the final 3D automated prescription. Evaluation of 2D and 3D boxes was performed on the remaining 20% datasets across patients, pathologies, and acquisition settings. We successfully implemented the method on a clinical MR system and conducted a prospective study with 6 healthy volunteers across acquisition sequences. LiverAx/TorsoAx/ArmsAx: liver/torso/arms in the axial view; LiverCor/TorsoCor: liver/torso in the coronal view; LiverSag/TorsoSag: liver/torso in the sagittal view.*

2.2.7 Statistical analysis

In the testing datasets from the retrospective study in patients, the performance of the full network trained without any augmentation in various sub-cohort across age, sex, BMI, pathology, acquisition field strength and localizer pulse sequence was measured by the overlap

between AI and manual labeling for 3D liver detection and axial prescription. In the same dataset, the performance of the networks with various training settings (full vs. tiny, with/without augmentation) was measured by the mis-classification rate and IoU in 2D detection from individual slices, and the overlap between manual labeling and AI prediction in 3D liver detection and axial, coronal, and sagittal prescriptions. Paired t-tests were conducted to evaluate the statistical significance of performance difference between the trained networks with a threshold of 0.05. Further, the median and inter-quartile range (IQR) of the same performance metrics for the trained networks was compared against the inter- and intra-reader reproducibility of the two radiologists.

In the prospective study in healthy volunteers, the performance of both the full and tiny networks trained without any augmentation was measured by the overlap between manual labeling and AI prediction in 3D liver detection and axial prescriptions across scans acquired with SSFSE, GRE, and bSSFP sequences with various parameters.

2.3 Results

Demo code and the YOLOv3 weights obtained after training for this work are shared in the following Zenodo repository: https://doi.org/10.5281/zenodo.7391054.

Overall, 7820 GA MRI examinations were identified, performed in 5351 patients (3022 women and 2329 men). Of the 5351 patients identified, 2285 had their BMI recorded within 30 days of one of their scans. Out of the 2285 exams with patient BMI recorded within 30 days of the scan, 1039 were used for manual annotation and model training and testing. A total of 1,039 exams from 1,039 patients (age 56±17 years, range 0-101 years, 570 females/469 males, BMI 28±9 kg/m^2) were collected. **Table 1** summarizes the distribution of the patients included in terms of age, sex, BMI, pathology, acquisition field strength and sequence. The localizer

acquisitions were based on SSFSE (1,015 exams, 98%) and GRE (24 exams, 2%). Training and validation involved 21,274 localizer slices from 748 patients and 1,850 slices from 83 patients (randomly chosen from all patient datasets). With full augmentation, 2,537,390/268,320 images were used for training/validation of the tiny network. The performance of the proposed method was evaluated on 5,655 localizer slices from the remaining 208 patients. **Figure 3** summarizes the data used in this study.

Training of the full network with all training data required ~40 hours (NVIDIA Tesla V100), to reach an mAP of 90% at an IoU threshold of 0.5. With augmentation using reflection, training took ~90 hours. Training of the tiny network with all training data required ~6 hours on the same GPU (~20 hours with reflection, ~150 hours with the full augmentation scheme). For testing, object detection for one entire three-plane localizer (~30 images) on a GPU required ~0.3/0.1 seconds for the full/tiny network.

Figure 4 shows representative examples of 3D detection of the liver in a patient with a normal liver, and in five patients with various representative liver pathologies including focal lesions, iron overload, ascites, and cirrhosis.

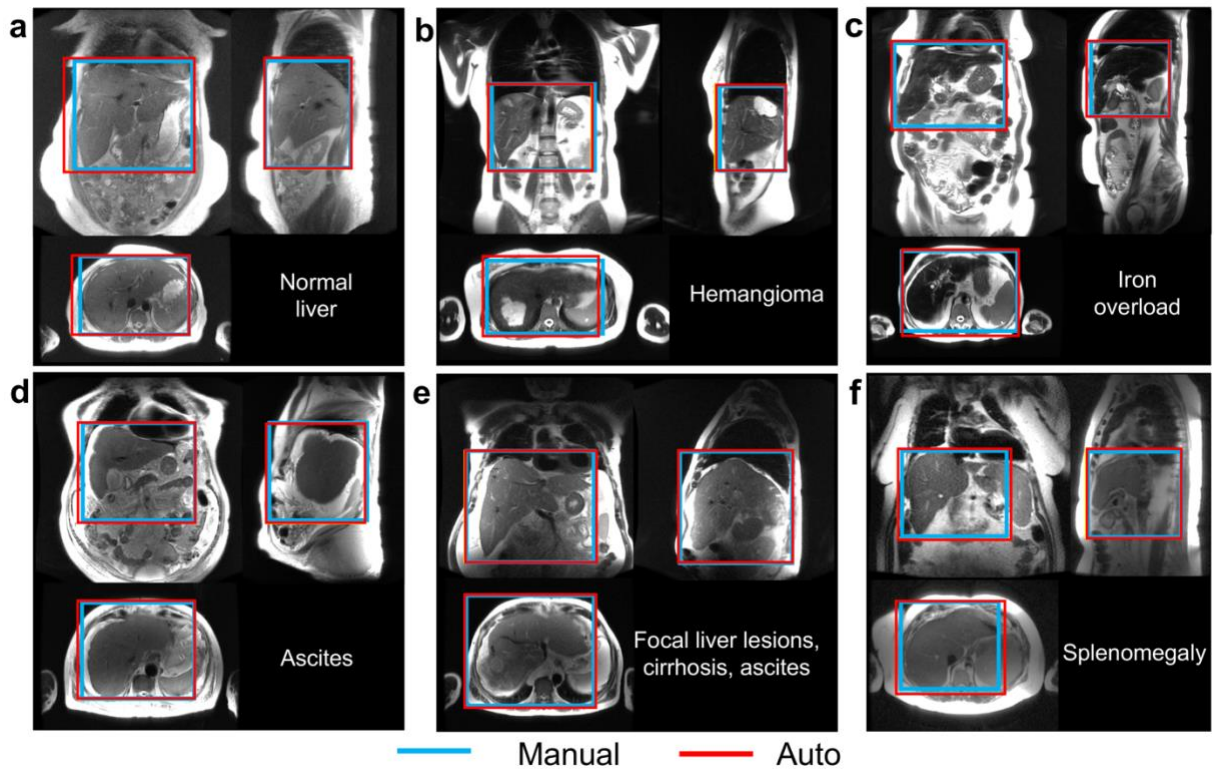

Figure 4. 3D detection of the liver in all three localizer orientations, with examples of common pathologies. *a) In most cases, the liver volume was covered accurately by automated prescription. The automated prescription aligned well with the manual annotation in patients with focal lesions (b), iron overload (c), ascites (d), and/or cirrhosis (e), as well as in a patient with splenomegaly (f), where the spleen abuts the liver and its signal level is similar to that of liver, but the proposed method was still able to identify the liver correctly.*

The automated liver detection failed to detect the entirety of the liver with tight margins (2 cm S/I) when localizer slices missed a large portion of the liver and/or provided insufficient signal due to dielectric shading (**Figure 5**). When the axial localizer images did not cover the liver sufficiently (a), missed prescription of the left lobe was observed due to failed R/L range cross-checking across views. However, 3D axial prescription of this case was entirely adequate (overlap with manual annotation >90%) owing to correct torso detection. Inaccurate automated object detection (b, c) was observed for patients with multiple cysts (b,c), where dielectric shading(96) led to signal dropouts in a large portion of the localizer slices. Inconsistencies in

manual annotation between two radiologists and even between repeated annotations by the same radiologist appeared in the more severe case (c).

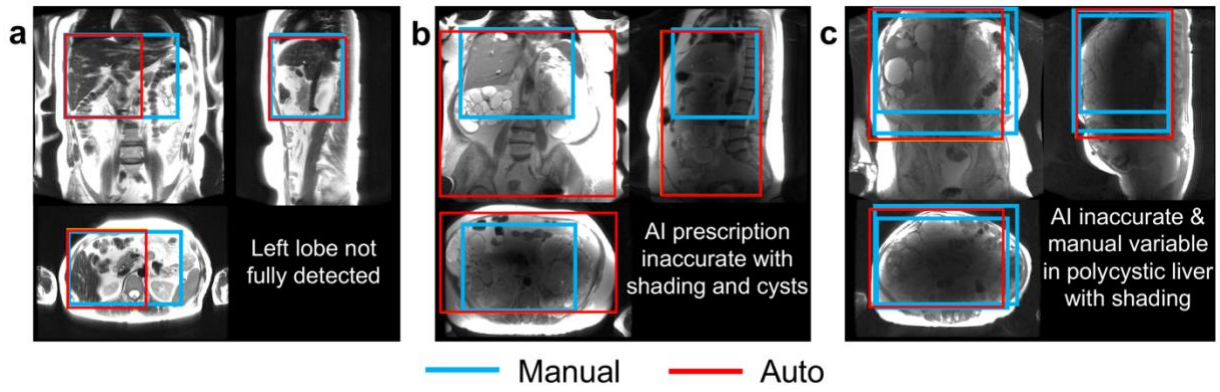

Figure 5. Examples of algorithm failures for 3D liver detection. *a) Missed coverage in the tip of the lateral segment of the left lobe due to insufficient axial localizer slices. Inaccurate automated object detection was observed for patients with multiple renal cysts (b) or liver cysts (c), or with dielectric shading (b,c) with signal dropouts in the central portion of multiple localizer images. Variation in manual annotation between two radiologists and even between repeated efforts by the same radiologist was observed in severe cases such as (c).*

The accuracy of automated 2D and 3D detection and prescription as measured by the mismatch in each dimension is shown in **Figure 6**. Each of the seven classes had a median IoU>0.91 with interquartile range (IQR) <0.09. The performance of the full YOLOv3 network (without any augmentation) in 3D liver detection and axial, coronal, and sagittal prescription was comparable to that of inter-reader reproducibility. For 3D liver detection, the percentage of manual volume included in the automated prescription had median = 97.6% and IQR = 6.5% while the percentage of manual volume from one radiologist included in the other had median = 97.0% and IQR = 5.0%. The overlap for 3D axial prescription by the full network had median = 98.5% and IQR = 3.0% while the inter-reader reproducibility performance had median = 97.1% and IQR = 1.9%. The maximum S/I shift for 3D axial prescription by the full network was 2.3 cm for 99.5% of the test datasets, while that for the inter-reader reproducibility was 2.4 cm. The

overlap for 3D coronal prescription by the full network had median = 98.3% and IQR = 3.8%, while the inter-reader reproducibility performance had median = 97.7% and IQR = 2.2%. The overlap for 3D sagittal prescription by the full network had median =97.9% and IQR = 5.5%, while the inter-reader reproducibility performance had median = 97.3% and IQR = 3.6%. In addition, for the full network the overlap for 3D axial prescription was significantly higher than the overlap for 3D liver detection.

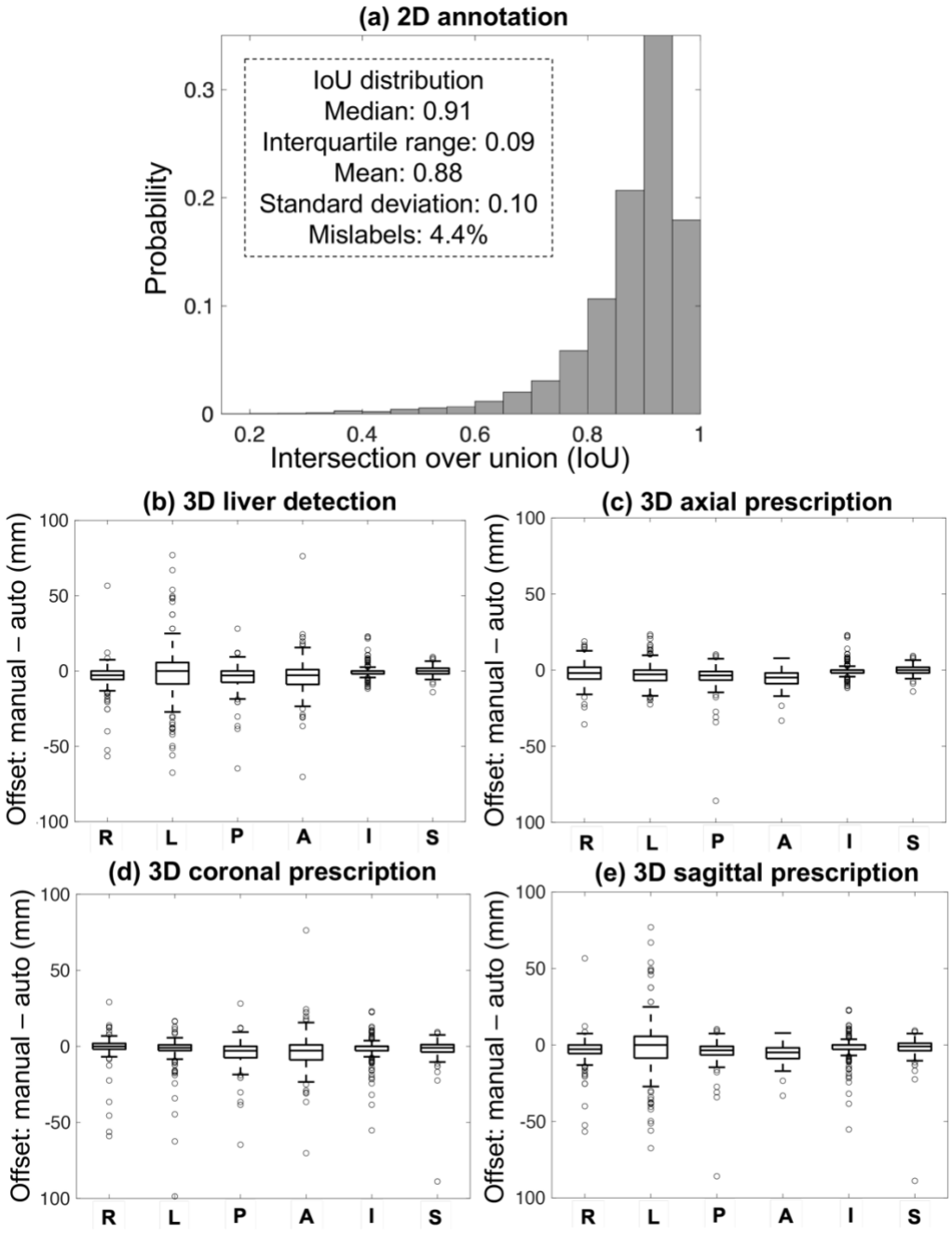

Figure 6. Accuracy of 2D annotation *across all label classes (a), 3D liver detection (b), and 3D image prescription (c-e). IoU histograms for all classes are qualitatively similar, with IoU median >0.91 and interquartile range <0.09. In (b-e), x axis shows the 6 edges: right (R), left (L), posterior (P), anterior (A), inferior (I), and superior (S); y axis shows the difference between automated and manual volumes (0: perfect alignment; negative offset: AI covering more volume; positive offset: missed volume). All boxes are tight around 0. For 3D axial prescription, the shift in the S/I dimension was less than 2.3 cm for 99.5% of the test datasets.*

For 2D detection with the full network, IoU histograms for different classes as well as the combined histogram followed similar trends. IoU median, IQR, mean, and standard deviation were similar across classes. Liver detection had a lower mis-classification rate than torso detection in all orientations, while 2D detection of the arms in the axial orientation had the highest mis-classification rate. Liver detection in the coronal and sagittal orientations had a mis-classification rate of ~1%.

The performance of the AI-based liver prescription for 3D liver detection and 3D axial prescription across sub-cohorts in age, sex, BMI, pathology, and acquisition field strength and sequence is shown in **Table 1**. For both 3D liver detection and 3D axial prescription, the overlap between AI and manual labeling was observed across all sub-cohorts was larger than 91%. 3D axial prescription had higher levels of overlap between AI and manual methods than 3D liver detection across all categories. The accuracy of AI-based liver detection was lower in the presence of iron overload (signal dropouts), partial liver resection, anatomical variation, or perihepatic pathologies such as pleural effusion or ascites. 3D axial prescription had an overlap of larger than 95% between AI and manual labeling across all pathologies.

As training size increased, the percentage of test cases with an overlap larger than 90% in 3D between AI and manual prescription increased for 3D liver detection and axial prescription (**Figure 7**). AI performance for 3D axial prescription plateaued after training with 500 datasets. AI performance for 3D liver detection approached but never reached inter-radiologist reproducibility. Training with $\geq$ 250 datasets, AI-based 3D axial prescription performed better than (manual) inter-reader reproducibility.

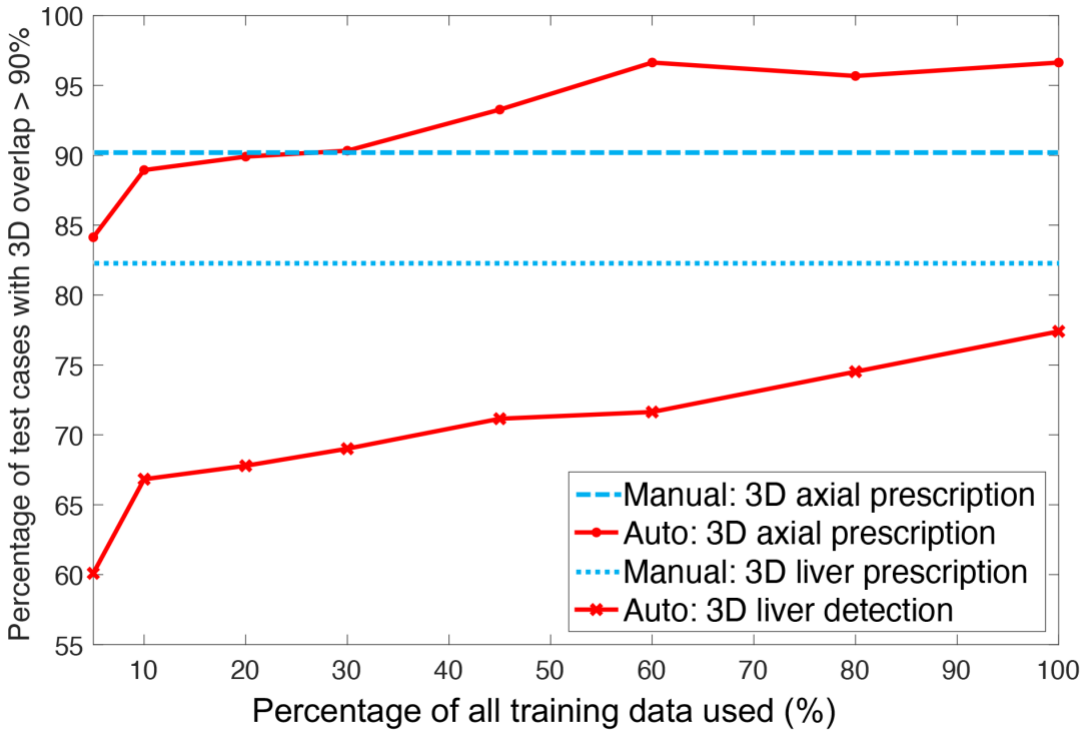

Figure 7. AI performance vs. training size. *As training size increased, the percentage of test cases with high overlap (>90%) in 3D between AI and manual prescription increased for 3D liver detection and axial prescription. AI performance for 3D axial prescription plateaued after training with 500 patients' datasets (60% of training data). AI performance for 3D liver detection approached but never reached radiologists' inter-reader reproducibility performance. Training with at least 250 datasets (30% of training data), AI-based 3D axial prescription performed better than (manual) inter-reader reproducibility.*

Table 2 shows the testing results with various training settings including the tiny and full networks. Overall, the tiny network performance was significantly inferior to the full network for 3D axial prescription. Without any augmentation, the tiny network had an overlap of median = 96.7% and IQR = 6.2%, 95.3%±6.3%, 96.3%±6.1%, 96.5%±5.8% in 3D liver detection, axial, coronal, and sagittal prescriptions, respectively. The maximum S/I shift for 3D axial prescription by the tiny network for 99.5% of the test datasets was 2.3 cm (the same as for the full network). Although augmentation methods reduced the mis-classification rate in individual slices, these augmentation methods did not significantly improve the performance of 3D prescription for

either the full (p = 0.23 for 3D axial prescription) or the tiny network (p = 0.26 for 3D axial prescription). Finally, the full network's mis-classification rate in 2D detection was low and comparable to that of the intra- and inter-reader reproducibility studies.

We successfully implemented the AI-based automated image prescription method with both the full and tiny YOLOv3 networks on a clinical MR system (GE MR750) at the site of this study. Automated image prescription for an entire three-plane localizer dataset on the MRI system CPU required ~10 seconds with the full network and ~3 seconds with the tiny network. For the six volunteers in this study, the online 3D axial prescription was performed by the tiny network to determine the prescription for the subsequent series. In all six volunteers, the whole liver was covered with visually adequate placement. The online AI axial prescriptions were accepted by the operators (R.G. and C.J.B.) at the console without modifications to proceed to the subsequent scans. This allowed for fully automated prescription within 10 seconds (including time for AI prediction and review by the operator) of the previous scan completion.

The prospective performance of the AI-based 3D axial prescription in healthy volunteers was similar to that of the retrospective study, using both the tiny network (

Sequences		**3D Liver Detection** overlap between AI and manual (%)		**3D Axial Prescription** overlap between AI and manual (%)	
		Median	IQR	Median	IQR
SSFSE	TE=40ms	94.74	15.77	96.39	9.54
	TE=80ms	97.36	12.24	97.65	1.58
	TE=120ms	89.33	15.95	98.20	15.33
GRE	Flip angle=20	87.26	10.52	85.01	15.79
	Flip angle=30	86.30	9.38	94.25	6.34
	Flip angle=60	79.74	26.51	87.33	13.90
	IR-prep	85.56	19.33	84.54	14.11
bSSFP	In phase	91.38	22.82	93.85	14.12
	Out of phase	88.44	12.56	92.09	7.94
Overall		89.18	14.55	92.12	13.23

Table 3*) and the full network. For 3D liver detection, the percentage of manual volume included in the automated prescription by the full network had median = 89.2% and IQR = 14.6%. The overlap for 3D axial prescription by the full network had median = 92.1% and IQR = 13.2%. The 3D liver detection and axial prescription with both networks had overlaps > 80% with all three types of localizer sequences: SSFSE, GRE, and bSSFP, acquired with various parameters (*

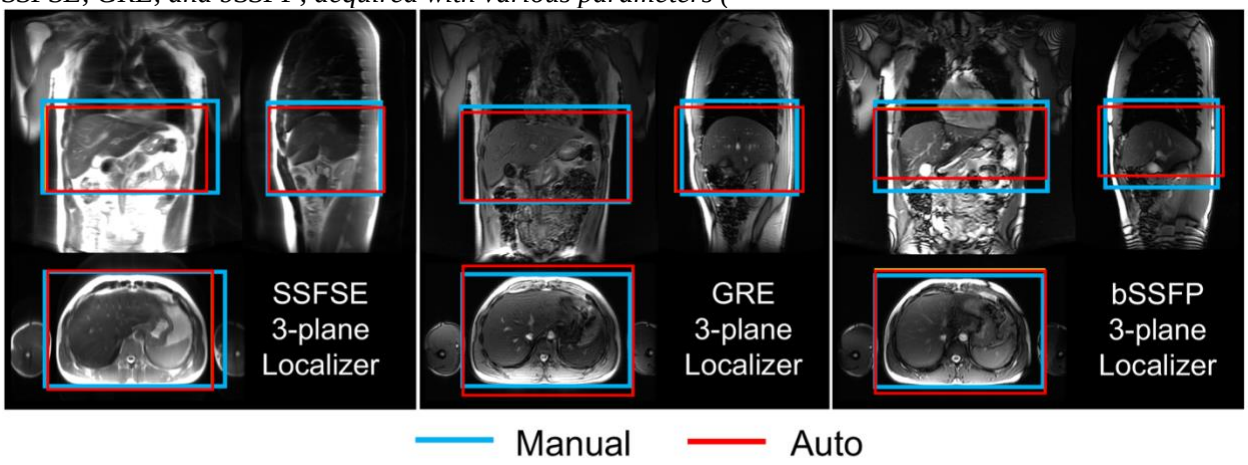

Figure 8). Nevertheless, AI performed best with SSFSE acquisitions (

Sequences		**3D Liver Detection** overlap between AI and manual (%)		**3D Axial Prescription** overlap between AI and manual (%)	
		Median	IQR	Median	IQR
SSFSE	TE=40ms	94.74	15.77	96.39	9.54
	TE=80ms	97.36	12.24	97.65	1.58
	TE=120ms	89.33	15.95	98.20	15.33
GRE	Flip angle=20	87.26	10.52	85.01	15.79
	Flip angle=30	86.30	9.38	94.25	6.34
	Flip angle=60	79.74	26.51	87.33	13.90
	IR-prep	85.56	19.33	84.54	14.11
bSSFP	In phase	91.38	22.82	93.85	14.12
	Out of phase	88.44	12.56	92.09	7.94
Overall		89.18	14.55	92.12	13.23

Table 3). The performance of both networks had no significant difference (p = 0.06) in 3D axial prescription across the various acquisition settings in the six healthy volunteers.

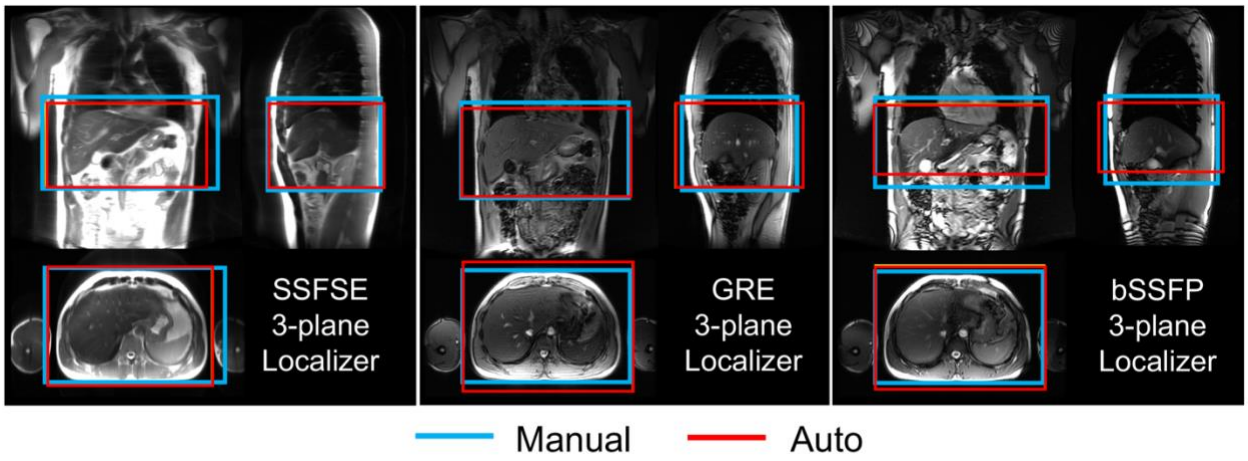

Figure 8. The AI-based automated image prescription was successfully implemented on a clinical MRI system for prospective scanning. *This online implementation performed well across various localizer sequences for 6 healthy volunteers. Automated prescription demonstrated promising performance for 3D axial prescription (similar to that of the retrospective study) across SSFSE, GRE, and bSSFP sequences with various parameters. The performance of AI-based automated prescription was best when using spin-echo (SSFSE) acquisitions.*

Sub-cohorts		Number of patients			3D Liver Detection overlap between AI and manual (%)		3D Axial Prescription overlap between AI and manual (%)	
		Overall	Training	Testing	Median	IQR	Median	IQR
Age	<21	29	18	11	96.95	5.29	99.53	1.50
	21-45	245	197	48	95.17	6.97	97.55	4.85
	>45	765	616	149	97.04	8.53	98.45	3.14
Sex	Male	469	373	96	97.29	8.89	99.31	2.68
	Female	570	458	112	95.95	7.15	97.68	3.58
BMI	<18.5	49	36	13	94.82	4.88	98.66	4.80
	18.5-24.9	364	295	69	95.36	13.69	97.63	4.12
	25.0-29.9	319	263	56	97.68	6.82	99.17	2.47
	≥ 30	307	237	70	97.04	6.43	98.28	3.17
Pathology*	Cirrhosis	131	105	26	97.60	4.79	99.72	2.37
	Iron overload	71	56	15	93.84	7.67	100.0	2.41
	Metastasis	353	297	56	96.25	9.86	98.61	3.15
	Steatosis	312	253	59	96.67	6.64	98.26	4.07
	Ascites	309	246	63	96.28	7.96	98.70	3.18
	Resection	39	28	11	91.90	6.98	97.96	3.28
	Pleural effusion	159	125	34	95.33	13.76	98.46	5.03
Field strength	1.5T	732	589	143	96.28	8.37	98.38	3.82
	3T	307	242	65	96.50	6.60	98.30	2.67
Sequence	SSFSE**	1015	809	206	96.40	8.04	98.35	3.20
	GRE	24	22	2	92.20	15.61	95.44	9.13
Overall		1039	831	208	97.62	6.51	98.48	3.00

*Pathology information was automatically extracted from medical reports using keyword matching. Actual case counts may be different from reported here.

**SSFSE: single-shot fast spin-echo; GRE: gradient-echo

Table 1. Distribution of patient datasets and testing results across age, sex, BMI, pathology, acquisition field strength and localizer pulse sequence. *Overlap between AI and manual labeling for 3D liver detection and axial prescription was high (>91%) across all categories. 3D axial prescription had higher levels of overlap between AI and manual methods than 3D liver detection across all categories. While AI-based liver detection faced challenges in iron overload (signal dropouts), resection and pleural effusion (unusual anatomy), 3D axial prescription maintained high overlap (>95%) between AI and manual labeling across all pathologies. Overlap: percentage of 3D volume from manual labeling covered by AI prescription.*

		Full network		Tiny network			Reproducibility of manual annotation	
		-	+ reflection	-	+ reflection	+ all augmentation	Inter-reader	Intra-reader
2D Annotation IoU between AI and manual (%)	Mis-classify	4.39	3.86	9.45	9.92	6.73	6.72	4.43
	Median	91.26	92.21	88.21	88.01	89.67	95.87	96.64
	IQR	8.90	8.37	10.08	10.72	10.66	4.69	5.03
3D Liver Detection overlap between AI and manual (%)	Median	97.62	97.66	96.65	97.17	95.17	97.02	98.91
	IQR	6.51	6.52	6.16	6.49	7.49	4.96	2.46
3D Axial Prescription overlap between AI and manual (%)	Median	98.48	98.41	95.26	95.62	96.51	97.09	99.05
	IQR	3.00	2.89	6.27	5.59	5.27	1.87	1.68
	S/I Shift for ≥99.5% patients	2.3cm	2.3cm	2.3cm	4.0cm	4.6cm	2.4cm	1.3cm
3D Coronal Prescription overlap between AI and manual (%)	Median	98.32	98.17	96.30	96.91	95.95	97.73	98.71
	IQR	3.76	3.71	6.13	5.13	5.65	2.18	2.25
3D Sagittal Prescription overlap between AI and manual (%)	Median	97.89	97.90	96.53	96.92	96.55	97.31	99.53
	IQR	5.50	5.37	5.79	5.92	6.79	3.64	1.29

Table 2. Testing results with various training settings and inter- and intra-reader reproducibility. *The full YOLOv3 network performed better than the tiny network. Although augmentation methods such as reflection and translation/scaling/contrast reduced the mis-classification rate in individual slices, these augmentation methods did not improve the performance of 3D image prescription for either the full or the tiny network. Compared to the performance of the readers (radiologists), the full network's mis-classification rate in 2D detection was low and on par with the disagreement rate from the intra- and inter-reader reproducibility studies. The full network's performance in 3D liver detection and axial, coronal, and sagittal prescription was comparable to that of inter-reader reproducibility. Overlap: percentage of 3D volume from manual labeling covered by AI prescription.*

Sequences		3D Liver Detection overlap between AI and manual (%)		3D Axial Prescription overlap between AI and manual (%)	
		Median	IQR	Median	IQR
SSFSE	TE=40ms	94.74	15.77	96.39	9.54
	TE=80ms	97.36	12.24	97.65	1.58
	TE=120ms	89.33	15.95	98.20	15.33
GRE	Flip angle=20	87.26	10.52	85.01	15.79
	Flip angle=30	86.30	9.38	94.25	6.34
	Flip angle=60	79.74	26.51	87.33	13.90
	IR-prep	85.56	19.33	84.54	14.11
bSSFP	In phase	91.38	22.82	93.85	14.12
	Out of phase	88.44	12.56	92.09	7.94
Overall		89.18	14.55	92.12	13.23

Table 3. Testing results for prospective study using the tiny network trained without any augmentation. *The online implementation worked well across various localizer sequences for 6 healthy volunteers. Automated prescription demonstrated promising performance (similar to that of the retrospective study) across SSFSE, GRE, and bSSFP sequences with various parameters. The performance of AI-based prescription was best for SSFSE acquisitions. Overlap: percentage of 3D volume from manual labeling covered by AI prescription.*

2.4 Discussion

This work proposed an AI-based automated liver image prescription method for abdominal MRI. The proposed method performed well across patients, pathologies, and clinically relevant acquisition settings (spin echo and gradient echo localizers at 1.5T and 3T) in a retrospective study. Further, prospective implementation on a 3T clinical MR system demonstrated rapid and accurate prospective performance in a pilot study with a limited number of healthy volunteers. Importantly, the AI-based automated liver prescription had a performance level comparable to radiologists' inter-reader reproducibility. This method has the potential to enable automated, efficient, and reproducible image prescription for liver MRI.

The trained networks demonstrated excellent performance for 2D detection of the liver, torso, and the arms from individual localizer slices. However, 2D detection performance was only an intermediate evaluation metric in this study. Thanks to redundancy across multiple slices and orthogonal views, 3D prescription was minimally affected by occasional detection errors in single slices. Importantly, the shift in 3D axial prescription in the testing dataset was less than 2.3 cm in the S/I dimension for 99.5% of the test datasets. This indicates that the addition of narrow safety margins would ensure complete liver coverage in effectively all patients, at the cost of slightly longer acquisitions to cover these safety margins. Finally, although the network was trained primarily with SSFSE localizers, the method performed well with other localizer methods (GRE, bSSFP) with different parameters, suggesting generalizable application across various localizer acquisitions.

There are relevant previous preliminary efforts towards automated scan prescription in the liver using traditional object detection methods(79). The method based on liver-only bounding boxes could only perform axial prescription, while the proposed method has the capability to enable liver image prescription in any orthogonal orientation thanks to the inclusion of torso and arms classes. Importantly, this previous method requires a specialized volumetric, breath-held localizer scan, while the proposed method does not add any additional scan and is based on conventionally acquired localizers. In addition, the previous method has been tested in limited numbers of healthy volunteers (n = 24) and simulated deformed livers (n = 7) while the proposed method has been tested in 208 patients with various pathologies in the liver. The proposed AI-based method may be more robust than the previous method in terms of testing performance. In 24 healthy volunteers, the detection errors of the previous method to detect the upper and lower edges of the liver were 1.87±2.04 mm and −0.90±7.84 mm, respectively(8). The

detection errors of the proposed method in 208 patients for the upper and lower edges were 0.31±3.53 mm and −0.68±12.52 mm, respectively. The performance of the proposed method is similar to recent developments in automated organ detection for kidney and spine using YOLOv3-based networks(23, 83). After training with datasets of 14 patients and testing with 41, the reported metrics for 2D detection of kidneys in CT were: average IoU = 0.769 and Dice coefficient = 0.851(83). Detection of intervertebral discs (IVD) in lumbar spine MRI, trained with datasets of 19 patients and tested with 18, obtained a Dice coefficient = 0.839(23). Likely as a result of the larger, diverse training dataset in this study, the IoU and Dice coefficient are both higher (0.878 ± 0.122 and 0.935 ± 0.069). In addition, the object mis-classification rate of the liver of the proposed method (1-4%) is comparable to that in a recent study using a modified YOLOv3 network trained with 5,986 abdominal (axial) CT images (~3%)(92).

This work relied on YOLO, a state-of-the-art and robust object detection system(91). Alternative networks include Single Shot Detector (SSD) and Faster R-CNN(97–99). YOLO and SSD have the advantage of real-time object detection(97). YOLO-based models have been applied to localization of organs with normal activity in 3D PET scans, detection of lung nodules, and detection of the nasal cavity in CT scans, with excellent robustness, speed and accuracy(100–102). YOLOv3 and SSD have shown similar accuracy, but YOLOv3 is about three times faster(83, 91).

The proposed approach presents several important network and workflow design considerations. Among various training settings, the tiny network, with much shallower architecture, showed slightly inferior performance to the full network. However, the 3x speedup of prediction time compared to the full network may make it a practical choice for implementation on current clinical MR systems. Additionally, the current workflow used a single

network for all localizer image orientations. Alternatively, one might train a different network for each localizer slice orientation. An important advantage of the current single-network approach is approximately 3x faster prediction for the current MR system implementation, compared to using three networks.

This work has several limitations. Confounding conditions such as multiple cysts, ascites, soft tissue edema, and iron overload, where B1-inhomogeneity leads to dielectric shading artifacts, pose a challenge for automated (and even manual) organ detection in the abdomen(96). Due to the limited number of failure cases with such conditions and artifacts in the testing dataset, the specific cause of detection failures is unknown. Furthermore, the quality of manual and automatic annotation in these cases may be limited by the fixed window/leveling of the input images. Although this did not appear to be a limitation in most cases, dynamic window/leveling may improve the quality of the manual and automatic annotation and provide a more accurate performance assessment. Importantly, this study relied on data from a single center and a single vendor. Finally, the prospective pilot study on a clinical MR system demonstrated promising performance, but only on a small number of healthy subjects.

Training and evaluation of the proposed method using multi-center and multi-vendor data with a wider variety of patient datasets are needed as future work. Evaluation of the model performance for centers that prioritize fast acquisitions and use fewer images per plane for the localizers is needed as future work. More cases with severe dielectric shading and iron overload from other vendors can be collected for training and testing to broaden the applicability of the algorithm. In this study, simple definitions of liver coverage for 3D prescription in axial, coronal, and sagittal orientations were used for illustration. Additional coverage considerations in each orientation can easily be included subsequently. Finally, in this study experienced radiologists

(rather than technologists) performed the labeling to train and demonstrate the performance of AI using the best possible manual labeling as the reference. In clinical practice, technologists typically prescribe the field of view for a given patient exam. Future studies aimed at measuring and comparing the inter-reader variability of technologists with AI performance are needed. A previous study showed that a commercial platform (Day optimizing throughput [Dot] engine, Siemens Healthineers, Forchheim, Germany) for automated image prescription contributed significant time savings (2-5 minutes) for whole-body free-breathing exams(103). The effect of the proposed automated liver prescription approach on potential time savings needs to be further examined in future work. Value chain analysis from study acquisition to delivery of actionable information to clinicians and patients may be conducted to determine whether automated prescription improves patient care and workflow efficiency in Radiology departments(104–107).

2.5 Conclusion

An AI-based automated liver prescription method developed in this work has promising performance across patients, pathologies, and clinically relevant acquisition settings, well within inter-radiologist reproducibility. Further, this study demonstrated the successful prospective implementation of the method on a clinical MR system. This method has the potential to improve clinical workflow and standardization for MRI of the liver.

Chapter 3 Characterization and Correction of Cardiovascular Motion Artifacts in Diffusion-Weighted Imaging of the Pancreas

3.1 Introduction

Diffusion-weighted imaging (DWI) has the potential to add value in the detection (108–110), diagnosis(111, 112), and treatment response prediction of pancreatic diseases(12–14, 111). DWI has been shown to have a similar accuracy as contrast-enhanced MRI for the diagnosis of pancreatic cancer and pancreatic neuroendocrine tumors(9). Furthermore, quantitative measurements derived from DW images constitute promising biomarkers for pancreas imaging applications. For example, measurement of the apparent diffusion coefficient (ADC) in the pancreas has been shown to correlate well with histopathological markers, such as the proportion of collagenous fibers(40). Further, ADC measurements may enable differentiation of malignant lesions from healthy tissue(30), mass-forming pancreatitis(15, 31), and other benign lesions(32, 33). Moreover, recent studies have shown that ADC measurements can help differentiate accessory spleen from small islet cell tumors(31), differentiate near solid serous cystadenomas from neuroendocrine tumors(113), and potentially determine the tumor grade(34, 35). DWI has also shown potential to enable an early prediction of treatment response(12–14), as early therapy-induced effects can be reflected in tissue reorganization, changes in cellularity, and vascularization, or metabolic activity, before measurable changes in tumor volume become apparent. Furthermore, DWI can be useful for detecting autoimmune pancreatitis and evaluating the effect of steroid therapy(111). In addition, an increase in tumor ADC values in unresectable pancreatic cancer during chemotherapy predicts better survival(13), pancreatic ductal adenocarcinomas with lower baseline ADC respond poorly to standard chemotherapy and would benefit from intensified treatment(14), and a lower ADC obtained from high b-value DWI in

patients with advanced pancreatic cancer may be predictive of early progression in chemotherapy-treated patients(12).

Despite this potential, the ability to differentiate between malignant and benign lesions and to predict treatment response based on ADC measurements remains limited, due to substantial variability and overlap in the quantitative measurements(114, 115). ADC values for normal and diseased pancreas have shown a broad variability within studies(9, 12, 116–119), and substantial overlap in ADC values among normal and diseased pancreas and various tumor grades have been reported(7, 9, 119). In particular, the reported ADC values for the different parts (head, body, and tail) of the normal pancreas have seen large differences across studies(7, 31, 112, 116, 117, 120). This overlap and variability in ADC measurements are likely due in part to the presence of multiple technical challenges, particularly physiological motion, that affect DWI of the pancreas. Due to its location within the retroperitoneum, the pancreas may be affected by respiratory, peristaltic, and cardiovascular-related motion(38). The extent of pancreatic motion due to respiration has been studied previously(36), and is routinely addressed in DWI through respiratory triggering(8, 15). Further, peristaltic motion can be minimized through the use of gastrointestinal motility inhibitors such as glucagon(37, 121–123).

However, the effect of cardiovascular-related motion, due to both direct cardiac motion and pulsation of large blood vessels, are not understood in the context of DWI of the pancreas. Cardiovascular-induced motion of organs adjacent to the heart (e.g. the liver) or large blood vessels (e.g. the pancreas) occurs throughout the cardiac cycle(21), and therefore its effects may not be fully avoidable using cardiac gating. Conventional DWI is acquired using monopolar DW gradients with elevated motion moments (i.e. motion sensitivity), and generally leads to artifacts in the presence of cardiovascular-induced compressive motion. Indeed, cardiovascular-induced

compressive tissue motion often leads to signal dropouts and ADC bias in abdominal organs such as the liver (particularly in the left lobe)(21).

We hypothesize that, similar to the liver, cardiovascular-related motion may lead to artifacts in DWI of the pancreas and thus ADC bias. In current literature, reduction of ADC measurements from pancreatic head to tail has been observed(116, 120, 124–126). Importantly, the pancreatic head is closest to large blood vessels such as the portal vein, inferior vena cava, aorta, and mesenteric superior artery. Indeed, artery pulsation and other cardiac-related motion may lead to rapid compressive motion of pancreas tissue, leading to signal dropouts and ADC bias in conventional DWI acquisitions performed with monopolar DW gradient waveforms. Thus, the apparent ADC heterogeneity observed across the parts of the healthy pancreas in previous studies may be due to cardiovascular-induced artifacts, analogously to the heterogeneity observed across the liver lobes.

Motion-compensated (MOCO) diffusion-encoding gradient waveforms with nulled first and/or second-order gradient moments (M1, M2) have been proposed to mitigate sensitivity to bulk motion. For example, velocity-compensated (M1= 0) diffusion-encoding gradient waveforms implemented in the liver enable improved ADC reproducibility without cardiac triggering(127, 128). Importantly, conventional MOCO diffusion encoding utilizes a multipolar gradient waveform that substantially increases the echo time (TE) compared to monopolar encoding, leading to degraded SNR(26). Optimized methods for motion-robust DWI with minimized TEs have been recently proposed(26–28). These methods generally lead to asymmetric waveforms that optimally utilize the available diffusion encoding time. Although these asymmetric diffusion waveforms may introduce additional challenges (e.g., concomitant gradient effects), these challenges can be often addressed within the optimization formulation

itself (e.g., by including a concomitant gradient nulling constraint as performed in this work(27). By applying optimized motion-compensated DW gradient waveforms, these methods are able to avoid signal dropouts in the presence of cardiovascular-related motion while maximizing SNR, potentially enabling motion-robust DWI. Although motion-robust DWI methods have been demonstrated in various applications of DWI, including in liver(27, 28) and cardiac(26) imaging, their performance in the pancreas remains unknown.

Based on these observations, we hypothesize that: 1) cardiovascular-related motion leads to artifacts and bias in conventional DWI of the pancreas, and further 2) these artifacts can be mitigated through the use of recently proposed motion-robust DWI methods. Therefore, the purpose of this work is to evaluate the effects of cardiovascular-related motion on conventional DWI of the pancreas, and to assess the performance of motion-robust DWI methods in a motion phantom and in healthy volunteers.

3.2 Methods

In this IRB-approved study conducted with informed written consent, we visualized the effects of cardiovascular-related motion using cardiac-gated cine acquisitions in healthy volunteers. Next, we evaluated these effects in a custom anatomically accurate 3D-printed pancreas motion phantom using DWI under various motion conditions. Finally, we assessed the artifacts and quantified the ADC bias in the pancreas of healthy volunteers using conventional DWI, and evaluated the performance of a recently developed motion-robust DWI method(27). All scanning was performed at 3T (GE Signa Premier) using flexible coils (AIR Technology, GE Healthcare, Waukesha, WI). A safe upper bound of slew rate (150 mT/m/msec) was used for optimization, well below the peak gradient slew rate of 200 mT/m/msec. These acquisitions and analyses are described in detail next.

3.2.1 Visualization of cardiovascular-related pancreas motion

Eight healthy volunteers were scanned with cardiac-gated SSFP of the pancreas in three orthogonal orientations (coronal, parasagittal, and axial) in separate breath-holds to visualize the bulk and compressive motion of the pancreas associated with cardiovascular-related motion. For each orientation, cine images were obtained for 20 frames within the cardiac cycle. For visualization, a radiologist (J.S.) with 9 years of experience in abdominal MRI contoured the pancreas borders on each of the 20 frames acquired within the cardiac cycle.

3.2.2 Evaluation in a motion phantom

3.2.2.1 Phantom construction

A custom phantom was fabricated for testing motion-compensated diffusion MRI. This phantom consisted of an anthropomorphic hydrogel "pancreas" (see below) embedded in silicone(70). Polyacrylamide hydrogel was used for the pancreas model in order to enable tissue-mimicking compressive motion. To create the anthropomorphic hydrogel model, the pancreas was segmented from a set of T2-weighted MR images of a healthy volunteer and a 3D digital model of the pancreas was exported in STL format. The model was first 3D-printed with polyvinyl-alcohol (PVA) filament on an Ultimaker (Utrecht, Netherlands) S5 machine. The PVA pancreas was then coated in liquid latex rubber. Once the rubber coating had dried, the inner PVA pancreas volume was dissolved with water, leaving a pancreas-shaped void in a rubber shell. Hydrogel with 8% acrylamide/bis-acrylamide concentration was then poured into the rubber mold and allowed to polymerize. Once cured, the hydrogel pancreas was extracted from the rubber, placed in a water-tight container, and surrounded with silicone. Compliant tubing was then run over the top of the pancreas model and fixed within the water-tight container filled with

silicone. The ends of the tubing were then integrated into a flow loop with a pulsatile positive displacement pump (BDC PD-1100, BDC Laboratories, Wheat Ridge, CO).

3.2.2.2 Motion setup

Water was pumped through the system, causing deformation of the compliant tube and adjacent hydrogel pancreas model at a frequency of one hertz. This setup was intended to mimic the cyclic motion induced by the cardiovascular-induced compressive motion of the vessels surrounding the pancreas *in vivo*. A phantom similar to the one in the photograph was used, with opaque silicone surroundings and pancreas neck placed between the tube and the container bottom to facilitate compressive motion in the pancreas. The videos show increased flow amplitude leads to increased pulsation of the tube, causing more severe deformation of the pancreas model.

3.2.2.3 Acquisition

At various flow velocities (0.5, 1.0, 1.5, 2.0, 2.5, 3.0, 3.5, 4.0 liters/min), DW images using standard monopolar (TE = 49 ms) and optimized motion-compensated (TE = 65 ms) waveforms were acquired. Motion-compensated waveforms were designed using the Optimized Diffusion-weighting Gradient waveform Design (ODGD) method(27). In this work, ODGD was used to achieve the desired b-values with minimum TE, first order motion moment nulling and concomitant gradient (CG) nulling. For each type of gradient waveforms (monopolar and motion-compensated), three orthogonal diffusion directions were obtained, each with two b values (b = 50, 500 s/mm^2, with 2 and 4 repetitions, respectively).

3.2.2.4 Analysis

One representative slice containing the head, body, and tail of the pancreas model was selected. The DW images and ADC maps were compared between standard monopolar and

motion-compensated DW waveforms, in the absence of motion, as well as in the presence of various levels of motion. The histograms of the ADC values in the pancreas segmented within the selected slice were generated, with mean and standard deviation calculated for each histogram, to compare the ADC distributions of both waveforms.

3.2.3 Characterization and correction of motion artifacts *in vivo*

3.2.3.1 Evaluating single-slice breath-held cardiac-gated DWI

Characterization under various cardiac trigger delays: The same eight healthy volunteers scanned for the visualization of cardiovascular-related pancreas motion, were scanned with standard monopolar diffusion waveforms. To maximally control the acquisition timing relative to the cardiac cycle, single-slice DWI was acquired using breath-holding and cardiac (peripheral) gating. Based on the observations from the SSFP images, one axial slice that captured the compressive motion of adjacent vessels on the pancreatic head and one axial slice that captured most of the rest of the pancreas were used for DWI. DW images were acquired in a single end-of-expiration breath-hold. This acquisition was repeated at three cardiac trigger delays (20, 100, and 200 ms after the R wave), and in three diffusion directions using a standard monopolar waveform (TE = 50 ms), for a total of 9 breath-held monopolar DWI acquisitions per volunteer. Reduced field-of-view(129, 130) (readout × phase encode FOV = 32 cm × 12.8 cm) was used with spatial resolution of 2 mm × 2 mm × 5 mm, with b = 50, 500 s/mm^2.

Correction using motion-compensated DW waveforms: The same eight volunteers were scanned within the same exams as above, in order to evaluate the performance of motion-compensated DW waveforms. Single-slice DWI using a motion-compensated gradient waveform (first order moment nulled with CG nulling, TE = 72 ms)(27) was tested using the same parameters as the standard monopolar waveform, with trigger delay = 20 ms. Three breath-held

acquisitions were performed, one per diffusion direction. Other trigger delays were not included due to scan time limitations.

3.2.3.2 Evaluating whole-pancreas respiratory-triggered DWI

In order to evaluate clinically relevant whole-pancreas DWI acquisitions, ten healthy volunteers (with an overlap of 6 volunteers from the previous scans) were scanned. Whole-pancreas DWI was acquired using respiratory-triggering with parameters similar to our local clinical protocol, including three diffusion directions, with b = 50, 500 s/mm^2. Two separate acquisitions were performed, using standard monopolar and motion-compensated gradient waveforms, respectively. The approximate acquisition time was 4 minutes. Detailed information on imaging parameters is shown in **Table 4**. A triggering window of 30% was used to acquire all slices covering the pancreas in one respiratory interval.

3.2.4 Image analysis and measurements

ADC measurements were performed in both single-slice and whole-pancreas DWI acquisitions, each for both standard monopolar and motion-compensated diffusion waveforms. For the single-slice study, region of interest (ROI) measurements were performed on ADC maps derived from each combination of cardiac trigger delay and diffusion direction to characterize the effects of cardiovascular-related motion. Oval ROIs were drawn by a radiologist (JS) in the pancreatic head, body, and tail in the b = 50 s/mm^2 DWI images (with b = 0 s/mm^2 as an anatomical reference), then copied to the corresponding ADC map for measurement, to avoid reader bias in directly placing ROIs in the ADC maps. For the whole-pancreas study, ROI measurements were performed on ADC maps derived from the averaged DW images of all diffusion directions. Oval ROIs were drawn on the slice that included most of each pancreatic part in the b = 50 s/mm^2 DWI images (with b = 0 s/mm^2 as an anatomical reference), then copied

to the corresponding ADC map for measurement. For both studies, ROIs were drawn as large as possible in each pancreatic part while avoiding peripheral regions with susceptibility artifacts, resulting in ROI areas between 52 and 244 mm^2.

3.2.5 Statistical analysis

Paired *T*-tests were performed to evaluate the ADC differences in different parts of the pancreas for both standard monopolar and motion-compensated waveforms.

3.2.6 Effect of peristalsis

Single repetitions taken within the same breath-hold and at the same cardiac trigger delay were compared qualitatively to assess the presence of non-cardiovascular-related motion artifacts in the acquired pancreas DWI images.

	Single-slice DWI		Whole-pancreas DWI	
DWI gradient waveforms	Standard monopolar waveform	Optimized motion-compensated waveform	Standard monopolar waveform	Optimized motion-compensated waveform
Acquisition modes	BH		RT	
TR (ms)	2069	1935	5000-10000*	
TE (ms)	41.2	72.7	48.7	72.7
Cardiac Trigger Delays (ms)	20, 100, 200	20	--	
b-values (s/mm^2) (repetitions per direction)	0 (1), 50 (2), 500 (6)	50 (2), 500 (6)	50 (2), 500 (6)	
Reduced Field of view	40% in phase	100%		
Field of view	32 cm × 12.8 cm	32 cm × 32 cm		
EPI echo train length	48	60		
Effective phase encoding bandwidth	31 Hz	25 Hz		
Parallel imaging factor	1	2		
Diffusion directions	Phase, frequency, and slice (AP, RL, SI)			
In-plane resolution	2 mm × 2 mm			
Slice thickness	5 mm			
Slice spacing	1 mm			
Receiver bandwidth	± 250 kHz			
Partial Fourier	75%			

* 1-2 respiratory intervals depending on the breathing pattern of the volunteer.

Table 4. Imaging parameters used for the in-vivo study. *Single-slice DWI was acquired using breath-holding and cardiac (peripheral) gating. DW images were acquired in a single end-of-expiration breath-hold. This acquisition was repeated at three cardiac trigger delays (20, 100, and 200 ms), and in three diffusion directions using a standard monopolar waveform (TE = 50 ms). Reduced field-of-view (FOV = 40%) was used with spatial resolution = 2mm×2mm×5mm. Single-slice DWI using a motion-compensated gradient waveform (TE = 72 ms) was tested using the same parameters as standard monopolar waveform with trigger delay = 20 ms. Whole-pancreas DWI was acquired using respiratory-triggering with parameters similar to our local clinical protocol, including three diffusion directions. Two separate acquisitions were performed, using standard monopolar and motion-compensated gradient waveforms, respectively.*

3.3 Results

3.3.1 Visualization of cardiovascular-related pancreas motion

Cardiac-gated dynamic SSFP images of the pancreas in coronal, parasagittal, and axial views were acquired. Pulsation of the aorta, as well as motion near the portal vein, inferior vena cava, and splenic vein caused substantial translational and compressive motion of the pancreatic head and body.

3.3.2 Evaluation in a motion phantom

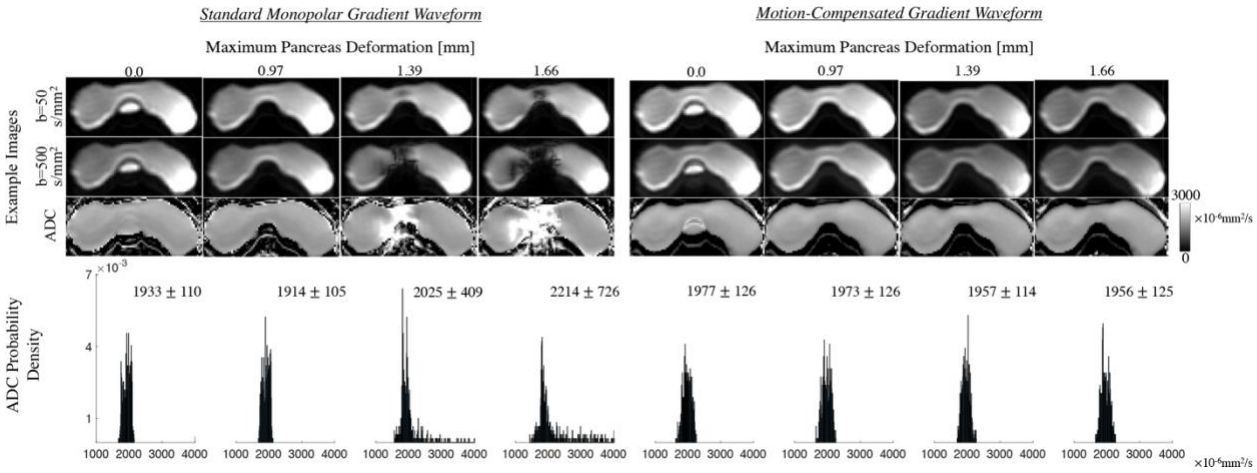

Figure 9 shows DW images and ADC maps of the pancreas motion phantom using both the standard monopolar and motion-compensated DW waveforms. In the absence of substantial motion (zero or low flow amplitude in the tube), the ADC distributions were similar between the two waveforms. In the presence of motion, the standard monopolar DW waveforms led to artifacts in both b = 50 s/mm^2 and b = 500 s/mm^2 images, as well as biased (overestimated) ADC values. The severity and extension of the artifacts and ADC bias increased with larger flow amplitude. In contrast, with motion-compensated DW waveforms, the DW signals appeared consistent regardless of the presence of motion. Further, motion-compensated DW waveforms

produced consistent and spatially uniform ADC values throughout the hydrogel pancreas model, over a wide range of flow amplitudes.

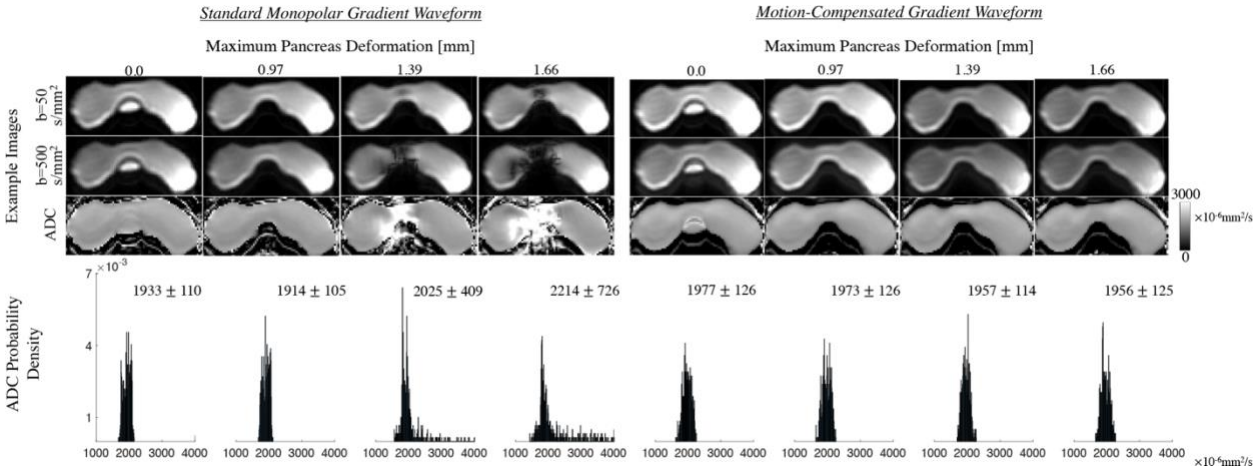

Figure 9. DW images and ADC maps of the pancreas motion phantom using both the standard monopolar and motion-compensated DW waveforms. *With the standard monopolar DW waveforms, artifacts appeared in both b = 50 s/mm^2 and b = 500 s/mm^2 images, resulting in overestimated ADC values. The severity and extension of the artifacts and ADC bias increased with larger flow amplitude in the tube. With motion-compensated DW waveforms, however, the signals in the DW images appeared consistent, producing uniform ADC values throughout the pancreas hydrogel model. With no or small pancreas deformation, the ADC distributions were similar between the two waveforms. However, with large deformation, the ADC histograms from standard waveforms were broader and shifted to higher ADC values. With motion-compensated waveforms, DW images and ADC distributions were similar regardless of the pancreas motion.*

3.3.3 Characterization and correction of motion artifacts *in vivo*

3.3.3.1 Evaluating single-slice breath-held cardiac-gated DWI

Characterization under various cardiac trigger delays: in the breath-hold study, signal dropouts occurred in DW images in all three parts of the pancreas, in all diffusion directions, and at all acquired trigger delay times. DW images of b = 500 s/mm^2 in the pancreatic head, body, and tail are shown in **Figure 10**. Contours were drawn on the b = 0 images and overlaid onto the b = 500 s/mm^2 images to indicate the location of the pancreatic head. For each acquisition and each part of the pancreas, the mean and standard deviation of the ADC measured across volunteers are noted in each sub-image. Signal dropouts were consistent across repetitions

acquired with the same cardiac phase and diffusion direction. However, dropouts appeared at different locations for images acquired at different cardiac phases (trigger delays) or in different diffusion directions. As a result of artifacts in DW images, biased ADC values with a large variation across volunteers occurred for all trigger delays and diffusion directions.

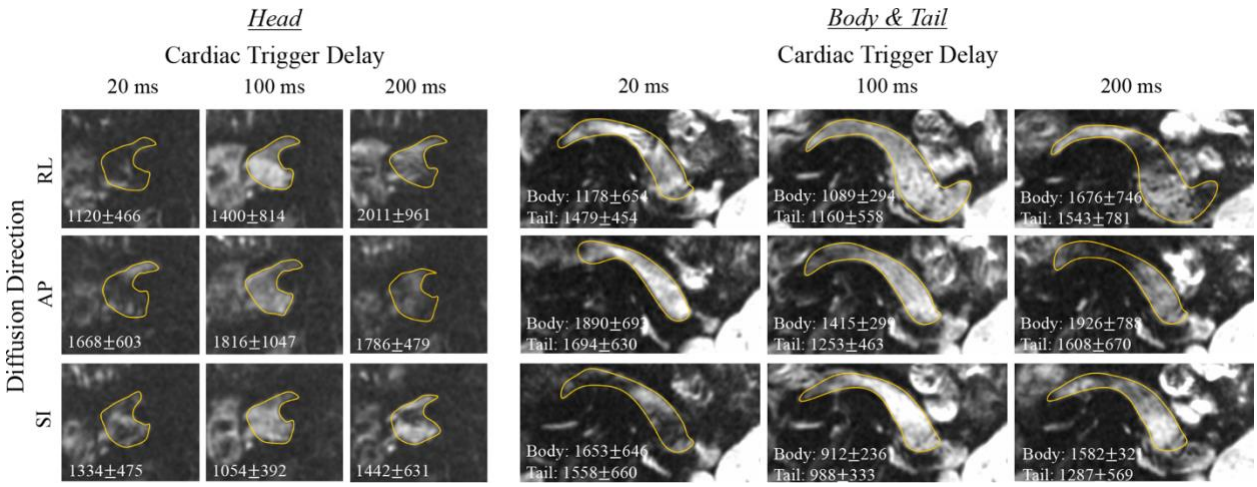

Figure 10. Single-slice monopolar-based diffusion-weighted images with b = 500 s/mm^2 in three diffusion directions. *DWI was obtained at three different cardiac trigger delays, each acquired in a separate breath hold. The yellow contours were drawn from the T2-weighted image (b = 0 s/mm^2, not shown) and overlaid on DWI b = 500 s/mm^2 to indicate pancreas location. For each acquisition and each part of the pancreas, the mean and standard deviation of the ADC measured across volunteers are noted in each sub-image. Using monopolar DW gradients, signal dropouts occurred in DWI images in all three parts of the pancreas, in all diffusion directions, and at all trigger delay times, resulting in biased ADC values with a large variation across volunteers observed for each acquisition.*

Correction using motion-compensated DW waveforms: with standard monopolar DW waveforms, heterogeneous DW signals and ADC values occurred across the pancreas for all diffusion directions (**Figure 10**). The measured ADCs had a large variability across volunteers in all three diffusion directions at a trigger delay time of 20 ms (the range of standard deviation across volunteers is 354 – 1590 $\times 10^{-6}$ mm^2/s for all parts of the pancreas and in all diffusion directions). Heterogeneous ADCs across the parts of the pancreas were observed, with significantly higher ADC in the head than in the tail ($p < .05$) in two of the diffusion directions (RL and AP) (**Figure 11**). Using a motion-compensated DW waveform, DW signals and ADC

values were uniform across the parts of the pancreas (**Figure 11**), and the measured ADCs had a much lower variability across volunteers (the standard deviation of ADC across volunteers is 63 – 279 $\times 10^{-6}$ mm^2/s for all parts of the pancreas and in all diffusion directions). Finally, motion-compensated DW waveforms led to comparable ADC in all three parts of pancreas, as shown in **Figure 12**.

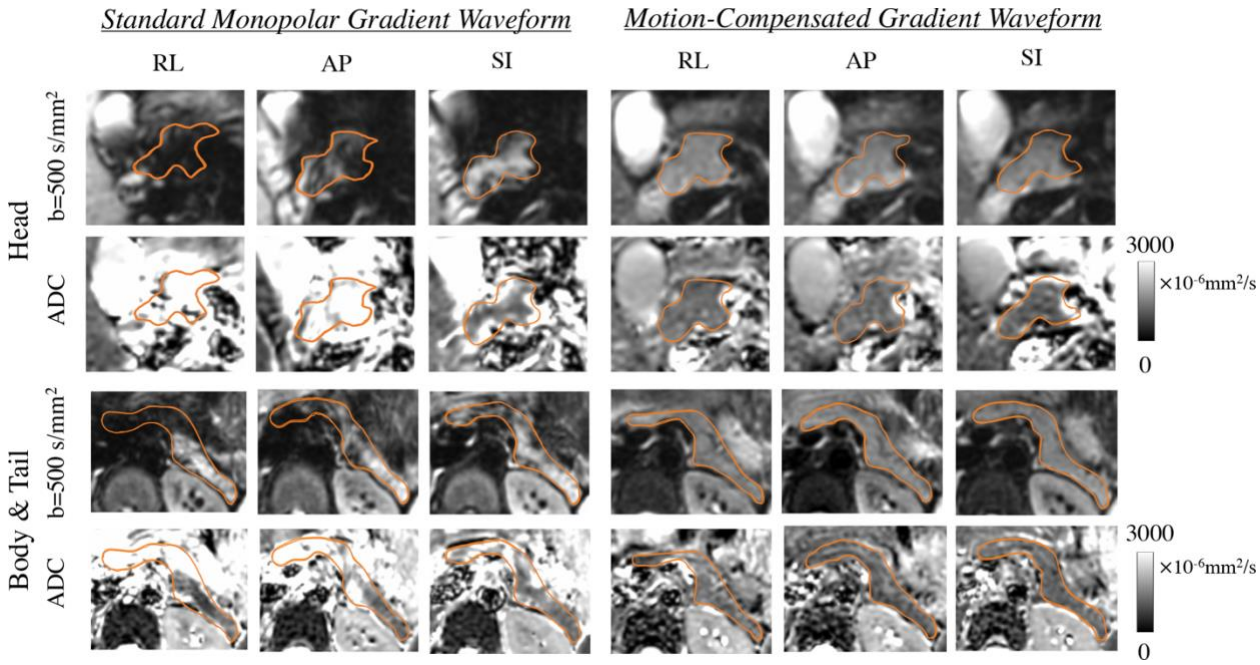

Figure 11. Single-slice breath-hold diffusion-weighted images with b = 50, 500 s/mm^2 and ADC maps in three diffusion directions, at cardiac (peripheral-gating) trigger delay = 20 ms. *The orange contours were drawn from DWI b = 50 s/mm^2 and overlaid on DWI b = 500 s/mm^2 and ADC maps to indicate pancreas location. Using a standard monopolar DW waveform, heterogeneous DW signals and ADC values were observed across the pancreas in all diffusion directions. Using a motion-compensated DW waveform, DW signals and ADC values appeared relatively uniform across the pancreas.*

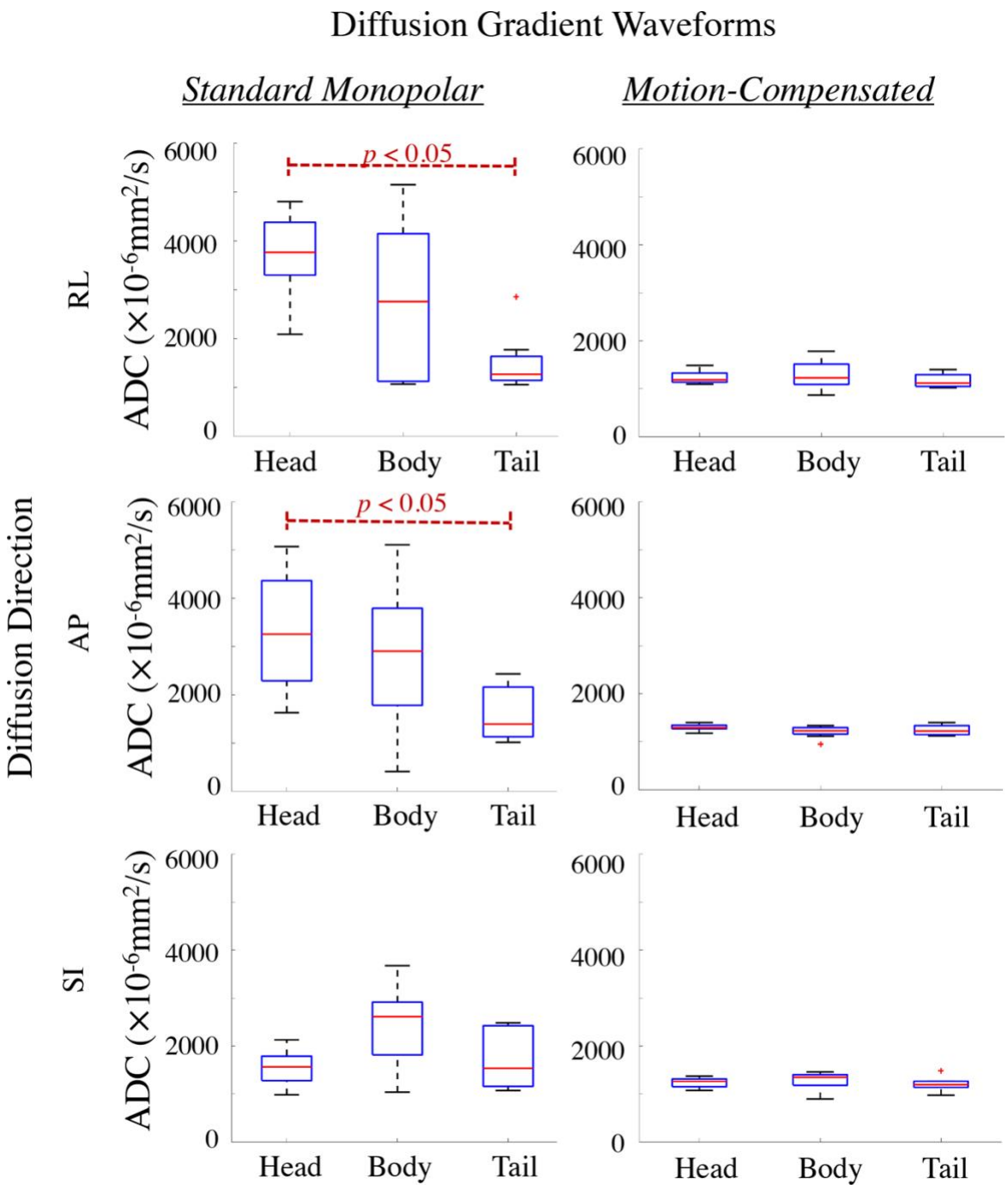

Figure 12. Boxplots of ADC measurements of eight volunteers derived from diffusion-weighted images acquired with b = 50 s/mm² and b = 500 s/mm² with standard monopolar and motion-compensated gradient waveforms in three diffusion directions in the breath-hold study. *Using a standard monopolar gradient waveform, the measured ADCs had a large variability among volunteers and were higher in pancreas head and body than in the tail. Using a motion-compensated gradient waveform, the measured ADCs had a much lower variability among volunteers and were comparable across the parts of the pancreas.*

3.3.3.1 Evaluating whole-pancreas respiratory-triggered DWI

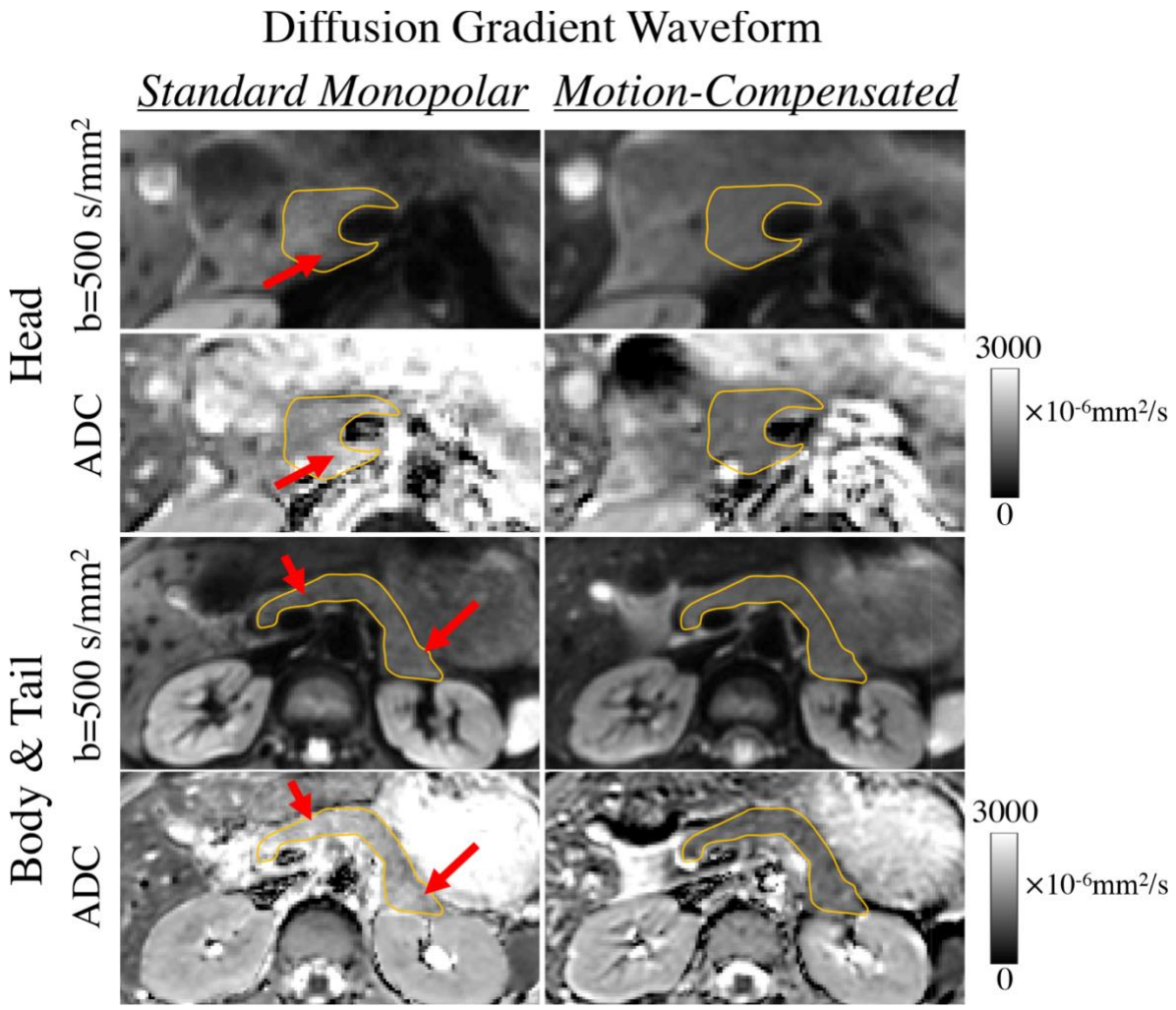

Figure 13 shows examples of DWI b = 500 s/mm^2 images and ADC maps acquired with respiratory-triggering using standard monopolar and motion-compensated DW waveforms. Standard DW waveforms led to localized regions of signal dropouts, resulting in heterogeneous ADC values across the three parts of the pancreas. The mean ADC values for the pancreatic head was 1756 ± 173 ×10^{-6} mm^2/s and the median (IQR) was 1739 (1638 to 1856) ×10^{-6} mm^2/s. For the pancreatic body: 1530 ± 338 ×10^{-6} mm^2/s and 1468 (1229 to 1938) ×10^{-6} mm^2/s. And for the pancreatic tail: 1388 ± 267 ×10^{-6} mm^2/s and 1264 (1187 to 1598) ×10^{-6} mm^2/s. Using a motion-compensated DW waveform, the measured ADCs were comparable across the parts of the

pancreas (head: 1277 ± 102 $\times 10^{-6}$ mm^2/s; body: 1204 ± 169 $\times 10^{-6}$ mm^2/s; tail: 1235 ± 178 $\times 10^{-6}$ mm^2/s). Boxplots of ADC measurements of eight volunteers for the two waveforms in respiratory-triggered study are shown in **Figure 14**. Using a standard monopolar DW waveform, the measured ADCs in the pancreatic head and body were significantly higher than in the tail ($p < .05$). Using motion-compensated DW waveforms, the measured ADCs had a lower variability among volunteers and were comparable in all three parts of pancreas ($p = .54$ between head and tail, $p = .69$ between body and tail, and $p = .19$ between head and body).

3.3.4 Effect of peristalsis

The effect of additional sources of motion artifacts (e.g. peristalsis) in breath-held, cardiac-triggered multi-repetition DWI was evaluated qualitatively. In the standard monopolar DW images, the location of signal dropout regions appears largely consistent across repetitions within the same breath-hold. However, residual variability across repetitions may be present, as indicated by the yellow arrows. DW images across multiple repetitions appeared similar when using motion-compensated waveforms.

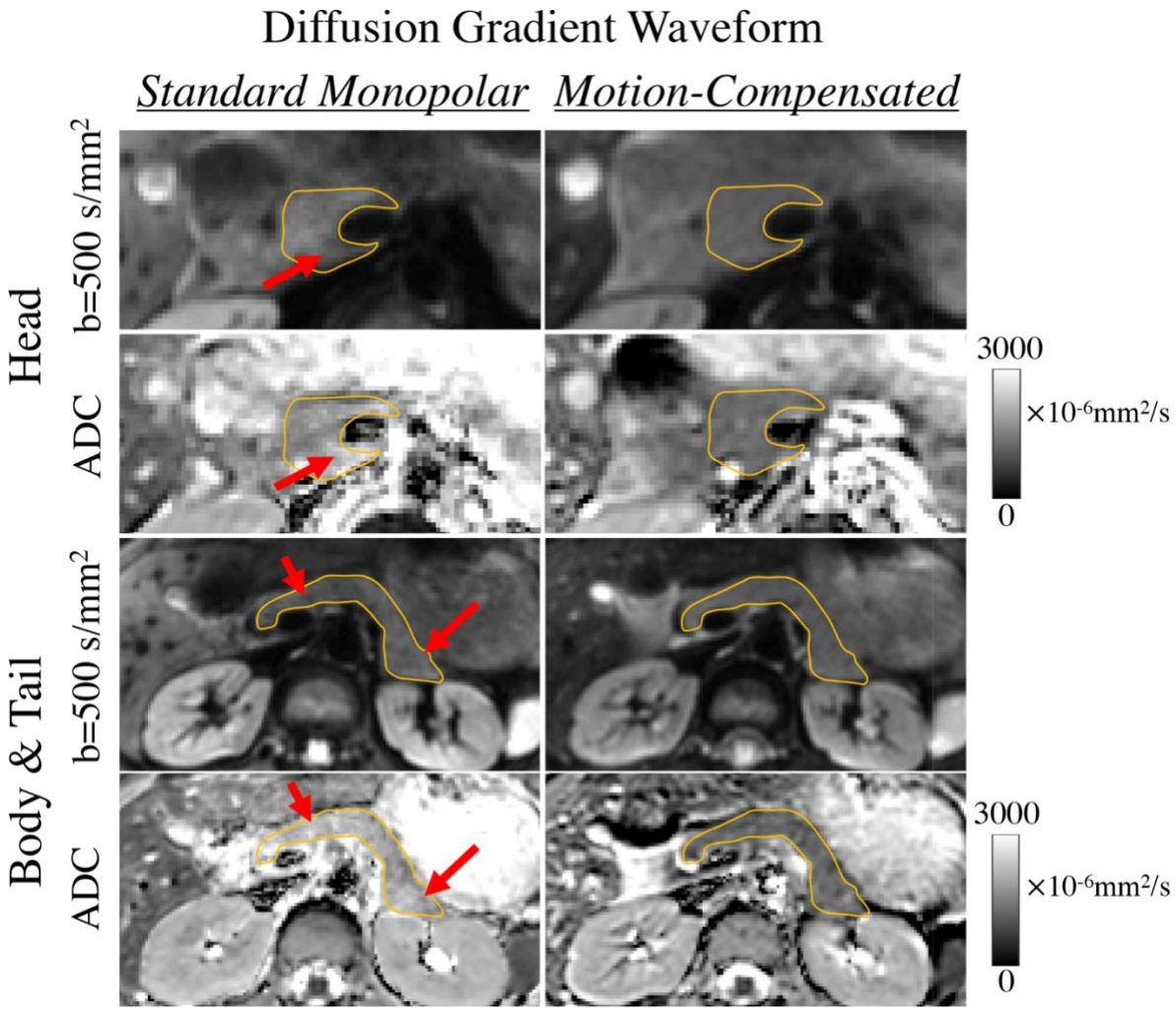

Figure 13. Examples of DWI b = 500 s/mm^2 and ADC maps of the whole pancreas acquired with respiratory-triggering using standard monopolar and motion-compensated DW waveforms. *Standard DW waveforms led to localized regions of signal dropouts, resulting in heterogeneous ADC values across the three parts of the pancreas. Green arrows indicate locations of artifactual signal dropouts. Since more repetitions and slices were acquired, the signal dropouts were blurred compared to the highly controlled single slice acquisitions shown earlier and the resulting elevated ADC values. Using a motion-compensated DW waveform, the measured ADCs were comparable across the parts of pancreas.*

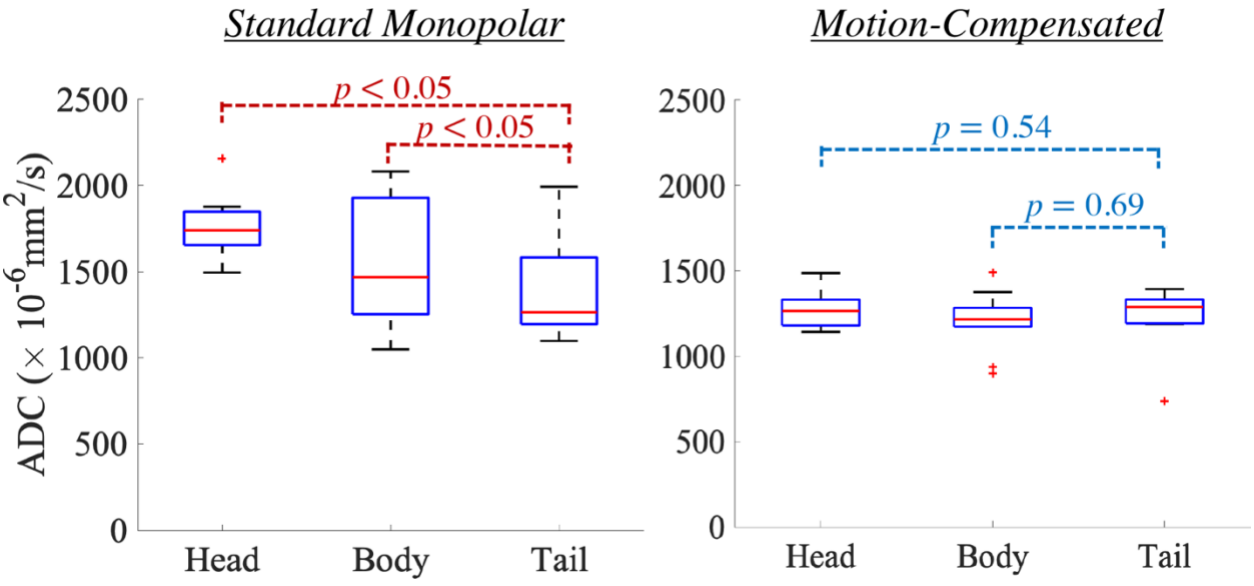

Figure 14. Boxplots of ADC measurements of ten volunteers for the two waveforms in the respiratory-triggered study. *Using a standard monopolar DW waveform, the measured ADCs in the pancreas head and body were significantly higher than in the tail. Using motion-compensated DW waveform, the measured ADCs had a lower variability among volunteers and were comparable in all three parts of pancreas.*

3.4 Discussion

Cardiovascular-related motion leads to artifacts and bias in conventional DWI of the pancreas. These artifacts and bias are mitigated through the use of recently proposed motion-robust DWI methods. Cardiovascular-related motion induces complex compressive motion of the pancreas, leading to signal dropouts in head, body, and tail, at various phases in the cardiac cycle, and in various diffusion directions. Motion-compensated diffusion gradient waveforms improved the DW signal reliability, resulting in more reproducible diffusion quantification.

These results may have important implications for research and clinical applications of pancreas DWI. As a result of artifacts in DW images, biased ADC values with a large variation across volunteers occurred in all cases. Importantly, these artifacts and bias are likely unavoidable by simply selecting a particular diffusion direction or trigger delay. A large location

and subject dependence on the occurrence of the artifacts was observed across different trigger delays. At the same trigger delay, signal void artifacts occurred at different slices for different subjects. Beyond the long scan times that would be needed for cardiac- and respiratory-triggered DWI of the pancreas, our proof of concept study suggests that there may not be an optimal cardiac trigger delay across slices and subjects. These results highlight the value of motion-compensated gradient waveforms to provide consistent ADC values across slices and subjects. Motion-robust DWI may reduce ADC bias and variability in the clinic, with the potential to enable more accurate lesion detection and diagnosis, as well as lesion characterization (e.g., for distinguishing benign versus malignant lesions) and treatment monitoring.

Cardiovascular-induced compressive motion is a major source of the signal dropouts observed in pancreas DWI. The phantom study suggested that pulsation or motion within blood vessels may induce pancreas deformation, and increased deformation led to increased severity of DWI artifacts and ADC bias. Further, in the highly controlled cardiac triggered *in vivo* experiments using monopolar DW gradients, individual repetitions were examined qualitatively. Importantly, for a BH acquisition with a fixed cardiac trigger delay (TD) time, the location of the artifacts appeared consistent across repetitions. Also, the location of artifacts appears different for different acquisitions performed at different TDs or different diffusion directions. Therefore, the effect is likely to be highly periodic with the cardiac cycle, which strongly suggests that the source is cardiovascular-related motion. Nevertheless, additional sources of motion (e.g., peristalsis) may contribute to the observed artifacts. Regardless of the specific source of motion, this study demonstrated the potential for improved ADC reproducibility with motion compensated gradients.

Using monopolar diffusion waveforms showed heterogeneity of ADC measurements from pancreatic head to tail (higher ADC in the head, and lower in the tail), which replicates the results from various previous studies(116, 120, 124–126). One previous study reported that ADC values in the pancreatic head were higher than in the tail, independently of gender, age and BMI(126). Schennagel et al. proposed the cause for the different ADC values in pancreatic head, neck, and tail to be due to the heterogeneity of the pancreatic tissue composition. However, our results suggest that these differences may be artifactual and due to cardiovascular-related motion effects. Importantly, in our study, this heterogeneity in ADC across different parts of pancreas disappeared when using motion-compensated gradient waveforms.

The motion artifact correction achieved by motion-compensated gradient waveforms in pancreas DWI bears resemblance to that in other organs. The effects of motion-compensated gradient waveforms to mitigate motion-induced ADC biases have been demonstrated in the liver MRI literature(26–28). In previous studies, monopolar-based ADC showed significant bias in the left lobe relative to the right lobe due to its sensitivity to motion, while DWI with motion-compensated waveforms showed no significant ADC bias in the left lobe relative to the right lobe, demonstrating robustness to cardiac-induced motion(26–28).

The observed ADC bias with monopolar DW waveforms was larger in the highly-controlled cardiac-triggered, breath-held acquisitions than in the respiratory triggered study. This is likely due to the high consistency of signal dropouts across repetitions in cardiac-triggered, breath-held acquisitions. In contrast, in the respiratory-triggered acquisitions without cardiac triggering, many repetitions are acquired at different cardiac phases, which partially averages out these signal dropouts, and leads to less pronounced (although still substantial) ADC bias. Another possible difference is that cardiovascular-related compressive motion may actually be

different during a breath-hold compared to during free breathing. Before holding their breath, volunteers were coached to take two rounds of deep inspiration and expiration, as practiced in the clinic. Previous studies show that the diameters of portal, splenic, and superior mesenteric veins (major veins by the pancreas) change significantly between deep inspiration and expiration(131), which may have resulted in stronger venous dilation and contraction, and increased compressive tissue motion. However, even in respiratory-triggered acquisitions the ADC bias and variability are still large and likely to interfere with quantitative applications of ADC, such as lesion characterization. Importantly, this bias and variability are reduced substantially with motion-compensated methods.

This study had several limitations. Since our study only included healthy volunteers, further studies in patients are needed. Our results suggest that motion compensation may improve the precision (e.g. test-retest repeatability) of ADC measurements in the pancreas(132). However, assessment of repeatability was not directly performed in this work. Further studies in volunteers and patients may also be needed to establish a clear separation of the effects of tissue composition and motion artifacts. With reduced motion-induced artifacts as enabled by motion-robust DWI methods, tissue heterogeneity may be more accurately measured in subsequent studies. The motion phantom used in this work does not precisely replicate the complex physiological motion of the pancreas. However, this phantom enables the evaluation of diffusion-weighted imaging under highly-controlled pulsatile motion. Remaining challenges in pancreas DWI are not addressed in this study, including susceptibility-related distortions which may influence image quality, as well as non-Gaussian diffusion which may require more advanced modeling of DW signals(133–136). Nevertheless, the proposed motion-robust methods are compatible with other advances in DWI, including low-distortion techniques(129, 137, 138),

and the improved signal reliability provided by motion-compensated DW waveforms may also enable improved performance of advanced diffusion modeling methods. Remaining systematic differences may exist between the ADC values derived from monopolar and motion-compensated waveforms, likely due to multiple effects including IVIM (micro-perfusion)(54, 55, 139), echo time, and diffusion time. For instance, motion-compensated diffusion acquisitions may lead to residual IVIM-induced dependence of pancreas ADC measurements on the choice of b values. This dependence of ADC on the choice of b values is expected to be different for motion-compensated compared to monopolar-based ADC measurements. Thorough analysis of these multiple potential confounding effects is beyond the scope of this work. One future consideration for deploying this technique across scanners is increased minimum TR due to issues including gradient duty cycle and heating limitations, which may lead to longer overall scan time (e.g. when the number of slices required to cover the whole liver is large). Importantly, compared to monopolar diffusion waveforms, motion-compensated waveforms enable improved ADC mapping in the pancreas by reducing motion-related bias and variability.

3.5 Conclusion

Cardiovascular-related compressive motion introduces substantial artifacts and ADC bias in pancreas DWI, which can be addressed by motion-compensated diffusion gradient waveforms. These results may have important implications both for understanding the current literature on DWI of the pancreas and for the design of improved DWI techniques for clinical and research applications.

Chapter 4 Development of Optimized Methods for Motion-Robust, Free-Breathing DWI in the liver

4.1 Introduction

Recent works have shown that motion-robust M1-optimized diffusion gradient waveforms (MODI) can address cardiac-induced artifacts while reducing blood signal(26–28). Nevertheless, motion-robust DWI typically requires longer TEs, which leads to a loss of SNR. Multi-repetition acquisitions with respiratory triggering (RT) are able to enhance SNR and co-localization(122). However, RT lengthens the repetition time (TR) and leads to unpredictable scan time due to variability in patients' breathing patterns(121). To address these challenges, I propose to develop a novel free-breathing (FB) DWI technique that combines motion-robust diffusion waveforms(27, 28) to address the effects of cardiovascular pulsation with motion-corrected averaging for respiratory motion-correction using a non-local means algorithm (NLM). I propose to validate this technique in healthy volunteers and patients with known or suspected liver metastases.

4.2 Methods

The non-local means algorithm is based on a non-local averaging of all pixel in the image, which was first proposed for the denoising of a single image(140). Our research group showed non-local means can also be used to align anatomical structures that move with respiratory motion(29). The NLM motion-corrected averaging algorithm works similar to the NLM denoising algorithm, with an additional dimension across image repetitions.

After IRB approval and informed written consent, ten healthy volunteers and eight patients with known or suspected liver metastases were recruited and scanned at 3T (GE Signa Premier) using flexible receive coils (AIR Technology, GE Healthcare, Waukesha, WI). The acquisition parameters are shown in **Table 5**.

	Healthy volunteers								Patients	
DWI gradient waveforms	MODI: optimized motion-compensated waveform				MONO: standard monopolar waveform				MODI: optimized motion-compensated waveform	
Acquisition modes	FB		RT		FB		RT		FB	
TR (ms)	4000		5000 – 10000*		4000		5000 – 10000*		3800--4000	
TE (ms)	68.5				45.7—46.1				68.5	
Scan time range (min)	9:30 ± 0:14		12:58 ± 2:52		9:31 ± 0:14		13:24 ± 2:27		7:20--7:51	
b values (s/mm^2)	100	500	100	500	100	500	100	500	50	500
Number of repetitions acquired per direction	12	32	6	14	12	32	6	14	6 / 12	14 / 24
Diffusion directions	Phase, frequency, and slice (AP, RL, SI)									
Field of view	36 cm x 36 cm									
In-plane resolution	2.8 mm x 2.8 mm									
Slice thickness	6 mm									
Receiver Bandwidth	250 kHz / pixel									
Parallel imaging factor	2									

*1-2 respiratory intervals depending on breathing pattern of the volunteer.

Table 5. Imaging parameters used for the healthy volunteer and patient studies. *In healthy volunteers, a motion-robust M1-optimized diffusion gradient waveform (MODI) and a standard monopolar waveform (MONO) were used to acquire DW images with multiple b values in three encoding directions with different numbers of averages in free-breathing and RT acquisition modes. The scan times and TR with FB for both waveforms were stable among all volunteers with minor variations due to selecting different numbers of slices to cover the entire liver, while the scan time and TR with RT was longer on average and varied a lot among volunteers. In patients, motion-robust M1-optimized diffusion gradient waveform (MODI) was used to acquire DW images with two b values in three encoding directions, during free-breathing. Different numbers of averages were acquired for different subjects due to limitations of available clinical scan time.*

4.2.1 Health volunteer study

Motion-robust M1-optimized (MODI) diffusion gradient waveform and standard Stejskal-Tanner monopolar (MONO) waveforms were used to acquire DWI of the liver. For each gradient waveform, both FB and RT acquisitions were performed. For the FB acquisitions, an NLM-based algorithm (**Figure 15**) was used to address motion across repetitions and diffusion directions for each b-value.

An NLM-based algorithm (**Figure 15**) was used to address motion across repetitions and diffusion directions for each slice and each b-value. Within NLM, a patch-based(141) reference selection step was used to account for non-rigid motion in the through-plane direction. For each

slice and b-value, a set of reference images was obtained by stitching together co-registered overlapping patches from all repetitions. Each reference patch was chose based on a similarity metric (mutual information) across repetitions and across b-values.

Three technical components were assessed: diffusion waveform (MODI vs. MONO); respiratory-motion mitigation (RT vs. FB); and signal averaging (direct averaging vs. NLM). For each acquisition and signal averaging method, DW images and corresponding ADC maps were generated. Performance comparisons included: ADC measurements in right and left liver lobes in MODI vs. MONO, SNR of averaged FB vs. RT images under comparable scan times, and motion-robustness and SNR of direct averaging (DA) vs. NLM. Additionally, assessment of respiratory-motion mitigation and signal averaging methods was performed retrospectively using fewer repetitions (50% and 20%), in order to assess the potential for faster acquisitions with the proposed approach. For each choice of technical components and number of repetitions, signal and noise levels of ADC maps were estimated by calculating means and standard deviations over co-localized ROIs.

4.2.2 Patient study

A T2-weighted fast spin echo and fat-saturated T1-weighted in- and out-of-phase acquisitions were obtained for anatomical reference. Motion-robust M1-optimized diffusion gradient waveforms (MODI) were used to acquire DWI (b=50, 500 s/mm^2) of the liver in FB without respiratory gating or triggering. The respiratory bellows signals from each FB acquisition were recorded to perform retrospective gating with 33% acceptance window, as an alternative reconstruction method for comparison with the proposed non-gated method.

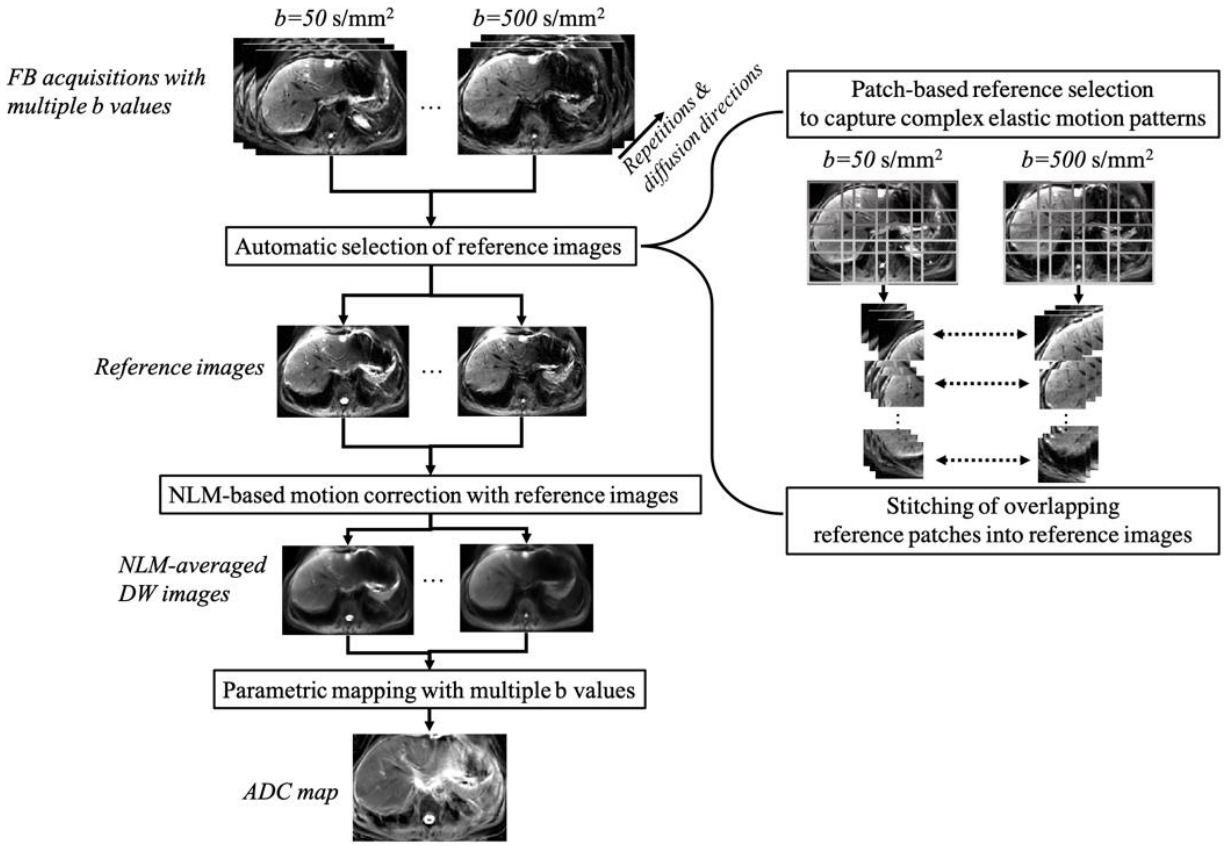

Figure 15. Workflow of NLM implementation for DWI for each slice and b-value for MODI waveform. *NLM addressed motion across repetitions and directions for each b-value. For each slice and b-value, a set of reference images was obtained by stitching together co-registered blocks from all repetitions. Each reference block was chose based on a similarity metric to the other repetitions and across b-values. NLM averaged the remaining repetitions using Gaussian-fitted weights in accordance with the local Euclidean distance to the reference images. ADC maps were calculated from the different b-values.*

4.3 Results

4.3.1 Healthy volunteer study

Diffusion waveform (MODI vs. MONO): ADC values are more homogeneous across left and right lobes on MODI than on MONO (**Figure 16**, **Figure 17**). While a significant difference between left and right lobes was observed in MONO for each acquisition mode and signal-averaging method (**Figure 18**. a), MODI provides consistent ADC values across liver (**Figure 18**. b).

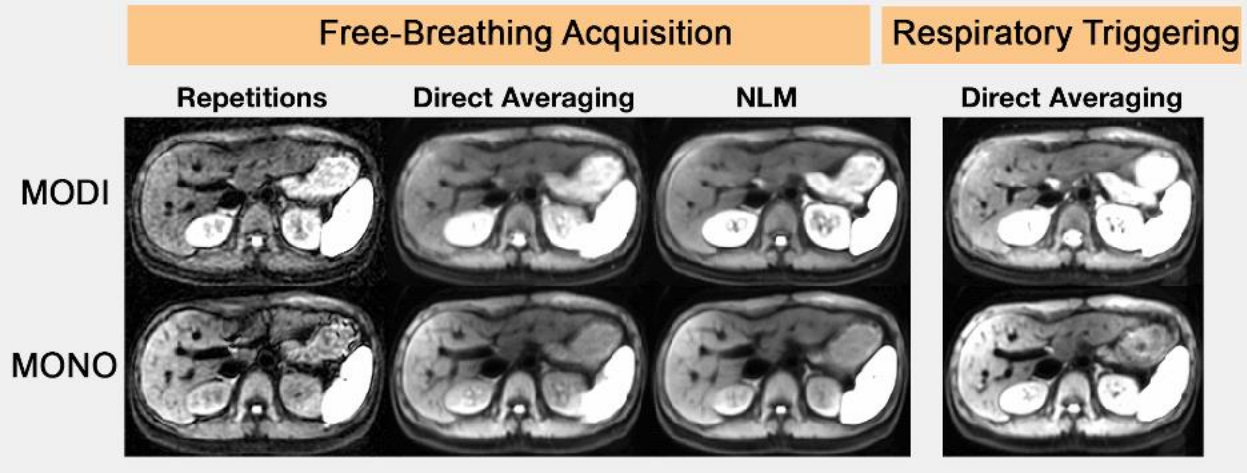

Figure 16. Compared to direct averaging, NLM reduced the mis-registration due to body motion, showed increased homogeneity in the liver, and higher spatial resolution overall. *MODI and MONO diffusion-weighted images using 100% repetitions of individual repetitions, post-processed with direct averaging (DA) and with NLM, and acquired in respiratory triggering mode for b=500 s/mm^2.*

Respiratory-motion mitigation (RT vs. FB): Scan times with FB for both waveforms were fixed across volunteers, while RT scan times were longer on average and varied substantially across volunteers. FB data reconstructed with NLM had similar signal levels but significantly lower noise levels compared to RT on MODI when 100% repetitions were used (**Figure 18**. c). As number of repetitions decreased, NLM tended to maintain lower noise levels than RT (**Figure 17**). FB acquisitions may enable higher SNR efficiency than RT.

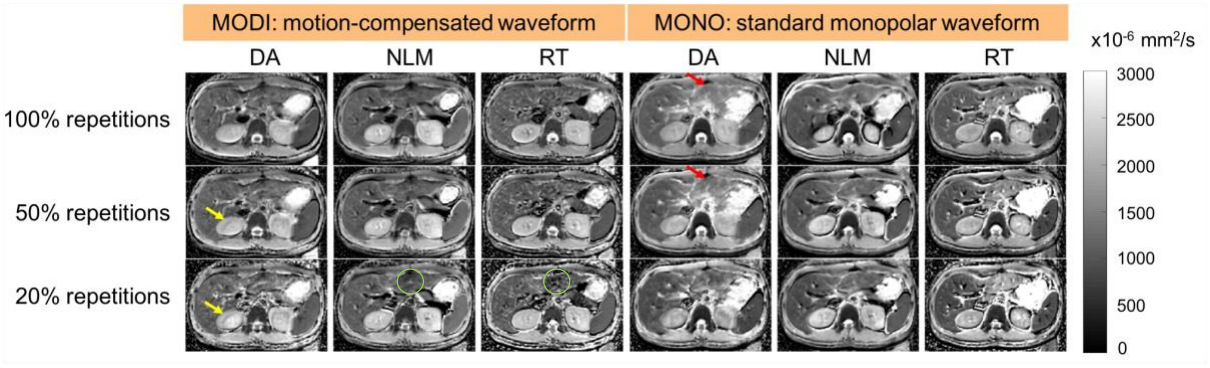

Figure 17. The ADC maps of MODI and MONO acquired in FB and RT modes and post-processed with DA and NLM algorithm. *In the absence of artifacts, ADC was expected to be similar between left and right lobes in healthy volunteers. Compared to DA, NLM reduced the mis-registration between b=100 s/mm^2 and b=500 s/mm^2 repetitions due to body motion (indicated by yellow arrows), showed increased homogeneity (indicated by red arrows) in the liver, and higher spatial resolution overall. Compared to RT, NLM showed higher SNR performance (circled in green).*

<u>*Signal averaging (DA vs. NLM):*</u> In both DWI and ADC maps (**Figure 16**, **Figure 17**), compared to DA, NLM reduced the mis-registration due to body motion and higher spatial resolution overall, yielding significantly higher image sharpness as measured by energy of Laplacian (**Figure 18**. d). NLM has similar SNR performance to DA (**Figure 18**. a - c).

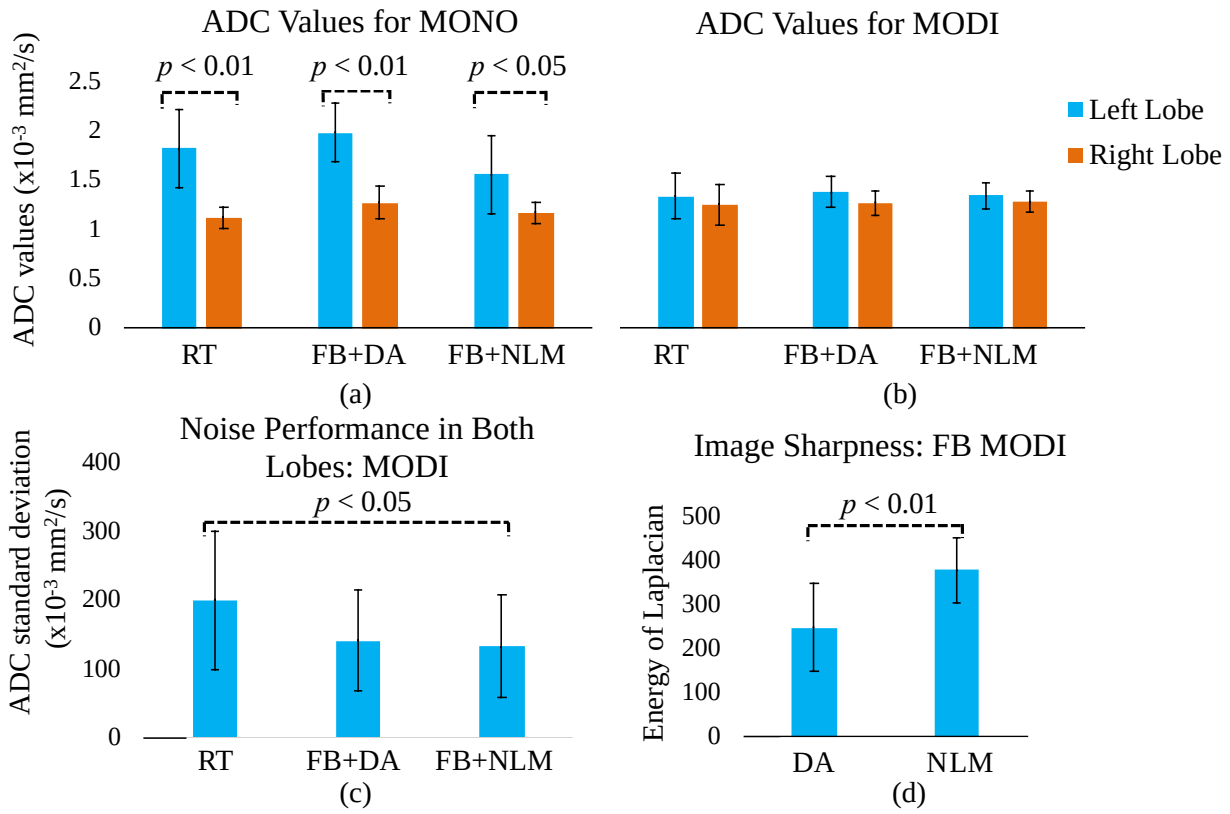

Figure 18. Bar plots of ADC values, ADC standard deviations, and image sharpness for monopolar (MONO) and motion-robust M1-optimized (MODI) diffusion gradient waveforms, using respiratory triggering (RT), and direct averaging (DA) and non-local mean (NLM) correction for free-breathing acquisitions (FB). *While a significant difference between left and right lobes was observed in MONO for each acquisition mode and signal-averaging method (a), MODI provides consistent ADC values across liver (b). FB data reconstructed with NLM had similar signal levels but significantly lower noise levels compared to RT on MODI. and NLM has a similar noise level to DA (c). NLM yields significantly higher image sharpness as measured by energy of Laplacian (d). NLM has similar SNR performance to DA (a-c).*

4.3.2 Patient study

Data were acquired and processed successfully for all 8 patients. Three representative examples are shown. DW images and ADC maps of a liver metastatic lesion from pancreatic cancer, processed with direct averaging, retrospective gating, and motion-corrected averaging (NLM) are shown in **Figure 19**. The lesion appeared to be extended in size and the boundaries appeared blurry in DW images and ADC maps processed with direct averaging and retrospective gating. With NLM, the shape and size of the lesion more closely match the co-localized T2-

weighted acquisition, and the boundaries appeared clearer in both DW images and ADC map. Retrospective gating demonstrated lower SNR and residual motion-related blurring and mis-registration.

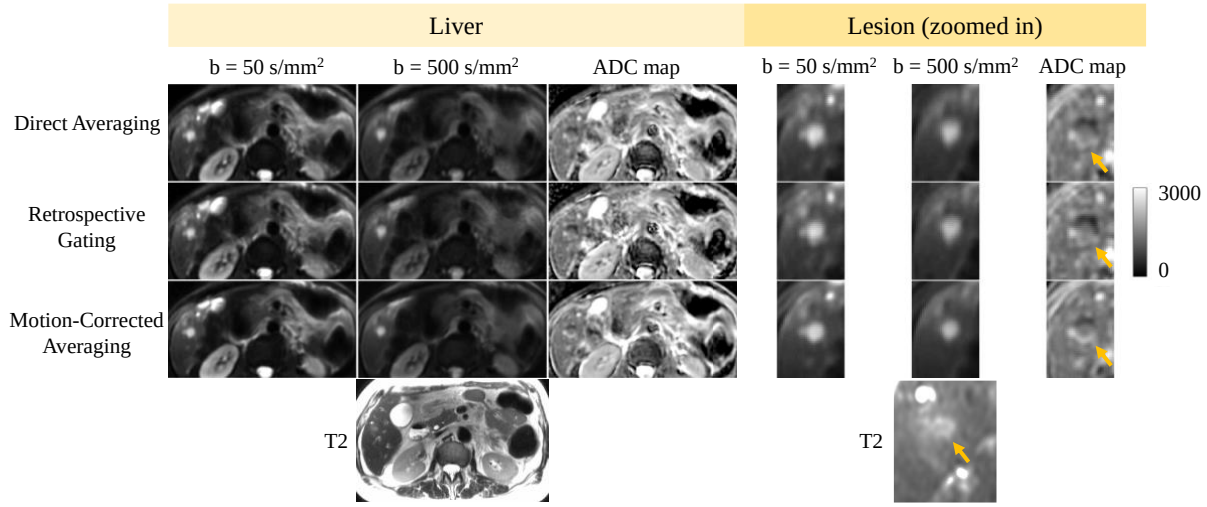

Figure 19. DW images and ADC maps of a liver metastatic lesion from pancreatic cancer, processed with direct averaging, retrospective gating, and motion-corrected averaging (NLM). *The lesion appeared extended in size and boundaries appeared blurry in DW images and ADC maps processed with direct averaging and retrospective gating, due to inadequate alignment of the lesion across repetitions and b values. And retrospective gating had lower SNR. With NLM, shape and size of the lesion showed improved correspondence to co-localized T2 reference, and boundaries appeared clearer in DWI and ADC map.*

Figure 20 shows DW images and ADC maps of multiple liver metastatic lesions from pancreatic cancer. The two adjacent lesions indicated by yellow arrows appeared to have blurry boundaries in DW images and ADC maps processed with direct averaging and retrospective gating. With NLM, the boundaries were clearly delineated and showed improved correspondence with the co-localized T2-weighted slice. However, despite the improved performance, NLM was unable to align every lesion correctly (orange arrows).

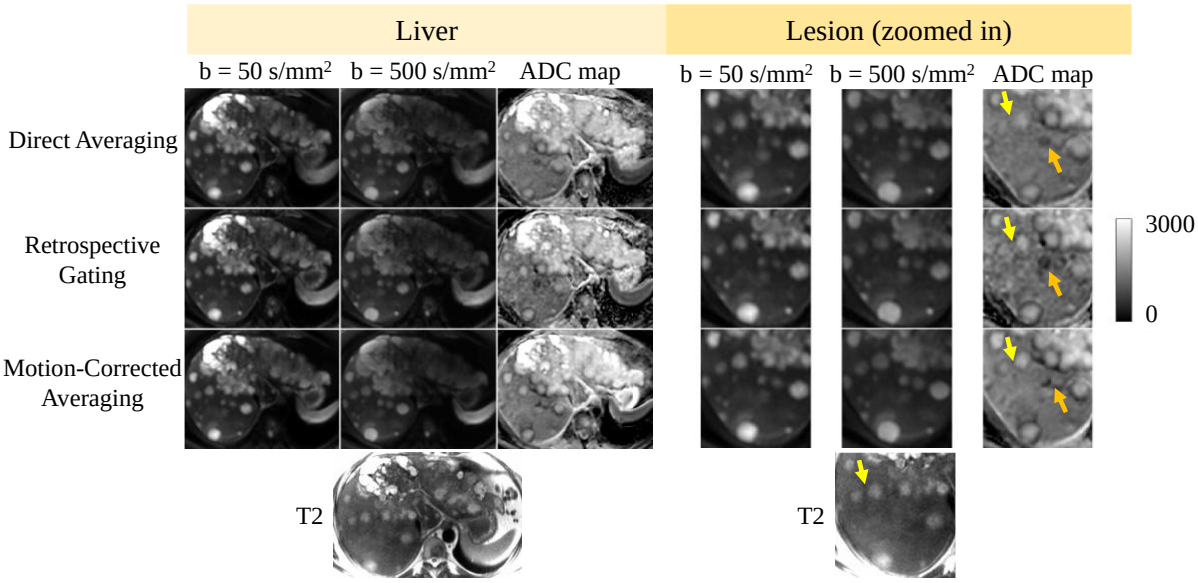

Figure 20. DW images and ADC maps of multiple liver metastatic lesions from pancreatic cancer, processed with direct averaging, retrospective gating, and motion-corrected averaging (NLM). *The two lesions pointed by yellow arrows appeared to have blurry boundaries in DW images and ADC maps processed with direct averaging and retrospective gating. With NLM, the boundaries were clearly delineated and better confirmed with its counterpart in the co-localized T2 slice. But in such a challenging case, NLM was unable to align every lesion correctly as a black crescent of mis-registration is pointed out by the orange arrows.*

DW images and ADC maps of an ablation site from previous treatment of hepatocellular carcinoma are shown in **Figure 21**. The lesion appeared to be extended in size and the boundaries appeared blurred in DW images and ADC maps processed with direct averaging and retrospective gating. With NLM, the shape and size of the lesion demonstrate improved correspondence with the co-localized T2-weighted slice, and the boundaries appeared clearer in both DW images and ADC map. Again, retrospective gating had lower SNR and residual motion-related blurring and mis-registration.

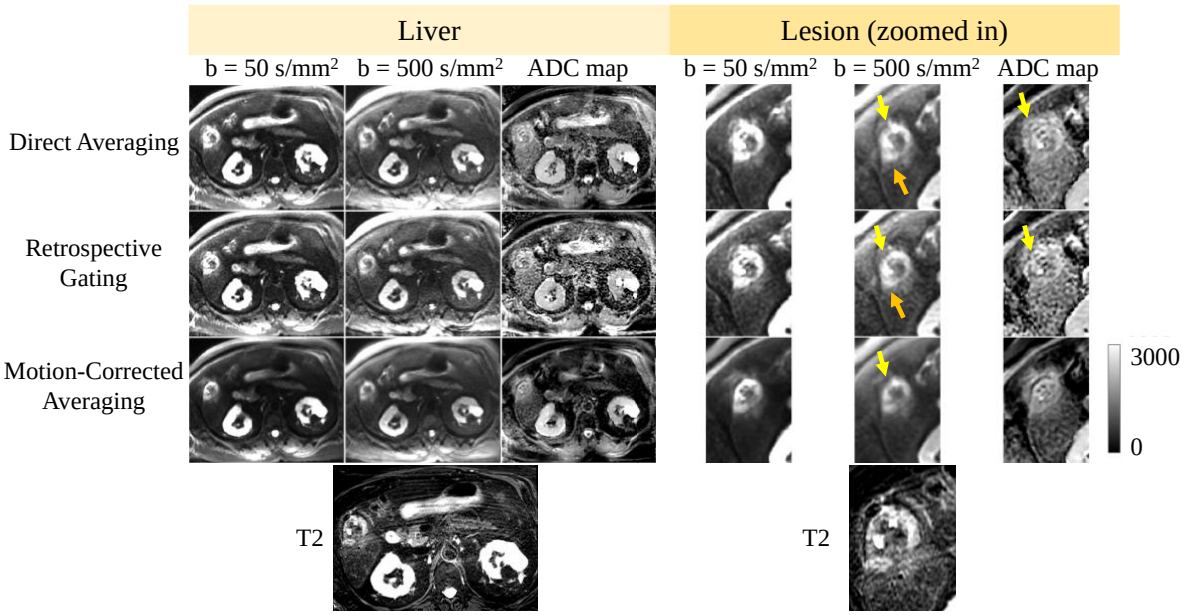

Figure 21. DW images and ADC maps of an ablation site for hepatocellular carcinoma, processed with direct averaging, retrospective gating, and motion-corrected averaging (NLM)*. The lesion appeared extended in size and had blurry boundaries in DW images and ADC maps processed with direct averaging and retrospective gating, due to inadequate alignment of the lesion across repetitions and b values. Retrospective gating had lower SNR. With NLM, the shape and size of the lesion showed better correspondence to co-localized T2 reference, and the boundaries appeared clearer in DW images and ADC map.*

4.4 Discussion

The proposed technique using motion-robust gradient waveforms (MODI) with FB acquisitions and motion-corrected averaging may enable abdominal DWI without motion artifacts and with high SNR. Compared to standard RT acquisitions, the proposed DWI technique provides higher SNR and predictable scan times even in the presence of irregular breathing patterns (which lead to scan variability in RT imaging). The proposed NLM algorithm has the potential to correct for motion across repetitions, diffusion directions, and b values. The patient study has demonstrated the feasibility of the proposed FB DWI technique in patients with

liver lesions. This technique combines motion-robust gradient waveforms (MODI) with FB acquisitions and motion-corrected averaging in order to enable abdominal DWI without motion artifacts and with high SNR. The proposed NLM approach has the potential to better align lesions within each slice, each b-value, and across b-values. The more accurate visualization of the shape, size, and boundaries of liver lesions in both DW images and ADC maps using NLM may have important implications in the clinic and in further clinical research.

This study has several limitations. Further optimization and characterization of the proposed technique are desirable. Indeed, NLM includes a number of tunable parameters that may be optimized, depending on the degree of respiratory motion and underlying SNR. And the patch-based reference selection step in NLM can be improved for patients with different lesion sizes and levels of DWI signal. Additionally, all lesions analyzed in this work were located in the right liver lobe; lesions in the left liver lobe need to be studied to test whether MODI can address the signal loss due to cardiac-related motion. Validation of the technique in a larger patient cohort is needed in future work. Future work includes the implementation of MODI waveform generation on the scanner and the optimization of the post-processing methods to adapt to patients with focal lesions. One consideration for a wider adoption of the proposed workflow is the speed of NLM reconstruction through the current MATLAB implementation. An alternative approach is to run the program in a remote server with higher computing power. Although NLM has shown promise to enable motion-robust FB acquisitions of liver DWI, lack of robustness due to the need for parameter tuning has manifested in the occasional mis-alignment of focal liver lesions. Deep learning (DL) methods have seen rapid adoption in MRI imaging, thanks to their ability to learn features from input images without being explicitly programmed(142). Future work can apply deep learning-based image registration and deblurring methods to align DWI

repetitions. In addition, as respiration-induced liver motion is different in the left-right (LR), anterior-posterior (AP), and superior-inferior (SI) orientations(143–147), image registration in the three orientations presents varying degrees of challenge. For slices acquired in the axial view, respiration-induced motion is predominantly through-plane, complicating the image registration process in 2D, while in the coronal and sagittal views, the respiration-induced motion is mostly in-plane, making it an easier 2D image registration problem. Therefore, joint optimization of acquisition and post-processing methods for motion robust FB DWI, including optimizing the acquisition slice orientation along with the post-processing methods, remains a promising direction for future research.

Nevertheless, the proposed motion-corrected FB DWI method shows the potential to improve the workflow (i.e., predictable and shortened scan times) and image quality (i.e., motion robustness and improved SNR) compared to current methods for abdominal DWI.

Chapter 5 Summary and Future Works

5.1 Automated MR image prescription of the liver using deep learning

5.1.1 Summary

Chapter 2 demonstrates that an AI-based automated liver prescription method developed in this work has shown promising performance across patient populations, pathologies, and clinically relevant acquisition settings, well within inter-radiologist reproducibility. The proposed method enables liver image prescription in any orthogonal orientation. Further, this study demonstrated the successful prospective implementation of the method on a clinical MR system. This method has the potential to improve clinical workflow and standardization for MRI of the liver.

5.1.2 Ongoing and future works

Training and evaluation of the proposed method using multi-center and multi-vendor data with a wider variety of patient datasets is ongoing. From preliminary results, the proposed AI-based automated liver prescription methods have shown promising multi-center, multi-vendor performance. Without retraining, the single network had been trained on localizers from the University of Wisconsin Hospitals and Clinics (UW) as described in Chapter 2, and was tested in localizers acquired on scanners by different vendors at three different sites. **Figure 22** a-c show examples of AI-based axial prescription on multi-center, multi-vendor data without retraining. **Figure 23** a-c show the boxplots of mismatches between AI-based axial prescription and manual labeling on multi-center, multi-vendor data without retraining, as tested in 200 patients from each vendor / site. The AI method performed well in spin echo localizers acquired on GE scanners at UW and Philips scanners (Philips Medical Systems, Amsterdam, Netherlands) at the University of Texas Southwestern Medical Center (UTSW). But the AI method showed lower

performance in gradient echo localizers acquired on Siemens scanners (Siemens Healthineers, Erlangen, Germany) at Duke University Medical Center (Duke). The overlaps between AI-based axial prescription and manual labeling without retraining were 97.6±6.5% for GE scanners at UW, 96.2±7.7% for Philips scanners at UTSW, and 89.7±25.3% for Siemens scanners at Duke. The result was expected as the model had been trained on mostly spin echo localizers acquired on GE scanners at UW.

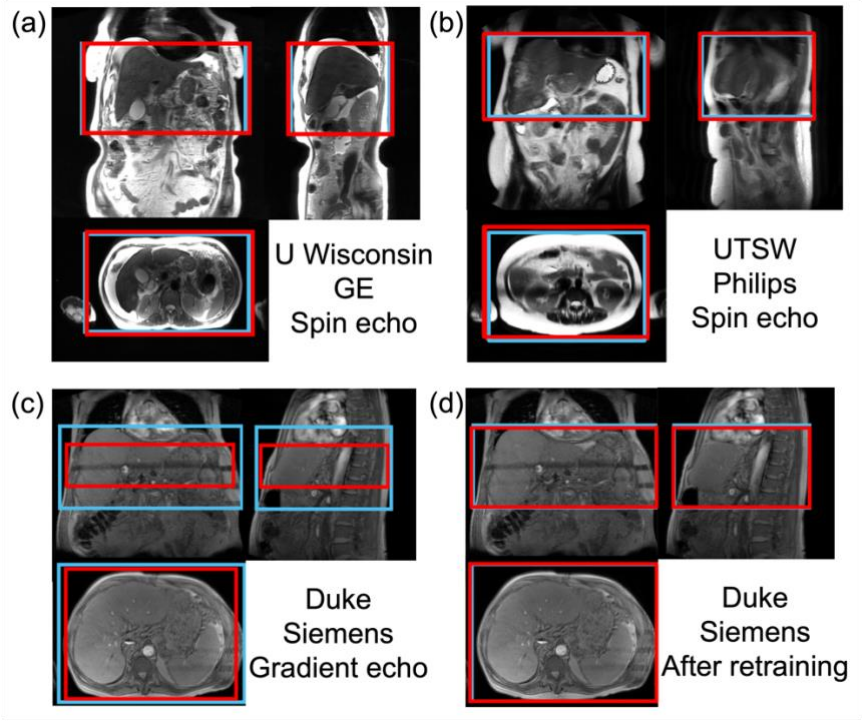

Figure 22. Examples of AI-based axial prescription on multi-center, multi-vendor data. *Without retraining, the single network was trained on UW data and tested in different vendors and sites. The AI method performed well in spin echo localizers acquired on GE scanners at UW and Philips scanners at UTSW. Without retraining, the AI method showed lower performance in gradient echo localizers acquired on Siemens scanners at Duke. However, after retraining, the method performed well on this Duke GRE dataset. (blue lines: manual prescription; red lines: AI prescription). Duke University data are courtesy of Dr. Mustafa Bashir. UT Southwestern data are courtesy of Dr. Takeshi Yokoo.*

The model was retrained with an additional 500 gradient echo cases from Duke, along with 500 spin echo cases from UW, and tested in the same 200 patients from each vendor / site

as above. The overlaps between AI-based axial prescription and manual labeling with retraining were 97.4±3.9% for GE scanners at UW, 96.3±7.4% for Philips scanners at UTSW, and 95.6±6.2% for Siemens scanners at Duke. the AI method performed substantially better in gradient echo localizers acquired on Siemens scanners at Duke. Across all the three vendors and sites, the AI method performed well, with the overlaps between AI and manual labeling all larger than 95%. Duke and UTSW prioritize fast acquisitions and use fewer images per plane for the localizers. But from the preliminary results, the proposed AI-based automated liver prescription methods have shown robustness to these variations in localizer acquisition settings and across the vendors and sites tested. Further optimization of the retraining process with multi-center, multi-vendor data to gain better generalizability across other sites and other patient populations remains future work.

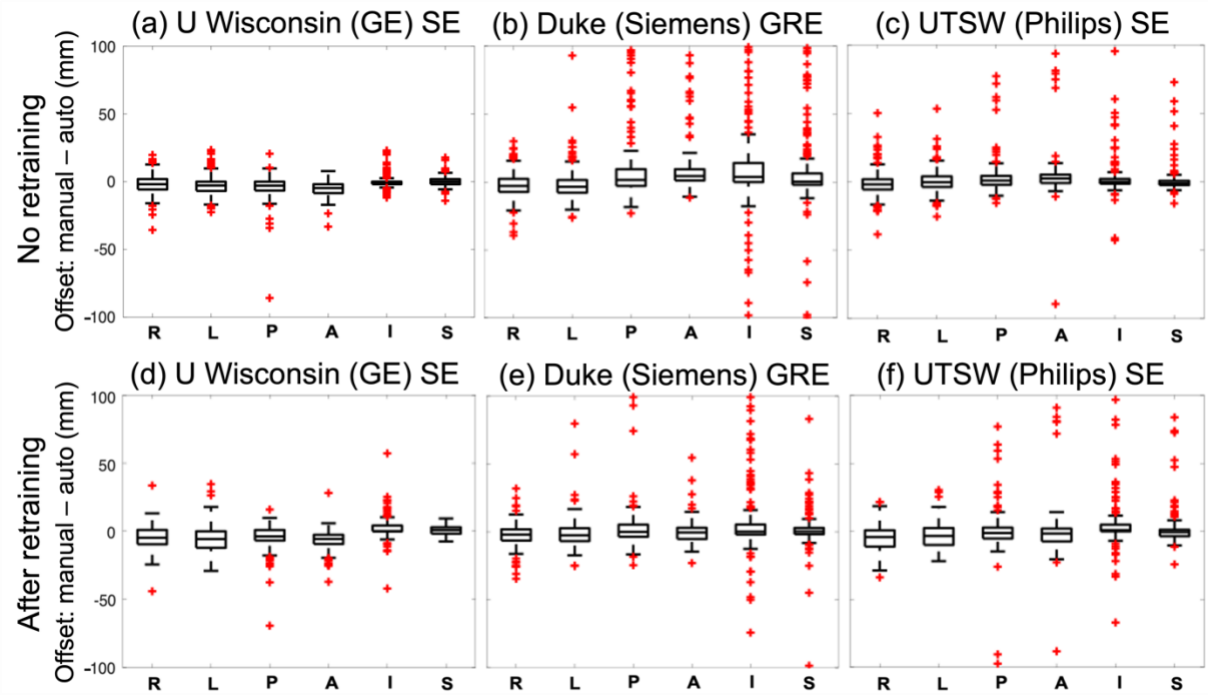

Figure 23. Testing results of AI-based axial prescription with and without retraining on 200 patients from each vendor / site*. Without retraining, the AI method performed well in spin echo localizers acquired on GE scanners at UW (a) and Philips scanners at UTSW (c). However, the AI method showed lower performance in gradient echo localizers acquired on Siemens scanners at Duke (b). This is expected as the*

model was trained on mostly spin echo localizers acquired on GE scanners at UW. After retraining the model with an additional 500 gradient echo cases from Duke, along with 500 spin echo cases from UW, the AI method performed better in gradient echo localizers acquired on Siemens scanners at Duke (e). Across all the three vendors and sites, the AI method performed well, with the overlaps between AI and manual labeling all larger than 95% (d-f).

After scanner implementation was in place, we developed a prototype of an automated pipeline towards the single button push liver fat/iron exams. An example on a healthy volunteer is shown in **Figure 24**. After three-plane localizers were acquired with free breathing, axial prescription was generated automatically within 3s for a chemical shift encoding sequence. This one-minute sequence is also free breathing and produced fat fraction and R2* maps, from which a report of the liver fat/iron content was generated automatically. Notably, although the AI model predicted a tight field-of-view (FOV), with the current vendor implementation on the scanner, the size of the in-plane FOV was fixed to preserve SNR and prevent aliasing. The current vendor implementation requires multiple clicks, but the example demonstrates the essential components to enable automated single button push scanning. Evaluation of this pipeline in patients is ongoing.

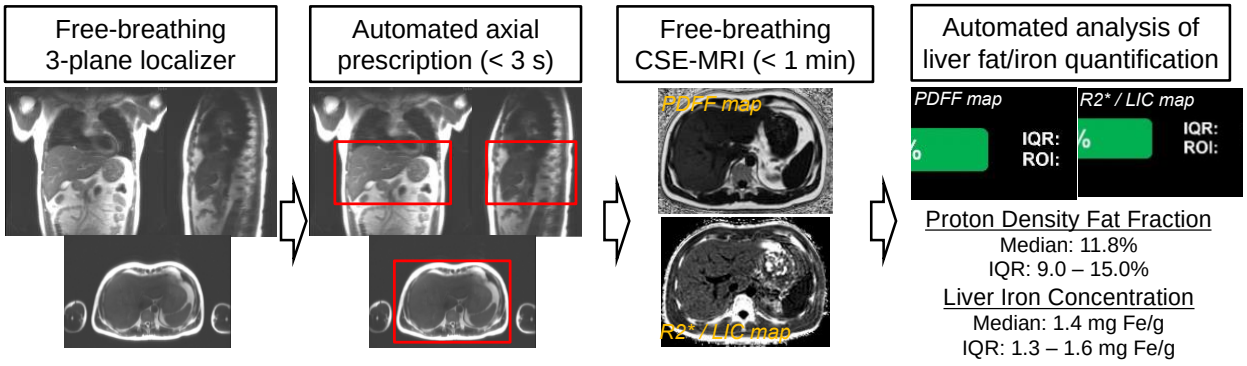

Figure 24. Prototype of an automated pipeline towards the single button push liver fat/iron exams on a healthy volunteer. *After three-plane localizers were acquired with free breathing, axial prescription was generated automatically within 3s for a chemical shift encoding sequence. This one-minute sequence is also free breathing and produced fat fraction and R2* maps, from which a report of the liver fat/iron content was generated automatically. Evaluation of this pipeline in patients is ongoing.*

Beyond applications in clinical fat/iron exams, a natural extended application of the proposed AI-based automated liver prescription is for MR elastography (MRE). MRE is a non-invasive imaging method for evaluating liver fibrosis. From localizers or coronal T2-weighted images, 4 axial image slices featuring the widest transverse dimension of the liver are manually prescribed. Manual image prescription for MRE by technologists is time-consuming and prone to error and variability. Automated MRE prescription based on an extension of the proposed method and other deep learning (DL)-based methods is being investigated in our group.

In addition, more cases with severe dielectric shading and iron overload from other vendors can be collected for training and testing to broaden the applicability of the algorithm. To improve the AI performance in such cases, methods like data augmentation and including more similar cases in the training dataset should be considered. In this study, simple definitions of liver coverage for 3D prescription in axial, coronal, and sagittal orientations were used for illustration. Additional coverage considerations in each orientation can easily be included subsequently. Finally, in this study experienced radiologists (rather than technologists) performed the labeling to train and demonstrate the performance of AI using the best possible manual labeling as the reference. In clinical practice, technologists typically prescribe the field of view for a given patient exam. Future studies aimed at measuring and comparing the inter-reader variability of technologists with AI performance are needed. A previous study showed that a commercial platform (Day optimizing throughput [Dot] engine, Siemens Healthineers, Forchheim, Germany) for automated image prescription contributed significant time savings (2-5 minutes) for whole-body free-breathing exams(86–89)(86–89). The effect of the proposed automated liver prescription approach on potential time savings needs to be further examined in future work. Value chain analysis from study acquisition to delivery of actionable information to

clinicians and patients may be conducted to determine whether automated prescription improves patient care and workflow efficiency in Radiology departments(132).

5.2 Towards motion-robust DW-MRI of the abdomen

5.2.1 Summary

Chapter 3 demonstrates that cardiovascular-related compressive motion introduces substantial artifacts and ADC bias in pancreas DWI, which can be addressed by motion-compensated diffusion gradient waveforms. Compared to monopolar diffusion waveforms, motion-compensated waveforms enable improved ADC mapping in the pancreas by reducing motion-related bias and variability. Importantly, previous works had shown that quantitative measures of diffusion such as the ADC varied along the pancreas from the head to the tail, and attributed these variations in ADC to actual differences in the pancreatic tissue. However, our results suggest that these differences may be artifactual and due to cardiovascular-related motion effects. Importantly, in our study, this heterogeneity in ADC across different parts of pancreas disappeared when using motion-compensated gradient waveforms. Crucially, the results also exemplify the importance of correcting for all relevant confounding factors in the development of quantitative MRI methods.

Chapter 4 demonstrates that using optimized gradient waveforms, non-gated free-breathing acquisitions, and motion-corrected averaging techniques, high-SNR and motion-robust DWI of the liver may be achieved. The patient study has demonstrated the feasibility of the proposed FB DWI technique in patients with liver lesions. This technique combines motion-robust gradient waveforms (MODI) with FB acquisitions and motion-corrected averaging in order to enable abdominal DWI without motion artifacts and with high SNR. The proposed NLM approach has the potential to better align lesions within each slice, each b-value, and across b-

values. The more accurate visualization of the shape, size, and boundaries of liver lesions in both DW images and ADC maps using NLM may have important implications in the clinic and in further clinical research. In summary, the proposed motion-corrected FB DWI method shows the potential to improve image quality (i.e., motion robustness and improved SNR) compared to current methods for abdominal DWI.

5.2.2 Ongoing and future works

Our results and previous works by our group suggest that motion compensation may improve the precision (e.g. test-retest repeatability) of ADC measurements of the abdomen (in the pancreas and liver)(114). Systematic assessment of repeatability and reproducibility in healthy volunteers and patients is ongoing. Preliminary results demonstrate substantially improved test-retest repeatability of ADC in the liver and pancreas when performed using motion-robust methods developed by our group(133). Ongoing work at our group evaluates the reproducibility of M1-optimized liver DWI across field strengths (1.5T and 3T) and gradient performances. In 8 healthy human subjects scanned on 3 separate MR systems with different field strengths and gradient performances, ADC estimation with M1-optimized diffusion waveforms achieved smaller coefficients of variation and reproducibility coefficients across MR systems in comparison to conventional monopolar DWI(134). This demonstrates the potential of M1-optimzed waveform designs to improve the reproducibility of diffusion quantitative parameters, which may emerge as reliable imaging biomarkers in the abdomen with further validations.

Further studies in volunteers and patients may also be needed to establish a clear separation of the effects of tissue composition and motion artifacts. With reduced motion-

induced artifacts as enabled by motion-robust DWI methods, tissue heterogeneity may be more accurately measured in subsequent studies.

Another ongoing work evaluates the feasibility and reproducibility of liver diffusion-weighted (DW) MRI using cardiac-motion-robust, blood-suppressed, reduced-distortion techniques(53). DW-MRI data were acquired at 3T in an anatomically accurate liver phantom including controlled pulsatile motion, in eight healthy volunteers and four patients with known or suspected liver metastases. Standard monopolar and motion-robust (M1-nulled, and M1-optimized) DW gradient waveforms were each acquired with single-shot echo-planar imaging (ssEPI) and multishot EPI (msEPI). In the motion phantom, ADC mean and SD in motion-affected volumes substantially increased with increasing motion for monopolar waveforms (**Table 6**). ADC remained stable in the presence of increasing motion when using motion-robust waveforms (**Table 6**). M1-optimized waveforms suppressed slow flow signal present with M1-nulled waveforms (**Figure 25**). In phantom and healthy volunteer studies, motion-robust acquisitions with msEPI showed significantly reduced image distortion ($p<0.001$) compared to ssEPI. Patient scans showed reduction of wormhole artifacts when combining M1-optimized waveforms with msEPI (**Figure 27**).

The diffusion-weighted images and ADC maps in the quantitative motion phantom in **Figure 25** demonstrate the robustness of the optimized motion-robust waveforms to compressive motion, suppression of perfusion (blood-mimicking) signals by M1-optimization, and the synergy between M1-optimized gradient waveform designs and multishot echo-planar imaging (msEPI) with increasing degrees of compressive tissue motion. Severe motion-induced signal dropouts (blue arrows) and ADC bias appear in monopolar images and ADC maps. Both M1-nulled and M1-optimized methods avoid the signal dropouts and produce consistent ADC

measurements throughout the liver model. With slow flow motion (roughly mimicking perfusion), residual bright signal from moving fluid remains in low-b-value images acquired with M1-nulled waveforms, resulting in biased ADC values in the tubing area (green circles). The perfusion signal is suppressed in low-b-value images acquired with M1-optimized waveforms (green arrows). ssEPI images suffer from severe image distortions (yellow contours and yellow arrows). msEPI reduces this image distortion. However, msEPI without motion-robust gradients shows wormhole artifacts in high-b-value images and biased ADC values (red arrows). M1-optimized-msEPI generates stable ADC measurements while maintaining low image distortion (red contours).

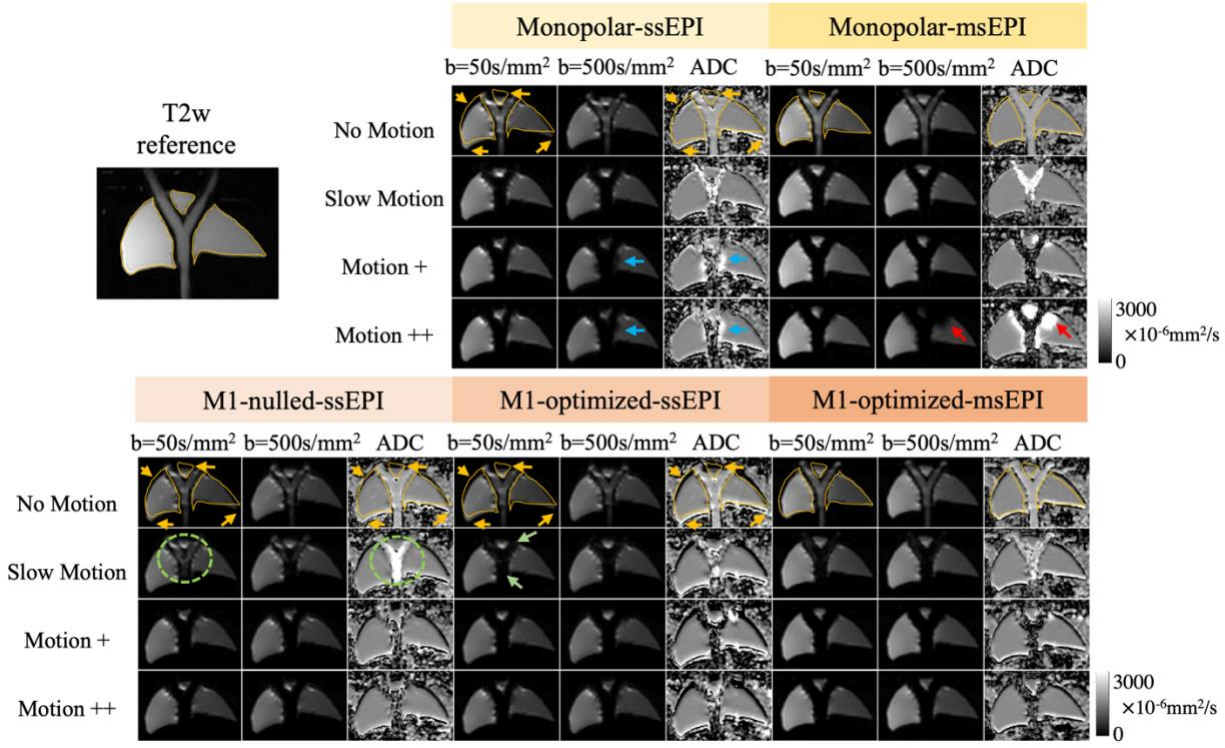

Figure 25. Diffusion-weighted images and apparent diffusion coefficient (ADC) maps in the quantitative motion phantom demonstrate robustness of optimized motion-robust waveforms to compressive motion, suppression of perfusion (blood-mimicking) signals by M1-optimization, and synergy between M1-optimized gradient waveform designs and multishot echo-planar imaging (msEPI) with increasing degrees of compressive tissue motion. *Severe motion-induced signal dropouts (blue arrows) and ADC bias appear in monopolar images and ADC maps. Both M1-nulled and M1-optimized methods avoid the signal dropouts and produce consistent ADC measurements throughout the liver model. With slow flow motion*

(roughly mimicking perfusion), residual bright signal from moving fluid remains in low-b-value images acquired with M1-nulled waveforms, resulting in biased ADC values in the tubing area (green circles). The perfusion signal is suppressed in low-b-value images acquired with M1-optimized waveforms (green arrows). ssEPI images suffer from severe image distortions (yellow contours and yellow arrows). msEPI reduces this image distortion. However, msEPI without motion-robust gradients shows wormhole artifacts in high-b-value images and biased ADC values (red arrows). M1-optimized-msEPI generates stable ADC measurements while maintaining low image distortion (red contours). "Slow motion" represents a flow rate of 0.15 L/min, or a flow velocity of 3.6 cm/s. "Motion +": flow rate = 0.9 L/min, flow velocity = 21.6 cm/s. "Motion ++": flow rate = 1.1 L/min, flow velocity = 26.4 cm/s.

a. Motion phantom		Monopolar waveforms		Motion-robust waveforms		
		ssEPI	msEPI	M1-nulled-ssEPI	M1-optimized-ssEPI	M1-optimized-msEPI
ADC ($\times 10^{-6} mm^2/s$) in motion-affected volume	No motion	1631±63	1634±50	1659±86	1664±125	1640±86
	Slow motion	1625±67	1631±91	1656±99	1661±124	1635±109
	Motion +	2077±667	1686±180	1668±117	1665±166	1636±134
	Motion ++	2070±727	2040±818	1658±114	1678±173	1638±154
	Motion +++	2129±772	2169±813	1714±212	1702±228	1747±346
CCC	CCC measurement	0.50±0.15	0.76±0.14	0.51±0.16	0.50±0.16	0.75±0.15
	p-value	< 0.001		< 0.001 (compared to msEPI)		

Table 6. The mean and SD of ADC measurements from the volume in the phantom within 2 cm of the bifurcation substantially increase with increasing motion for monopolar waveforms. For the motion-robust methods, ADC mean and SD remain stable with increasing motion, although residual artifacts caused by severe motion (+++) appear in M1-optimized-msEPI. *The alignment between DW images from Monopolar-msEPI and M1-optmized-msEPI and the T2w reference is significantly higher than monopolar-ssEPI ($p < 0.001$), M1-nulled-ssEPI ($p < 0.001$), and M1-optmized-ssEPI ($p < 0.001$). "Slow motion" represents a flow rate of 0.15 L/min, or a flow velocity of 3.6 cm/s. "Motion +": flow rate = 0.9 L/min, flow velocity = 21.6 cm/s. "Motion ++": flow rate = 1.1 L/min, flow velocity = 26.4 cm/s. "Motion +++": flow rate = 1.3 L/min, flow velocity = 31.2 cm/s.*

In healthy volunteers, worm-hole artifacts were observed in the msEPI reconstruction with monopolar waveforms, which were mitigated when combining msEPI with motion-robust waveforms. Individual shot images acquired with msEPI and monopolar or M1-optimized waveforms are shown in **Figure 26**. In an inferior slice of the liver, where the right liver lobe was unaffected by cardiovascular pulsation (a), the phase maps were smooth across individual shots acquired with either monopolar or motion-robust waveforms. In contrast, in a superior slice where the cardiovascular-related motion periodically compresses the liver parenchyma (b),

monopolar acquisitions lead to motion-induced rapid spatial phase variations in individual shots, inducing worm-hole artifacts in the msEPI reconstructed image (red arrow). Motion-robust waveforms enable improved phase consistency to mitigate these artifacts in msEPI.

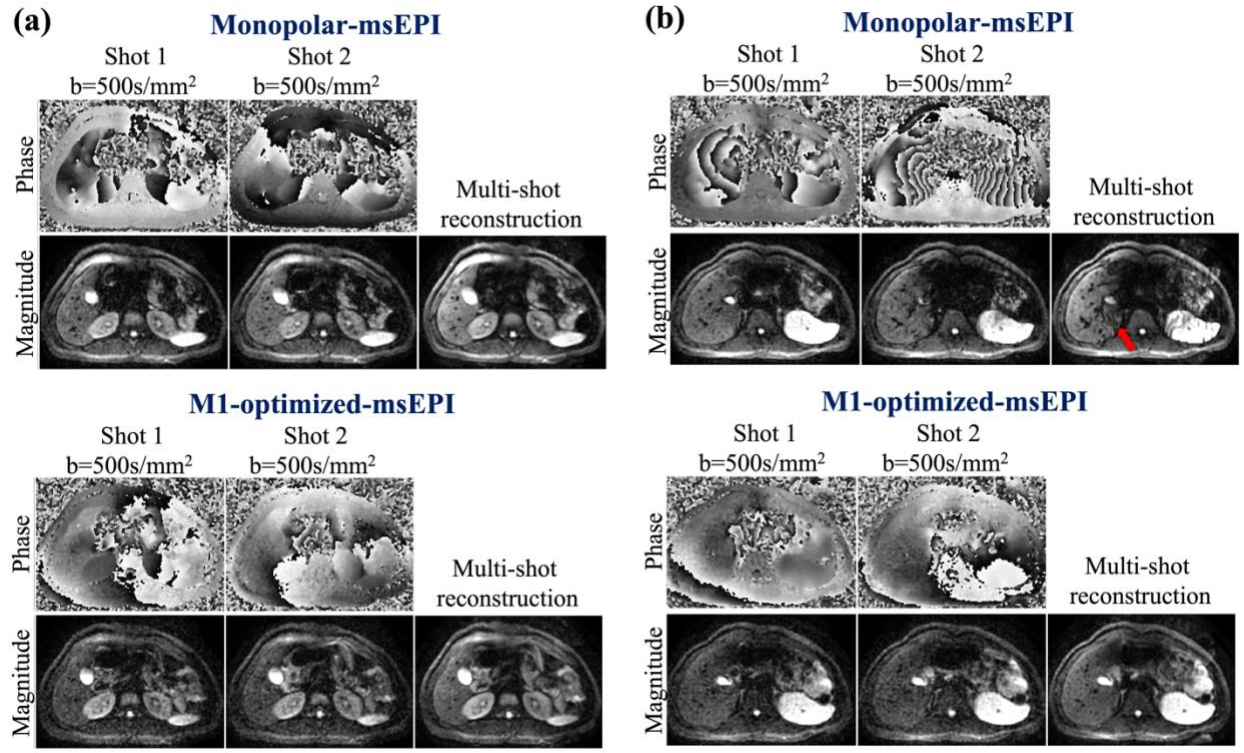

Figure 26. Phase and amplitude maps of individual shot images acquired with multishot echo-planar imaging of a healthy volunteer. *In an inferior slice where the right liver lobe was unaffected by cardiovascular pulsation (a), the phase maps were smooth across individual shots acquired with either monopolar or motion-robust waveforms. In a superior slice where the heart periodically compresses the liver (b), the phase maps acquired with monopolar acquisitions showed rapid variation in the liver, resulting in wormhole artifacts in the multishot reconstructed image (red arrow). However, individual shots acquired with motion-robust waveforms showed smooth phase even in the presence of compressive tissue motion, leading to artifact-free multishot combination.*

In the DW images of patients, reduction of wormhole artifacts due to unpredictable phase variations in the signal acquired from each excitation was observed when combining M1-optimized waveforms with msEPI. **Figure 27** shows a 66-year-old female patient with neuroendocrine carcinoma metastatic to liver (orange arrows). Worm-hole artifacts appear in

msEPI acquired with monopolar waveforms (red circle), while msEPI acquired with M1-optimized waveforms remain free of such artifacts, demonstrating the synergy between M1-optimized motion-robust waveforms and msEPI.

Further studies in larger patient populations are needed to validate the synergistic effects of combined M1-optimized diffusion waveforms and msEPI acquisitions enable reproducible liver DWI with motion robustness, blood signal suppression, and reduced distortion.

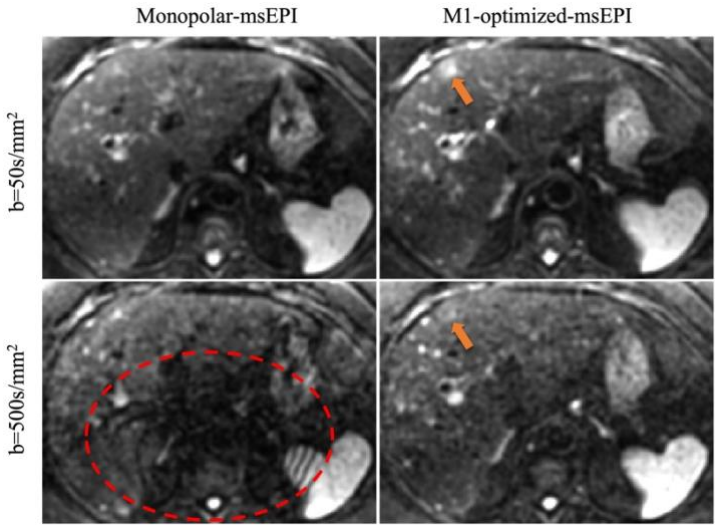

Figure 27. Synergy between M1-optimized motion-robust waveforms and multishot echo-planar imaging (msEPI) in a patient. *A 66-year-old female patient with small bowel neuroendocrine tumor (NET) metastatic to the liver, BMI = 35.72 kg/mm^2. Worm-hole artifacts appear in msEPI acquired with monopolar waveforms (red circle), while msEPI acquired with M1-optimized waveforms remain free of such artifacts. Orange arrows point to a metastasis in the liver.*

Since a synergistic combination is feasible between motion-robust DW gradient waveforms and low-distortion DW-MRI, combining the technique with motion-corrected averaging throughout the respiratory cycle to enable low-distortion, motion-robust, free-breathing DW-MRI acquisitions is a promising direction for future work. Inter-shot respiratory motion would lead to severe ghosting artifacts if left uncorrected. A potential approach is to

retrospectively bin(150) multi-shot acquisitions based on their proximity within the respiratory cycle using acquired bellows signals, reconstruct ms-EPI images separately from each bin within the respiratory cycle and then perform NLM-based motion-corrected averaging or DL-based image post-processing across respiratory phases (as described in Chapter 4).

Another promising line of research is taking advantage of the flexibility of diffusion gradient waveform designs to develop repeatable and reproducible IVIM estimates by optimally sampling the b-M1-space. IVIM quantifies parameters related to the microstructure of liver tissue, including measures of diffusivity (diffusion coefficient (*D*)) and microcirculation of blood (perfusion fraction (*F)* and blood velocity standard deviation (V_b, related to the pseudo-diffusion parameter *D**)). As mentioned in Chapter 1, conventional IVIM-DWI methods suffer from poor test-retest repeatability and reproducibility across field strengths. Ongoing work by our group explores mixed waveform protocols that explicitly sample the first motion moment (M_1) dimension in addition to the b-value dimension for the quantification of IVIM parameters with freely and optimally sampled b-M_1-space (136). By determining an optimal sampling of an echo time (TE) constrained b-M_1-space using CRLB optimization and designing b-M_1-optimized gradient waveforms based on the determined optimal sampling, the method demonstrated improved stability and repeatability of certain IVIM estimates in the liver in comparison to estimates obtained using monopolar samplings in healthy volunteers. Further work incorporates an additional perfusion component in the signal model and takes the advantages of 2D (*b*-M_1) IVIM-DWI acquisitions and ROI-based fitting techniques to achieve repeatable and reproducible tri-exponential IVIM quantification in the livers of healthy volunteers (137). Importantly, the combination of 2D (*b*-M_1) IVIM-DWI acquisitions, physical IVIM signal modeling, and ROI-based fitting techniques has been shown to improve the reproducibility of IVIM quantitative

parameters across field strengths, gradient performances, and liver lobes(153). Further validation of these methods in patients and evaluation of the predictive performance of IVIM quantitative parameters may help develop IVIM quantification as emerging imaging biomarkers in the liver.

Another approach to improving the image quality and reliability of DW-MRI in the abdomen is to improve fat suppression. As mentioned in Chapter 1, B0 inhomogeneities can lead to failures in chemical shift-based fat suppression. Conventional volumetric shimming often fails to compensate for these B0 inhomogeneities, leading to bright fat signals overlapping the organs of interest. Our group has proposed a slice-by-slice shimming method based on knowledge of the water/fat distributions and B0 field map derived from a rapid chemical shift-encoded acquisition(154). This method has demonstrated improved fat suppression in diffusion weighted imaging (DWI) of the abdomen in a healthy volunteer. Further optimization and validation of the method in larger healthy volunteer and patient studies remains future work.

In summary, ongoing and future works in combining motion-robust gradient waveforms, distortion-correction and/or motion-corrected averaging techniques, developing advanced IVIM signal modeling, repeatability and reproducibility studies of diffusion quantitative parameters, and improving fat suppression may improve the image quality and reliability of diffusion quantification in the abdomen.

Bibliography

1. Hernando D, Zhang Y, Pirasteh A: Quantitative diffusion MRI of the abdomen and pelvis. *Med Phys* 2021.

2. Zhou IY, Gao DS, Chow AM, et al.: Effect of diffusion time on liver DWI: an experimental study of normal and fibrotic livers. *Magn Reson Med* 2014; 72:1389–1396.

3. Taouli B, Chouli M, Martin AJ, Qayyum A, Coakley FV, Vilgrain V: Chronic hepatitis: role of diffusion-weighted imaging and diffusion tensor imaging for the diagnosis of liver fibrosis and inflammation. *J Magn Reson Imaging* 2008; 28:89–95.

4. Taouli B, Koh D-M: Diffusion-weighted MR imaging of the liver. *Radiology* 2010; 254:47–66.

5. Chung W-S, Kim M-J, Chung YE, et al.: Comparison of gadoxetic acid-enhanced dynamic imaging and diffusion-weighted imaging for the preoperative evaluation of colorectal liver metastases. *J Magn Reson Imaging* 2011; 34:345–353.

6. Bonekamp S, Torbenson MS, Kamel IR: Diffusion-weighted Magnetic Resonance Imaging for the Staging of Liver Fibrosis. *J Clin Gastroenterol* 2011; 45:885–892.

7. Wang Y, Miller FH, Chen ZE, et al.: Diffusion-weighted MR imaging of solid and cystic lesions of the pancreas. *Radiographics* 2011; 31:E47-64.

8. Balci NC, Perman WH, Saglam S, Akisik F, Fattahi R, Bilgin M: Diffusion-weighted magnetic resonance imaging of the pancreas. *Top Magn Reson Imaging* 2009; 20:43–47.

9. Kartalis N, Lindholm TL, Aspelin P, Permert J, Albiin N: Diffusion-weighted magnetic resonance imaging of pancreas tumours. *Eur Radiol* 2009; 19:1981–1990.

10. Bruegel M, Holzapfel K, Gaa J, et al.: Characterization of focal liver lesions by ADC measurements using a respiratory triggered diffusion-weighted single-shot echo-planar MR imaging technique. *Eur Radiol* 2008; 18:477–485.

11. Padhani AR, Koh D-M: Diffusion MR imaging for monitoring of treatment response. *Magn Reson Imaging Clin N Am* 2011; 19:181–209.

12. Niwa T, Ueno M, Ohkawa S, et al.: Advanced pancreatic cancer: the use of the apparent diffusion coefficient to predict response to chemotherapy. *Br J Radiol* 2009; 82:28–34.

13. Nishiofuku H, Tanaka T, Marugami N, et al.: Increased tumour ADC value during chemotherapy predicts improved survival in unresectable pancreatic cancer. *Eur Radiol* 2016; 26:1835–1842.

14. Trajkovic-Arsic M, Heid I, Steiger K, et al.: Apparent Diffusion Coefficient (ADC) predicts therapy response in pancreatic ductal adenocarcinoma. *Scientific Reports* 2017; 7:17038.

15. Sandrasegaran K, Nutakki K, Tahir B, Dhanabal A, Tann M, Cote GA: Use of diffusion-weighted MRI to differentiate chronic pancreatitis from pancreatic cancer. *AJR Am J Roentgenol* 2013; 201:1002–1008.

16. Bozgeyik Z, Onur MR, Poyraz AK: The role of diffusion weighted magnetic resonance imaging in oncologic settings. *Quant Imaging Med Surg* 2013; 3:269–278.

17. Murphy P, Wolfson T, Gamst A, Sirlin C, Bydder M: Error model for reduction of cardiac and respiratory motion effects in quantitative liver DW-MRI. *Magnetic Resonance in Medicine* 2013; 70:1460–1469.

18. Benner T, van der Kouwe AJW, Sorensen AG: Diffusion imaging with prospective motion correction and reacquisition. *Magn Reson Med* 2011; 66:154–167.

19. Gumus K, Keating B, Poser BA, et al.: Prevention of motion-induced signal loss in diffusion-weighted echo-planar imaging by dynamic restoration of gradient moments. *Magn Reson Med* 2014; 71:2006–2013.

20. Lewis S, Dyvorne H, Cui Y, Taouli B: Diffusion-weighted imaging of the liver: techniques and applications. *Magn Reson Imaging Clin N Am* 2014; 22:373–395.

21. Liau J, Lee J, Schroeder ME, Sirlin CB, Bydder M: Cardiac motion in diffusion-weighted MRI of the liver: artifact and a method of correction. *Journal of Magnetic Resonance Imaging* 2012; 35:318–327.

22. Nasu K, Kuroki Y, Sekiguchi R, Nawano S: The effect of simultaneous use of respiratory triggering in diffusion-weighted imaging of the liver. *Magn Reson Med Sci* 2006; 5:129–136.

23. De Goyeneche A, Peterson E, He JJ, Addy NO, Santos J: One-Click Spine MRI. *3rd Medical Imaging Meets NeurIPS Workshop at the Conference on Neural Information Processing Systems (NeurIPS 2019), Vancouver, Canada* .

24. Tokoro H, Fujinaga Y, Ohya A, et al.: Usefulness of free-breathing readout-segmented echo-planar imaging (RESOLVE) for detection of malignant liver tumors: comparison with single-shot echo-planar imaging (SS-EPI). *Eur J Radiol* 2014; 83:1728–1733.

25. Choi JS, Kim M-J, Chung YE, et al.: Comparison of breathhold, navigator-triggered, and free-breathing diffusion-weighted MRI for focal hepatic lesions. *Journal of Magnetic Resonance Imaging* 2013; 38:109–118.

26. Aliotta E, Wu HH, Ennis DB: Convex optimized diffusion encoding (CODE) gradient waveforms for minimum echo time and bulk motion-compensated diffusion-weighted MRI. *Magn Reson Med* 2017; 77:717–729.

27. Peña-Nogales Ó, Zhang Y, Wang X, et al.: Optimized Diffusion-Weighting Gradient Waveform Design (ODGD) formulation for motion compensation and concomitant gradient nulling. *Magn Reson Med* 2019; 81:989–1003.

28. Zhang Y, Peña-Nogales Ó, Holmes JH, Hernando D: Motion-robust and blood-suppressed M1-optimized diffusion MR imaging of the liver. *Magn Reson Med* 2019; 82:302–311.

29. Luo H, Zhu A, Wiens CN, et al.: Free-breathing liver fat and R 2 ∗ quantification using motion-corrected averaging based on a nonlocal means algorithm. *Magn Reson Med* 2021; 85:653–666.

30. Brenner R, Metens T, Bali M, Demetter P, Matos C: Pancreatic neuroendocrine tumor: Added value of fusion of T2-weighted imaging and high b-value diffusion-weighted imaging for tumor detection. *European Journal of Radiology* 2012; 81:e746–e749.

31. Lee SS, Byun JH, Park BJ, et al.: Quantitative analysis of diffusion-weighted magnetic resonance imaging of the pancreas: usefulness in characterizing solid pancreatic masses. *J Magn Reson Imaging* 2008; 28:928–936.

32. d'Assignies G, Fina P, Bruno O, et al.: High sensitivity of diffusion-weighted MR imaging for the detection of liver metastases from neuroendocrine tumors: comparison with T2-weighted and dynamic gadolinium-enhanced MR imaging. *Radiology* 2013; 268:390–399.

33. Warda MHA, Hasan DI, Elteeh OA: Differentiation of Pancreatic lesions using Diffusion-Weighted MRI. *The Egyptian Journal of Radiology and Nuclear Medicine* 2015; 46:563–568.

34. Jang KM, Kim SH, Lee SJ, Choi D: The value of gadoxetic acid-enhanced and diffusion-weighted MRI for prediction of grading of pancreatic neuroendocrine tumors. *Acta Radiol* 2014; 55:140–148.

35. Hwang EJ, Lee JM, Yoon JH, et al.: Intravoxel incoherent motion diffusion-weighted imaging of pancreatic neuroendocrine tumors: prediction of the histologic grade using pure diffusion coefficient and tumor size. *Invest Radiol* 2014; 49:396–402.

36. Langen KM, Jones DTL: Organ motion and its management. *International Journal of Radiation Oncology*Biology*Physics* 2001; 50:265–278.

37. Barral M, Taouli B, Guiu B, et al.: Diffusion-weighted MR Imaging of the Pancreas: Current Status and Recommendations. *Radiology* 2014; 274:45–63.

38. Ichikawa T, Erturk SM, Motosugi U, et al.: High-b Value Diffusion-Weighted MRI for Detecting Pancreatic Adenocarcinoma: Preliminary Results. *American Journal of Roentgenology* 2007; 188:409–414.

39. Löwenthal D, Zeile M, Lim WY, et al.: Detection and characterisation of focal liver lesions in colorectal carcinoma patients: comparison of diffusion-weighted and Gd-EOB-DTPA enhanced MR imaging. *Eur Radiol* 2011; 21:832–840.

40. Muraoka N, Uematsu H, Kimura H, et al.: Apparent diffusion coefficient in pancreatic cancer: characterization and histopathological correlations. *J Magn Reson Imaging* 2008; 27:1302–1308.

41. Bharwani N, Koh DM: Diffusion-weighted imaging of the liver: an update. *Cancer Imaging* 2013; 13:171–185.

42. Kwee TC, Takahara T: Diffusion-weighted MRI for detecting liver metastases: importance of the b-value. *Eur Radiol* 2011; 21:150.

43. Geng R, Zhang Y, Luo H, Hernando D: Toward high-SNR, motion-robust diffusion MRI of the liver using optimized gradient waveforms, non-gated free-breathing acquisitions, and motion-corrected averaging. *International Society for Magnetic Resonance in Medicine Annual Meeting; 2019; Montreal, Canada* .

44. Furuta A, Isoda H, Yamashita R, et al.: Comparison of monopolar and bipolar diffusion weighted imaging sequences for detection of small hepatic metastases. *Eur J Radiol* 2014; 83:1626–1630.

45. Schakel T, Hoogduin JM, Terhaard CHJ, Philippens MEP: Technical Note: Diffusion-weighted MRI with minimal distortion in head-and-neck radiotherapy using a turbo spin echo acquisition method. *Med Phys* 2017; 44:4188–4193.

46. Morani AC, Elsayes KM, Liu PS, et al.: Abdominal applications of diffusion-weighted magnetic resonance imaging: Where do we stand. *World J Radiol* 2013; 5:68–80.

47. Malayeri AA, El Khouli RH, Zaheer A, et al.: Principles and applications of diffusion-weighted imaging in cancer detection, staging, and treatment follow-up. *Radiographics* 2011; 31:1773–1791.

48. Thoeny HC, De Keyzer F, Chen F, et al.: Diffusion-weighted magnetic resonance imaging allows noninvasive in vivo monitoring of the effects of combretastatin a-4 phosphate after repeated administration. *Neoplasia* 2005; 7:779–787.

49. Chen N-K, Guidon A, Chang H-C, Song AW: A robust multi-shot scan strategy for high-resolution diffusion weighted MRI enabled by multiplexed sensitivity-encoding (MUSE). *Neuroimage* 2013; 72:41–47.

50. Skare S, Newbould RD, Clayton DB, Albers GW, Nagle S, Bammer R: Clinical multishot DW-EPI through parallel imaging with considerations of susceptibility, motion, and noise. *Magn Reson Med* 2007; 57:881–890.

51. Holdsworth SJ, Skare S, Newbould RD, Guzmann R, Blevins NH, Bammer R: Readout-segmented EPI for rapid high resolution diffusion imaging at 3 T. *Eur J Radiol* 2008; 65:36–46.

52. Del Grande F, Santini F, Herzka DA, et al.: Fat-suppression techniques for 3-T MR imaging of the musculoskeletal system. *Radiographics* 2014; 34:217–233.

53. Geng R, Zhang Y, Rice J, et al.: Motion-robust, blood-suppressed, reduced-distortion diffusion MRI of the liver. *Magnetic Resonance in Medicine* 2023; 89:908–921.

54. Ahlgren A, Knutsson L, Wirestam R: Quantification of microcirculatory parameters by joint analysis of flow-compensated and non-flow-compensated intravoxel incoherent motion (IVIM) data. *Nmr Biomed* 2016; 29:640–649.

55. Wetscherek A, Stieltjes B, Laun FB: Flow-compensated intravoxel incoherent motion diffusion imaging. *Magn Reson Med* 2015; 74:410–419.

56. Li YT, Cercueil J-P, Yuan J, Chen W, Loffroy R, Wáng YXJ: Liver intravoxel incoherent motion (IVIM) magnetic resonance imaging: a comprehensive review of published data on normal values and applications for fibrosis and tumor evaluation. *Quant Imaging Med Surg* 2017; 7:59–78.

57. Ding L, Xiao L, Lin X, Xiong C, Lin L, Chen S: Intravoxel Incoherent Motion (IVIM) Diffusion-Weighted Imaging (DWI) in Patients with Liver Dysfunction of Chronic Viral Hepatitis: Segmental Heterogeneity and Relationship with Child-Turcotte-Pugh Class at 3 Tesla. *Gastroenterol Res Pract* 2018; 2018:2983725.

58. Wu H, Liang Y, Jiang X, et al.: Meta-analysis of intravoxel incoherent motion magnetic resonance imaging in differentiating focal lesions of the liver. *Medicine (Baltimore)* 2018; 97:e12071.

59. Cui Y, Dyvorne H, Besa C, Cooper N, Taouli B: IVIM Diffusion-weighted Imaging of the Liver at 3.0T: Comparison with 1.5T. *Eur J Radiol Open* 2015; 2:123–128.

60. Dyvorne HA, Galea N, Nevers T, et al.: Diffusion-weighted imaging of the liver with multiple b values: effect of diffusion gradient polarity and breathing acquisition on image quality and intravoxel incoherent motion parameters--a pilot study. *Radiology* 2013; 266:920–929.

61. Padhani AR, Liu G, Mu-Koh D, et al.: Diffusion-weighted magnetic resonance imaging as a cancer biomarker: consensus and recommendations. *Neoplasia* 2009; 11:102–125.

62. Naganawa S, Kawai H, Fukatsu H, et al.: Diffusion-weighted imaging of the liver: technical challenges and prospects for the future. *Magn Reson Med Sci* 2005; 4:175–186.

63. Hansmann J, Hernando D, Reeder SB: Fat confounds the observed apparent diffusion coefficient in patients with hepatic steatosis. *Magn Reson Med* 2013; 69:545–552.

64. Kazama T, Nasu K, Kuroki Y, Nawano S, Ito H: Comparison of diffusion-weighted images using short inversion time inversion recovery or chemical shift selective pulse as fat suppression in patients with breast cancer. *Jpn J Radiol* 2009; 27:163–167.

65. Nogueira L, Brandão S, Nunes RG, Ferreira HA, Loureiro J, Ramos I: Breast DWI at 3 T: influence of the fat-suppression technique on image quality and diagnostic performance. *Clin Radiol* 2015; 70:286–294.

66. Brandão S, Nogueira L, Matos E, et al.: Fat suppression techniques (STIR vs. SPAIR) on diffusion-weighted imaging of breast lesions at 3.0 T: preliminary experience. *Radiol Med* 2015; 120:705–713.

67. Malyarenko DI, Ross BD, Chenevert TL: Analysis and correction of gradient nonlinearity bias in apparent diffusion coefficient measurements. *Magn Reson Med* 2014; 71:1312–1323.

68. Surov A, Meyer HJ, Wienke A: Correlation between apparent diffusion coefficient (ADC) and cellularity is different in several tumors: a meta-analysis. *Oncotarget* 2017; 8:59492–59499.

69. Geng R, Zhang Y, Muhler MR, Starekova J, Hernando D: Liver Diffusion MRI using Optimized Gradient Waveforms, Free-Breathing Acquisitions, and Motion-Corrected Averaging: Validation in Patients. In *ISMRM 2020*; :#2470.

70. Rutkowski DR, Kim C, Roldán-Alzate A: Hydrogel-based phantoms for magnetic resonance imaging. *Proceedings of Summer Biomechanics, Bioengineering, and Biotransport Conference* ; (SB3C2020) #376.

71. Geng R, Zhang Y, Starekova J, et al.: Characterization and correction of cardiovascular motion artifacts in diffusion-weighted imaging of the pancreas. *Magn Reson Med* 2021; 86:1956–1969.

72. Canellas R, Rosenkrantz AB, Taouli B, et al.: Abbreviated MRI Protocols for the Abdomen. *RadioGraphics* 2019; 39:744–758.

73. Pooler BD, Hernando D, Reeder SB: Clinical Implementation of a Focused MRI Protocol for Hepatic Fat and Iron Quantification. *AJR Am J Roentgenol* 2019; 213:90–95.

74. *Zhao R, Zhang Y, Wang X, et al. Motion-Robust, High-SNR Liver Fat Quantification Using a 2D Sequential Acquisition with a Variable Flip Angle Approach. Magn Reson Med. 2020;84(4):2004-2017. Doi:Https://Doi.Org/10.1002/Mrm.28263*. .

75. Huang SS, Boyacioglu R, Bolding R, MacAskill C, Chen Y, Griswold MA: Free-Breathing Abdominal Magnetic Resonance Fingerprinting Using a Pilot Tone Navigator. *J Magn Reson Imaging* 2021; 54:1138–1151.

76. Wang N, Cao T, Han F, et al.: Free-breathing multitasking multi-echo MRI for whole-liver water-specific T1 , proton density fat fraction, and R 2 ∗ quantification. *Magn Reson Med* 2022; 87:120–137.

77. Roth CJ, Boll DT, Wall LK, Merkle EM: Evaluation of MRI acquisition workflow with lean six sigma method: case study of liver and knee examinations. *AJR Am J Roentgenol* 2010; 195:W150-156.

78. Heye T, Bashir MR. Liver imaging today. Magnetom Flash. 2013;52(2):2013. .

79. Goto T, Kabasawa H: Automated Scan Prescription for MR Imaging of Deformed and Normal Livers. *Magnetic Resonance in Medical Sciences* 2013; 12:11–20.

80. Goto T, Kabasawa H: Automated Positioning of Scan Planes and Navigator Tracker Locations in MRI Liver Scanning. *Medical Imaging Technology* 2010; 28:245–251.

81. Massat MB, Bryant M: Thinking inside the box with AI and ML: A new kind of "insider intelligence." *Applied Radiology* 2019; 48:34–37.

82. Barral JK, Overall WR, Nystrom MM, et al.: A novel platform for comprehensive CMR examination in a clinically feasible scan time. *J Cardiovasc Magn Reson* 2014; 16(Suppl 1):W10.

83. Lemay A: Kidney Recognition in CT Using YOLOv3. *arXiv:191001268 [cs, eess]* 2019.

84. Dey D, Slomka PJ, Leeson P, et al.: Artificial Intelligence in Cardiovascular Imaging. *Curr Treat Options Cardiovasc Med* 2019; 21:25.

85. Itti L, Chang L, Ernst T: Automatic scan prescription for brain MRI. *Magnetic Resonance in Medicine* 2001; 45:486–494.

86. Lecouvet FE, Claus J, Schmitz P, Denolin V, Bos C, Berg BCV: Clinical evaluation of automated scan prescription of knee MR images. *Journal of Magnetic Resonance Imaging* 2009; 29:141–145.

87. Geng R, Buelo CJ, Sundaresan M, et al.: Automated MR Image Prescription of the Liver Using Deep Learning: Development, Evaluation, and Prospective Implementation. *Journal of Magnetic Resonance Imaging* ; n/a(n/a).

88. Redmon J: Darknet: Open Source Neural Networks in C. 2013.

89. *Van Rossum G, Drake Jr FL. Python Reference Manual. Centrum Voor Wiskunde En Informatica Amsterdam; 1995. .*

90. Tzutalin: LabelImg. *Git code* 2015; https://github.com/tzutalin/labelImg.

91. Redmon J, Divvala S, Girshick R, Farhadi A: You Only Look Once: Unified, Real-Time Object Detection. *arXiv:150602640 [cs]* 2016.

92. Pang S, Ding T, Qiao S, et al.: A novel YOLOv3-arch model for identifying cholelithiasis and classifying gallstones on CT images. *PLoS One* 2019; 14:e0217647.

93. Adarsh P, Rathi P, Kumar M: YOLO v3-Tiny: Object Detection and Recognition using one stage improved model. In *2020 6th International Conference on Advanced Computing and Communication Systems (ICACCS)*; 2020:687–694.

94. The Pascal Visual Object Classes (VOC) Challenge | SpringerLink [https://link.springer.com/article/10.1007/s11263-009-0275-4]

95. Martín Abadi, Ashish Agarwal, Paul Barham, et al.: TensorFlow: Large-Scale Machine Learning on Heterogeneous Systems. 2015.

96. Huang SY, Seethamraju RT, Patel P, Hahn PF, Kirsch JE, Guimaraes AR: Body MR Imaging: Artifacts, k-Space, and Solutions. *RadioGraphics* 2015; 35:1439–1460.

97. Zhao Z-Q, Zheng P, Xu S, Wu X: Object Detection with Deep Learning: A Review. *arXiv:180705511 [cs]* 2019.

98. Liu W, Anguelov D, Erhan D, et al.: SSD: Single Shot MultiBox Detector. *arXiv:151202325 [cs]* 2016; 9905:21–37.

99. Ren S, He K, Girshick R, Sun J: Faster R-CNN: Towards Real-Time Object Detection with Region Proposal Networks. *arXiv:150601497 [cs]* 2016.

100. Afshari S, BenTaieb A, Hamarneh G: Automatic localization of normal active organs in 3D PET scans. *Comput Med Imaging Graph* 2018; 70:111–118.

101. Ramachandran S. S, George J, Skaria S, V. V. V: Using YOLO based deep learning network for real time detection and localization of lung nodules from low dose CT scans. 2018; 10575:105751I.

102. Laura CO, Hofmann P, Drechsler K, Wesarg S: Automatic Detection of the Nasal Cavities and Paranasal Sinuses Using Deep Neural Networks. In *2019 IEEE 16th International Symposium on Biomedical Imaging (ISBI 2019)*; 2019:1154–1157.

103. Koch V, Merklein D, Zangos S, et al.: Free-breathing accelerated whole-body MRI using an automated workflow: Comparison with conventional breath-hold sequences. *NMR Biomed* 2022:e4828.

104. O'Brien JJ, Stormann J, Roche K, et al.: Optimizing MRI Logistics: Focused Process Improvements Can Increase Throughput in an Academic Radiology Department. *American Journal of Roentgenology* 2017; 208:W38–W44.

105. Recht M, Macari M, Lawson K, et al.: Impacting key performance indicators in an academic MR imaging department through process improvement. *J Am Coll Radiol* 2013; 10:202–206.

106. Tokur S, Lederle K, Terris DD, et al.: Process analysis to reduce MRI access time at a German University Hospital. *International Journal for Quality in Health Care* 2012; 24:95–99.

107. Beker K, Garces-Descovich A, Mangosing J, Cabral-Goncalves I, Hallett D, Mortele KJ: Optimizing MRI Logistics: Prospective Analysis of Performance, Efficiency, and Patient Throughput. *American Journal of Roentgenology* 2017; 209:836–844.

108. Ichikawa T, Erturk SM, Motosugi U: High-b Value Diffusion-Weighted MRI for Detecting Pancreatic Adenocarcinoma: Preliminary Results. *Am J Roentgenol* 2007; 188:409–414.

109. Brenner R, Metens T, Bali M, Demetter P, Matos C: Pancreatic neuroendocrine tumor: Added value of fusion of T2-weighted imaging and high b-value diffusion-weighted imaging for tumor detection. *Eur J Radiol* 2012; 81.

110. Schmid-Tannwald C, Schmid-Tannwald CM, Morelli JN: Comparison of abdominal MRI with diffusion-weighted imaging to 68Ga-DOTATATE PET/CT in detection of neuroendocrine tumors of the pancreas. *Eur J Nucl Med Mol Imaging* 2013; 40:897–907.

111. Kamisawa T, Takuma K, Anjiki H: Differentiation of autoimmune pancreatitis from pancreatic cancer by diffusion-weighted MRI. *Am J Gastroenterol* 2010; 105:1870–1875.

112. Fattahi R, Balci NC, Perman WH: Pancreatic diffusion-weighted imaging (DWI): comparison between mass-forming focal pancreatitis (FP), pancreatic cancer (PC), and normal pancreas. *J Magn Reson Imaging JMRI* 2009; 29:350–356.

113. Jang KM, Kim SH, Song KD, Kim YK, Lee SJ, Choi D: Differentiation of solid-type serous cystic neoplasm from neuroendocrine tumour in the pancreas: value of abdominal MRI with diffusion-weighted imaging in comparison with MDCT. *Clin Radiol* 2015; 70:153–160.

114. Sandrasegaran K, Nutakki K, Tahir B, Dhanabal A, Tann M, Cote GA: Use of diffusion-weighted MRI to differentiate chronic pancreatitis from pancreatic cancer. *AJR Am J Roentgenol* 2013; 201:1002–1008.

115. Bozgeyik Z, Onur MR, Poyraz AK: The role of diffusion weighted magnetic resonance imaging in oncologic settings. *Quant Imaging Med Surg* 2013; 3:269–278.

116. Ding X, Xu H, Zhou J: Reproducibility of normalized apparent diffusion coefficient measurements on 3.0-T diffusion-weighted imaging of normal pancreas in a healthy population. *Medicine (Baltimore* 2019; 98.

117. Barral M, Soyer P, Ben Hassen W: Diffusion-weighted MR imaging of the normal pancreas: reproducibility and variations of apparent diffusion coefficient measurement at 1.5- and 3.0-Tesla. *Diagn Interv Imaging* 2013; 94:418–427.

118. Wang Y, Chen ZE, Nikolaidis P: Diffusion-weighted magnetic resonance imaging of pancreatic adenocarcinomas: Association with histopathology and tumor grade. *J Magn Reson Imaging* 2011; 33:136–142.

119. Lemke A, Laun FB, Klauss M: Differentiation of pancreas carcinoma from healthy pancreatic tissue using multiple b-values: comparison of apparent diffusion coefficient and intravoxel incoherent motion derived parameters. *Invest Radiol* 2009; 44:769–775.

120. Yoshikawa T, Kawamitsu H, Mitchell DG: ADC Measurement of Abdominal Organs and Lesions Using Parallel Imaging Technique. *Am J Roentgenol* 2006; 187:1521–1530.

121. Kwee TC, Takahara T, Koh D-M, Nievelstein RAJ, Luijten PR: Comparison and reproducibility of ADC measurements in breathhold, respiratory triggered, and free-breathing diffusion-weighted MR imaging of the liver. *J Magn Reson Imaging* 2008; 28:1141–1148.

122. Kandpal H, Sharma R, Madhusudhan KS, Kapoor KS: Respiratory-Triggered Versus Breath-Hold Diffusion-Weighted MRI of Liver Lesions: Comparison of Image Quality and Apparent Diffusion Coefficient Values. *American Journal of Roentgenology* 2009; 192:915–922.

123. Mochiki E, Suzuki H, Takenoshita S: Mechanism of inhibitory effect of glucagon on gastrointestinal motility and cause of side effects of glucagon. *J Gastroenterol* 1998; 33:835–841.

124. Schoennagel BP, Habermann CR, Roesch M: Diffusion-weighted imaging of the healthy pancreas: Apparent diffusion coefficient values of the normal head, body, and tail calculated from different sets of b-values. *J Magn Reson Imaging* 2011; 34:861–865.

125. Dale BM, Braithwaite AC, Boll DT, Merkle EM: Field Strength and Diffusion Encoding Technique Affect the Apparent Diffusion Coefficient Measurements in Diffusion-Weighted Imaging of the Abdomen. *Invest Radiol* 2010; 45:104–108.

126. A KN, F F, MH A, M AJ: ADC values in diffusion-weighted MRI and their relationship with age, gender and BMI in healthy people's pancreases. *Br J Radiol* 2015; 88.

127. Kwee TC, Takahara T, Ochiai R, Nievelstein RAJ, Luijten PR: Diffusion-weighted whole-body imaging with background body signal suppression (DWIBS): features and potential applications in oncology. *Eur Radiol* 2008; 18:1937–1952.

128. Ozaki M, Inoue Y, Miyati T: Motion artifact reduction of diffusion-weighted MRI of the liver: Use of velocity-compensated diffusion gradients combined with tetrahedral gradients. *J Magn Reson Imaging* 2013; 37:172–178.

129. Ma C, Li Y, Pan C: High resolution diffusion weighted magnetic resonance imaging of the pancreas using reduced field of view single-shot echo-planar imaging at 3 T. *Magn Reson Imaging* 2014; 32:125–131.

130. Kim H, Lee JM, Yoon JH: Reduced Field-of-View Diffusion-Weighted Magnetic Resonance Imaging of the Pancreas: Comparison with Conventional Single-Shot Echo-Planar Imaging. *Korean J Radiol* 2015; 16:1216–1225.

131. Goyal AK, Pokharna DS, Sharma SK: Ultrasonic measurements of portal vasculature in diagnosis of portal hypertension. A controversial subject reviewed. *J Ultrasound Med Off J Am Inst Ultrasound Med* 1990; 9:45–48.

132. Starekova J, Geng R, Pirasteh A, Wang Z, Zhang Y, Hernando D: Improved Repeatability of Abdominal Diffusion MRI using Motion-Compensated Methods. In *106th Sci Assem Annu Meet Radiol Soc N Am*; :2020.

133. D LB, E B, D L, ML A, J V, M L-J: Separation of diffusion and perfusion in intravoxel incoherent motion MR imaging. *Radiology* 1988; 168:497–505.

134. Mulkern RV, Gudbjartsson H, Westin CF: Multi-component apparent diffusion coefficients in human brain. *NMR Biomed* 1999; 12:51–62.

135. Bennett KM, Schmainda KM, Bennett R, Rowe DB, Lu H, Hyde JS: Characterization of continuously distributed cortical water diffusion rates with a stretched-exponential model. *Magn Reson Med* 2003; 50:727–734.

136. Jensen JH, Helpern JA, Ramani A, Lu H, Kaczynski K: Diffusional kurtosis imaging: the quantification of non-gaussian water diffusion by means of magnetic resonance imaging. *Magn Reson Med* 2005; 53:1432–1440.

137. Saritas EU, Cunningham CH, Lee JH, Han ET, Nishimura DG: DWI of the spinal cord with reduced FOV single-shot EPI. *Magn Reson Med* 2008; 60:468–473.

138. Chen N, Guidon A, Chang H-C, Song AW: A robust multi-shot scan strategy for high-resolution diffusion weighted MRI enabled by multiplexed sensitivity-encoding (MUSE). *Neuroimage* 2013; 72:41–47.

139. Moulin K, Aliotta E, Ennis DB: Effect of flow-encoding strength on intravoxel incoherent motion in the liver. *Magn Reson Med* 2019; 81:1521–1533.

140. Buades A, Coll B, Morel J-M: A non-local algorithm for image denoising. In *2005 IEEE Computer Society Conference on Computer Vision and Pattern Recognition (CVPR'05)*. *Volume 2*; 2005:60–65 vol. 2.

141. Alkinani MH, El-Sakka MR: Patch-based models and algorithms for image denoising: a comparative review between patch-based images denoising methods for additive noise reduction. *EURASIP Journal on Image and Video Processing* 2017; 2017:58.

142. Lundervold AS, Lundervold A: An overview of deep learning in medical imaging focusing on MRI. *Zeitschrift für Medizinische Physik* 2019; 29:102–127. [*Special Issue: Deep Learning in Medical Physics*]

143. Tsai Y-L, Wu C-J, Shaw S, Yu P-C, Nien H-H, Lui LT: Quantitative analysis of respiration-induced motion of each liver segment with helical computed tomography and 4-dimensional computed tomography. *Radiat Oncol* 2018; 13:59.

144. Hallman JL, Mori S, Sharp GC, Lu H-M, Hong TS, Chen GTY: A Four-Dimensional Computed Tomography Analysis of Multiorgan Abdominal Motion. *International Journal of Radiation Oncology*Biology*Physics* 2012; 83:435–441.

145. Bussels B, Goethals L, Feron M, et al.: Respiration-induced movement of the upper abdominal organs: a pitfall for the three-dimensional conformal radiation treatment of pancreatic cancer. *Radiotherapy and Oncology* 2003; 68:69–74.

146. Nishioka T, Nishioka S, Kawahara M, et al.: Synchronous monitoring of external/internal respiratory motion: validity of respiration-gated radiotherapy for liver tumors. *Jpn J Radiol* 2009; 27:285–289.

147. Tai A, Liang Z, Erickson B, Li XA: Management of Respiration-Induced Motion With 4-Dimensional Computed Tomography (4DCT) for Pancreas Irradiation. *International Journal of Radiation Oncology*Biology*Physics* 2013; 86:908–913.

148. Zhang Y, Peña-Nogales Ó, Holmes JH, Hernando D: Motion-robust and blood-suppressed M1-optimized diffusion MR imaging of the liver. *Magnetic resonance in medicine* 2019; 82:302–311.

149. Allen TJ, Volety S, van der Heijden RA, Simchick G, Hernando D: Reproducibility of M1-optimized Liver DWI Across Field Strengths and Gradient Performance. In *ISMRM 2023*; :#1216.

150. Piccini D, Feng L, Bonanno G, et al.: Four-dimensional respiratory motion-resolved whole heart coronary MR angiography. *Magn Reson Med* 2017; 77:1473–1484.

151. Simchick G, Geng R, Zhang Y, Hernando D: b value and first-order motion moment optimized data acquisition for repeatable quantitative intravoxel incoherent motion DWI. *Magnetic Resonance in Medicine* 2022; 87:2724–2740.

152. Simchick G, Hernando D: Precision of region of interest-based tri-exponential intravoxel incoherent motion quantification and the role of the Intervoxel spatial distribution of flow velocities. *Magn Reson Med* 2022; 88:2662–2678.

153. Simchick G, Allen TJ, Hernando D: Multi-Scanner Reproducibility of IVIM Quantification in the Liver using Pseudo-Diffusion and Physical IVIM Signal Models. In *ISMRM 2023*; :#5009.

154. Tollefson A, Wu G, Lan P, et al.: Slice-by-slice Dynamic Shimming Based on a Chemical Shift-Encoded Acquisition to Improve Fat Suppression in DWI. In *ISMRM 2023*; :#3409.